POLITECNICO DI TORINO

Master Degree course in Biomedical Engineering

Biomedical Instrumentation

Master Degree Thesis

Analysis of inferior vena cava dynamics under controlled breathing conditions

Supervisor
Prof. Luca Mesin

Candidate
Gabriele De Palma

Academic Years 2023/2024

Ai miei genitori,
A mio fratello,
A mio nipote,
A me stesso

Summary

Ultrasonography of the inferior vena cava (IVC) is a technique widely used in clinical practice to assess its size and pulsatility, providing important information on the volemic status of patients. In addition, it is used to predict fluid responsiveness. Finally, it provides a non-invasive estimate of right atrial pressure (RAP), which is usually measured by an invasive procedure called right heart catheterisation (RHC).

Non-invasive estimation of RAP is obtained as a function of IVC maximum diameter and Caval Index (CI), defined as the ratio of the difference between the maximum and minimum diameter and the maximum diameter of the IVC. This is achieved by using a respiratory manoeuvre called sniff, which involves a quick, strong inhalation through the nose by the patient, but is non-standardised.

The aim of this thesis is to analyse the dynamics of the IVC, in terms of size and pulsatility indices (CI, RCI, CCI), under controlled breathing conditions. To this end, a spirometer was built and 3D printed, starting from a model created in a previous thesis work and attempting to overcome the problems that emerged, through which it is possible to provide visual feedback to the subject. Subsequently, a user interface was developed to facilitate the operator in data acquisition and to display the signal for visual feedback. Finally, an experimental protocol was tested on 10 healthy subjects with the aim of assessing changes in IVC pulsatility in three different breathing modes: light, normal and deep. For the IVC segmentation, necessary to extract information on size and pulsatility indices, the software developed by Viper s.r.l. was used, which is able to follow the vein borders throughout the ultrasound recording.

The mean values and standard deviation of the CI, RCI and CCI are 34.30 ± 9.36 %, 24.46 ± 8.49 % and 16.71 ± 6.62 % for the light breathing condition; 45.79 ± 11.72 %, 35.36 ± 9.62 % and 19.97 ± 9.62 % for the normal breathing condition; and 52.30 ± 9.89 %, 41.00 ± 9.23 % and 20.21 ± 11.45 % for the deep breathing condition, respectively. The increase in IVC pulsatility that occurs with increasing exertion by the subject is mainly due to a greater reduction in IVC minimum diameter. The mean value and standard deviation of the minimum diameter are 10.58 ± 3.48 mm, 8.79 ± 3.71 mm and 7.62 ± 2.57 mm for the light, normal and deep breathing conditions, respectively. Friedman's test and the Wilcoxon signed-rank test were used to highlight any statistically significant differences between the normal breathing condition and the other two conditions: both breathing conditions show significant differences. Only weak correlations were observed between IVC parameters and differential pressure values obtained from the sensors connected

to the spirometer.

The results show that the three conditions tested can induce a different pulsatility of the IVC, even though the effort required of the subject is not excessive. However, this approach has some limitations that could be overcome with future research.

Acknowledgements

Contents

List of Figures

List of Tables

Chapter 1

Introduction

The inferior vena cava (IVC) represents the largest vein in the entire cardiovascular system., characterised by high compliance, whose dynamics are influenced both by the structures to which it is anchored and by the respiratory and cardiac cycle. With regard to respiratory activity, the diameter of the IVC decreases during inspiration and increases during expiration. Regarding cardiac activity, the diameter of the IVC decreases before atrial systole and increases during atrial contraction.

In clinical practice, assessment of IVC pulsatility by ultrasonography can provide information on the patient's volemic status. This technique, due to its non-invasiveness, wide availability and low cost, allows assessment of central venous pressure (CVP) [6]. Moreover, it offers the possibility of predicting the response of haemodynamically unstable patients to fluid administration, thus helping to determine whether such intervention is appropriate. Indeed, only half of such patients respond positively to fluid therapy, while the others risk developing fluid overload [7]. Finally, IVC pulsatility offers a non-invasive method to estimate right atrial pressure (RAP), which is essential for the haemodynamic analysis of patients. High RAP values, usually above 10 mmHg, are typically observed in patients with conditions such as heart failure or pulmonary hypertension.

The gold standard for estimating RAP is 'right heart catheterisation' (RHC), a procedure in which a catheter equipped with sensors is inserted into the heart to directly monitor RAP. However, this technique is invasive and can carry risks such as infection and thrombosis.

Alternatively, ultrasonography of the IVC is a viable option for non-invasive estimation of RAP by assessing the size and pulsatility of the vein. The main indicator of IVC pulsatility is the Caval Index (CI), defined as the relative reduction in IVC diameter during the respiratory cycle.

Current guidelines for the non-invasive estimation of RAP using ultrasonography of the IVC involve the execution of an inspiratory manoeuvre called 'sniffing', which involves a strong inhalation through the nose by the patient. However, this manoeuvre is not standardised and therefore not reliable. Furthermore, although these guidelines demonstrate good accuracy in estimating low or high RAP, they are less accurate for intermediate values [8].

Echocardiographic estimation of RAP is affected by both operator- and patient-dependent variability. Part of it is attributable to the movements of the IVC relative to the ultrasound probe during the respiratory cycle, mainly in the cranio-caudal direction, thus leading to the comparison of different points of the IVC during inspiration and expiration. To address this issue, VIPER (Vein Image Processing for Edge Rendering) has developed a semi-automated software that can compensate for IVC movements and consider an entire portion of the IVC, highlighting its edges. This allows for more precise and reliable estimates than standard measurements.

The aim of this thesis is to analyse the pulsatility changes of the IVC under different controlled breathing conditions. For this purpose, a spirometer was developed, through which visual feedback can be provided to the patient, and an experimental protocol was implemented to analyse the dynamics of the IVC.

The following chapters provide an overview of the cardiovascular system, the respiratory system, ultrasonography and current techniques for estimating RAP. Next, a detailed description of the software and tools used for data acquisition and processing is provided. Finally, the experimental protocol used is outlined, together with the results obtained and related discussions.

Chapter 2

Background

2.1 Cardiovascular system

The cardiovascular system is a complex system consisting of several elements:

- Heart

- Blood vessels

- Blood

The function of the cardiovascular system is to ensure adequate blood circulation in the body in order to properly supply the body's tissues with oxygen and nutrients, necessary for their functioning, and to eliminate carbon dioxide and waste substances.

2.1.1 Heart and cardiac cycle

The heart is an organ composed of muscle tissue and, through alternating phases of contraction and relaxation, it pumps blood in blood vessels.
It is functionally divided in right heart and left heart, separated by a wall called 'septum', which prevents mixing of the blood present in the two parts. Indeed, oxygenated blood is present in the left heart, while deoxygenated blood is present in the right heart.
Each of the two parts is divided in two chamber:

- Atrium: the upper chamber into which the blood arriving from the venous vessels enters

- Ventricle: the lower chamber from which the blood goes out into the arterial vessels

Atria and ventricles on each side are separated by a valve, known as 'atrioventricular valve', which opens and closes depending on the pressure variation between upper and lower chambers, and it allows blood to flow from the atrium to the ventricle preventing the reverse pathway. The valve on the left side is called 'mitral

valve', while the valve on the right side is called 'tricuspid valve'.

Finally, there are the 'semilunar valves', located between the ventricles and arteries, and they too allow blood to flow in only one direction, i.e. form ventricle to artery. The left valve is called 'aortic valve' because it is located between the left ventricle and the aorta, while the right valve is called 'pulmonary valve' because it is located between the right ventricle and the pulmonary arteries.
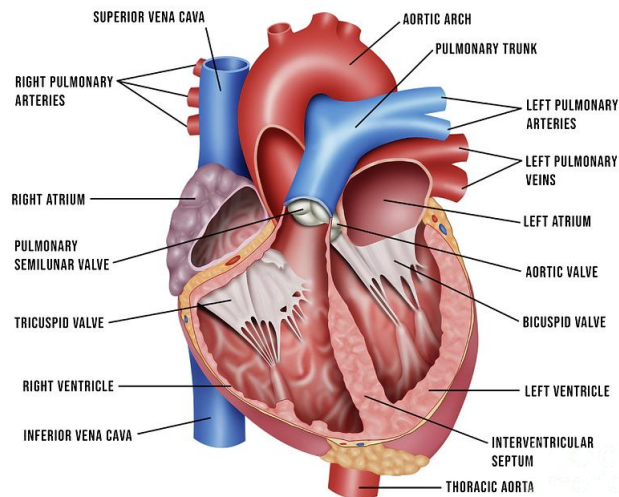
Figure 2.1: *Heart*

The cardiac cycle includes all events that occur during a single heartbeat, i.e. from the beginning of one heartbeat until the beginning of the next one.

It consists of two stages:

- Systole: ventricular contraction phase

- Diastole: ventricular relaxation phase

The cardiac cycle begins with atrial systole, during which the atria contract, the pressure inside them increases and, when the pressure is higher than the pressure in the ventricles, the two atrioventricular valves open allowing blood to flow to the ventricles. This represents the 'ventricular filling' phase.

Subsequently, ventricular systole occurs. In the first phase of ventricular systole, the atria relax, while the ventricles contract and the pressure inside them increases. This causes the atrioventricular valves to close, but the pressure is not high enough to open the semilunar valves. Since blood is not yet releases from the ventricles as the semilunar valves are closed, this phase is called 'isovolumetric contraction'. In the second phase of ventricular systole, 'ventricular ejection' occurs. The pressure within the ventricles exceeds the arterial pressure, causing the opening of the semilunar valves, and the blood flows into the arteries (pulmonary arteries and aorta). At this point, the pressure in the ventricles begins to drop and falls below the pressure in the arteries, so the semilunar valves close, but it is still too high to keep the atrioventricular valves open.

Since the atrioventricular valves remain closed, there is no change in blood volume in the ventricles, so the initial phase of ventricular diastole is called 'isovolumetric relaxation' phase. In the second phase of ventricular diastole, the blood pressure in the ventricles decreases and falls below the blood pressure in the atria, causing the atrioventricular valves to open, and blood flows from the atria to the ventricles. Then the cardiac cycle begins again.
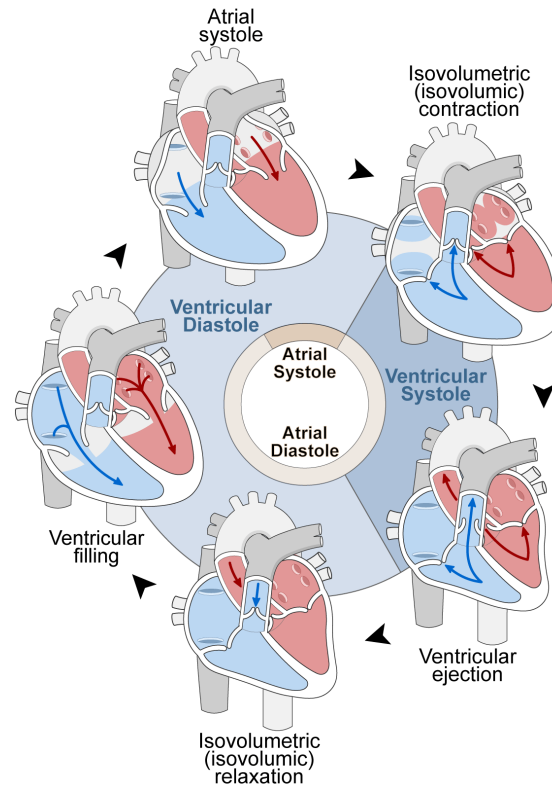
Figure 2.2: *Cardiac Cycle*

2.1.2 Blood vessels

The blood vessels are hollow ducts through which blood is transported from the heart to the organs and vice versa. The set of blood vessels is also known as the 'vascular system'. It is possible to distinguish three types of vessels:

- Arteries: vessels that transport oxygenated blood from heart to tissues. They branch into arterioles

- Veins: vessels that transport deoxygenated blood from tissues to heart. They branch into venules

- Capillaries: smaller vessels where the exchange of nutrients and catabolites between blood and tissue takes place [9]

Blood vessels, specifically arteries and veins, consist mainly of three layers of tissue:

- Intima: the innermost layer in contact with blood, composed of endothelial cells. It is separated from the next layer by the 'internal elastic lamina'

- Media: the intermediate layer composed of smooth muscle tissue and connective tissue (fibrous and/or elastic), which regulate the diameter of the vessel. It is separated from the adventizia by the 'external elastic lamina'

- Adventizia: the outermost layer composed of collagen, elastic fibres, fibroblasts and vasa vasorum. It provides structural support and shape of the vessel
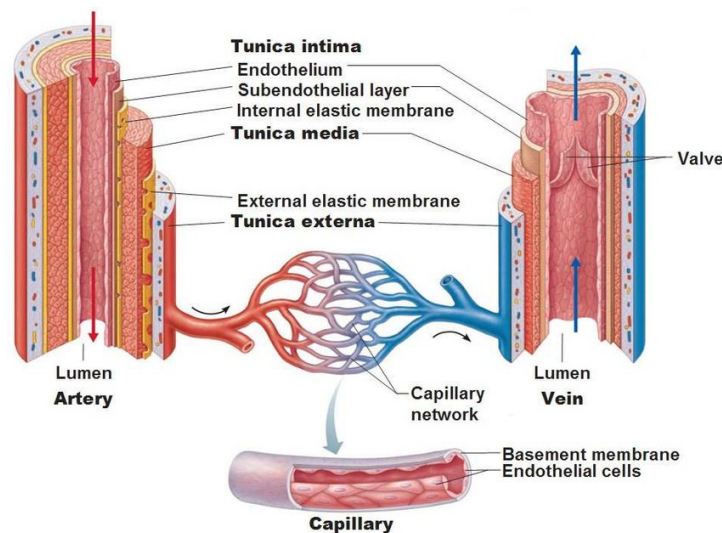
Figure 2.3: *Structure of blood vessels*

Arteries are the blood vessels that conduct the blood from the heart to the rest of the body. In order to withstand the high pressure of blood pumped from the heart, they are characterised by a fairly large internal diameter and thickness. Arteries are classified into elastic arteries such as the aorta and pulmonary arteries, which contain more elastic tissue than muscle tissue, and muscular arteries, in which the amount of smooth tissue is greater than elastic tissue.

Veins, on the other hand, transport blood to the heart and they are characterised by thin walls. Indeed, venous pressure is lower than arterial pressure. Unlike arteries, veins have the characteristic of being equipped with unidirectional valves, which facilitate venous return to the heart, preventing the reflux of blood, and they are characterised by high compliance, so they are able to considerably dilate in the face of small changes in pressure.

2.1.3 Inferior Vena Cava

The vena cava is divided into Inferior Vena Cava (IVC) and Superior Vena Cava (SVC). They are the the largest veins in the entire body, and they are responsible for transporting deoxygenated blood to the right atrium of the heart. Specifically,

the IVC carries blood from the lower part of the body (lower extremities and abdomen) to the heart, while the SVC carries blood from the upper part of the body to the heart.

The inferior vena cava is formed by the confluence of the two common right and left iliac veins in the belly area and flows into the right atrium. It is the largest vessel in the overall venous system, thin-walled, retroperitoneal, and with a diameter of approximately 30 mm. Since the IVC accounts for two-thirds of the systemic venous return, it can be clinically used as marker of volemic status, which is a key component of clinical assessment [10].

Indeed, the evaluation of the diameter of the inferior vena cava and its pulsatility provides information on the volume status, but also on fluid responsiveness, right heart function, heart-lung interaction and right atrial pressure [6].

In general, the assessment of changes in the inferior vena cava is performed using non-invasive methods, such as ultrasonography, however, there is a lack of standardization in measurement techniques and results are affected by patient- and operator-dependent variability.

2.2 Respiratory system

The respiratory system includes all the organs involved in respiration, i.e. the process of gas exchange. Specifically, it supplies oxygen to the cells and eliminates products such as carbon dioxide.
It consists of several components:

- Upper airways (nasal cavity, oral cavity, pharynx)

- Respiratory tract (larynx, trachea)

- Lungs

Air enters the body through the nasal and/or oral cavity, passes into the pharynx and enters the larynx. Subsequently, air passes into the trachea and primary bronchi. Within each lung, the primary bronchi divide into smaller and smaller structures until they reach the bronchioles, at the ends of which are the pulmonary alveoli, which represent the area where gas exchange takes place.

2.2.1 Respiratory mechanics

The breathing process is driven by the pressure gradients between alveoli and outside aria that are created due to volume variations in the lungs, produced by the diaphragm and chest muscles. Specifically, these volume variations are reflected in pressure variations within the lungs, in accordance with the Boyle's law of inverse proportionality between volume and pressure, which allows the airflow involved in breathing to move by pressure gradient, i.e from high-pressure zones to low-pressure zones.

Air movement mainly depends on the difference between intra-alveolar pressure

and atmospheric pressure. The latter remains constant, while the first varies during the phases of breathing.
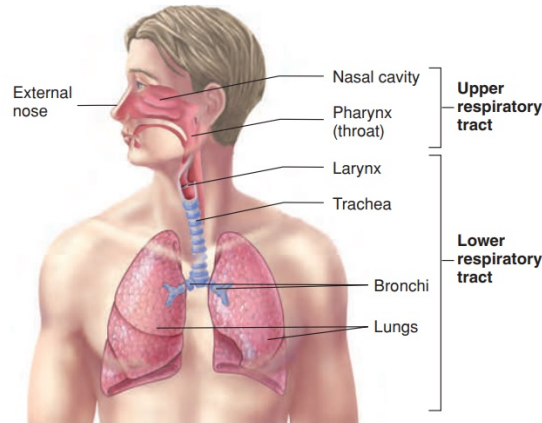
Figure 2.4: *Respiratory system divided into upper respiratory tract and lower respiratory tract*
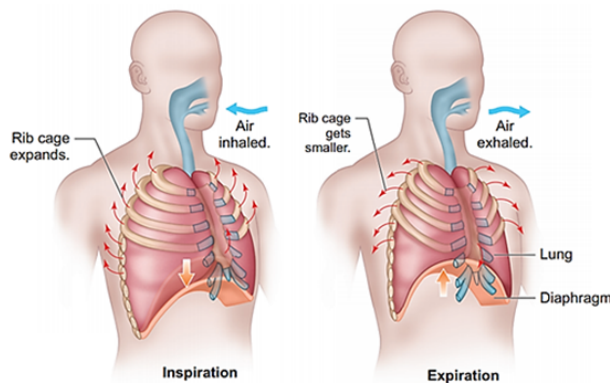
Figure 2.5: *Mechanism of breathing*

Breathing is divided into two phases: inspiration and expiration.
Inspiration is an active process, as it involves the action of the respiratory muscles, during which air enters the lungs. The diaphragm contracts and lowers, the intercostal muscles contract causing the ribs to rotate outwards and upwards. These contractions induce an expansion of the rib cage and lungs, resulting in an increase in volume and a reduction in intra-alveolar pressure, which falls below atmospheric pressure. The pressure gradient thus generated allows air to flow into the lungs.
Expiration, unlike the previous process, is a passive act, as it does not involve the active involvement of muscles. At the end of inspiration, the lungs and rib cage return to their initial condition, causing a decrease in volume and an increase in intra-alveolar pressure, which exceeds atmospheric pressure. This allows air to escape into the external environment.
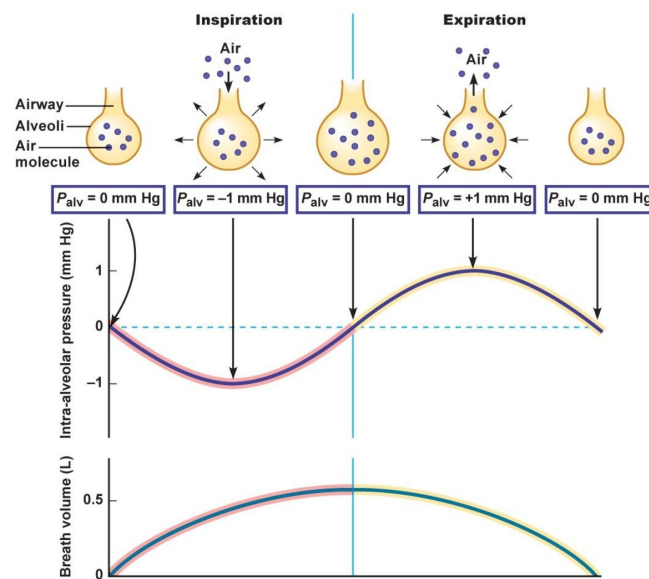
Figure 2.6: *Intra-alveolar pressure and breath volume changes during inspiration and expiration*

2.2.2 Lung volumes and capacities

Lung function is assessed by clinicians through measurements of lung volumes and capacities [9]. The lung volumes are:

- Tidal volume (TV): volume of air inhaled and exhaled during an unforced respiratory act. On average it is 500 mL.

- Inspiratory reserve volume (IRV): volume of air that can still be inhaled at the end of an unforced respiratory act. On average it is 3000 mL.

- Expiratory reserve volume (ERV): volume of air that can still be exhaled at the end of an unforced respiratory act. On average it is 1000 mL.

- • Residual volume (RV): volume of air remaining in the lungs following maximal exhalation. On average it is 1200 mL.

The lung capacities result from the sum of two or more lung volumes, and are:

- Inspiratory capacity (IC): maximum volume of air that can be inhaled at the end of a normal exhalation.

- Vital capacity (VC): maximum volume of air that can be exhaled after a maximum inhalation.

- Functional residual capacity (FRC): volume of air remaining in the lungs at the end of a normal exhalation.

- Total lung capacities (TLC): volume of air present in the lungs at the end of a maximal inhalation.
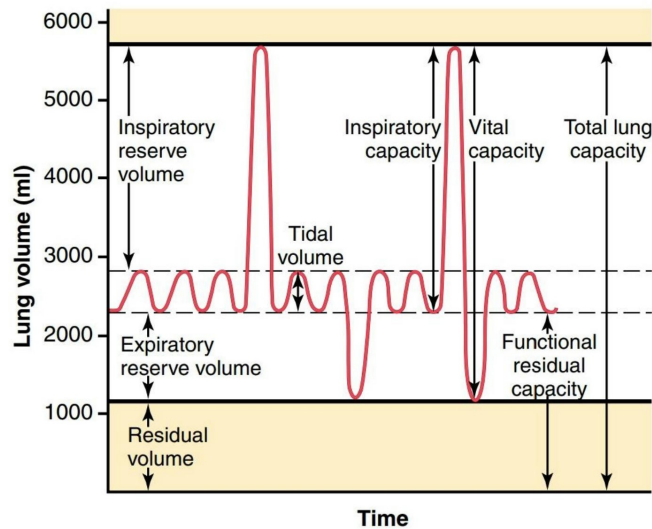
Figure 2.7: *Lung volumes and capacities*

2.2.3   Spirometry

Spirometry is a technique for assessing a patient's lung function by measuring the air that is inhaled and exhaled. However, residual volume cannot be measured using this technique, so neither functional residual capacity nor total lung capacity can be calculated.

The instrument used in a spirometry examination is the spirometer. The first device dates back to 1846, made by physician John Hutchinson, and it consists of an inverted bell filled with air and placed in a container filled with water. The bell is connected to the patient's mouth via a hose and to a pen. During inhalation ed exhalation phases, the bell descends towards the water and rises upwards, respectively. These movements of the bell are transmitted to the pen, which draws lines on a rotating cylinder at constant speed indicating the volume of air entering and leaving the lungs.

Nowadays, there are different versions of the spirometer and they are computerised, i.e. they use transducers that convert the volume of air inhaled/exhaled into electrical signals, which are then interpreted in order to provide a reading of lung volumes and capacities. A spirometry test generally involves a deep inhalation by the patient followed by a strong and rapid exhalation. In addition, a nasal clip is applied to the patient during the test in order to obtain the maximum possible effort. As a rule, the test is performed at least three times to ensure accurate and reproducible results. This test provides a parameter known as Forced Vital Capacity (FVC), which corresponds to the volume of air that is expelled during a forced expiration following a maximal inhalation.

Spirometry is mainly used as a diagnostic test for asthma and chronic obstructive pulmonary disease (COPD), but it also allows the early detection of individuals at risk of lung disease or the assessment of the severity of lung disease [11].
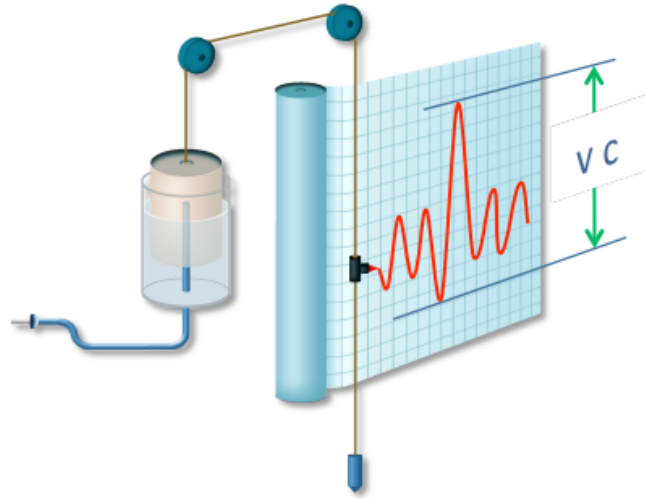
Figure 2.8: *Simple representation of the Hutchinson's spirometer*

2.3 Ultrasonography

Ultrasonography is an imaging technique that uses high-frequency mechanical waves to obtain two-dimensional images, exploiting the physical principle of reflection.

The frequencies of these acoustic waves are higher than the band of human hearing, i.e. above 20 kHz. In practice, the frequencies involved range from 2 to 20 MHz.

The advantage of ultrasonography is that it uses non-ionising radiation, so this technique is suitable for long-term measurements, and it is applicable to patients at risk, such as pregnant women. Furthermore, this imaging modality is characterised by a high temporal resolution, so that many frames can be acquired in the unit of time, which allows images to be observed in real-time.

2.3.1 Ultrasound physics

The propagation speed of ultrasounds varies depending on the medium in which they propagates. In general, the wave propagation speed is described as:

$$v = \lambda \cdot f \tag{2.1}$$

where λ is the wavelength and f is the frequency of the wave.

The only medium in which ultrasound cannot propagate is the vacuum, as it is devoid of molecules. Indeed, mechanical waves need to set molecules in the medium in motion to propagate.

In ultrasonic devices, the speed is set at 1540 m/s.

Within the body, ultrasound interacts with tissues on the basis of the acoustic impedance of those tissues. Acoustic impedance is defined as:

$$Z = \rho \cdot v \tag{2.2}$$

where ρ is the density of the tissue and v is the propagation speed of the wave. This parameter varies between the different tissues of the human body: for instance, soft tissues have similar acoustic impedance, while bones have a very high acoustic impedance.

Material	Density (Kg/m^3)	Propagation Velocity (m/s)	Acoustic Impedance $(Kg/m^2/s \cdot 10^6)$
Air	1200	330	0.0004
Water	1000	1480	1.48
Soft tissue	1060	1540	1.63
Muscle	1080	1580	1.70
Fat	952	1459	1.38
Brain	994	1560	1.55
Kidney	1038	1560	1.62
Liver	1060	1550	1.64
Lung	400	650	0.26
Bone	1912	4080	7.80

Table 2.1: *Density, Propagation velocity and Acoustic Impedance values of air, water and biological tissues*

When a wave travels in a medium with a certain acoustic impedance and encounters a discontinuity, i.e. the medium interfaces with another medium characterised by a different acoustic impedance, part of the acoustic energy is reflected and part is transmitted.

The physical principle behind this phenomenon is the reflection principle, governed by Snell's law, according to which the angle of reflection coincides with the angle of incidence and the ratio of the sine of the angle of incidence to the sine of the angle of transmission is constant and equal to the ratio of the refractive index of the second medium to the refractive index of the first medium:

$$\theta_i = \theta_r \tag{2.3}$$

$$\frac{\sin \theta_i}{\sin \theta_t} = \frac{n_2}{n_1} \tag{2.4}$$

In ultrasonography, we make the assumption of normal incidence, whereby the waves propagate along the same direction. To know how much acoustic energy is reflected and how much is transmitted, it is necessary to introduce two coefficients: reflection coefficient R and transmission coefficient T. Their definitions are:

$$R = \left(\frac{Z_1 - Z_2}{Z_1 + Z_2} \right)^2 \tag{2.5}$$

$$T = 1 - R \tag{2.6}$$
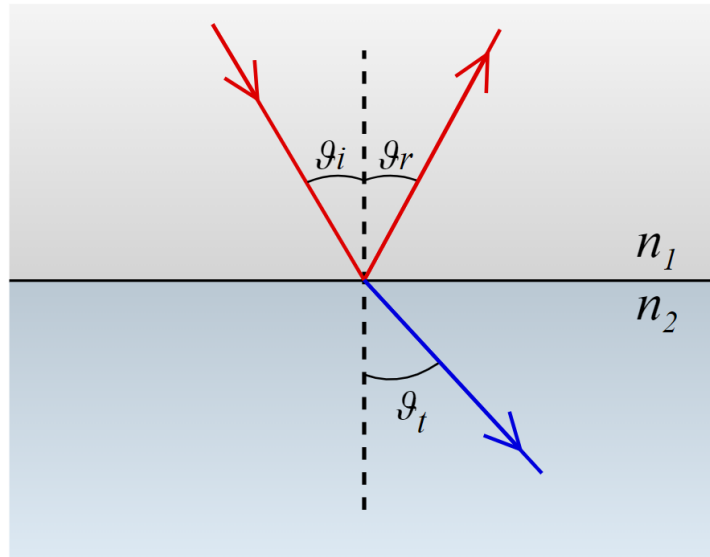
Figure 2.9: *Reflection principle and Snell'law. The incident wave hits the interface with an angle of incidence θ_i. At the interface, part of the wave is reflected with an angle of reflection θ_r equal to θ_i and part is transmitted with an angle of transmission θ_t.*

where Z_1 and Z_2 are the acoustic impedance values of the two media interfacing. The component of interest is the acoustic energy that is reflected when the wave encounters the discontinuity. The reflect wave is also called echo.

If R is small, i.e. the two interfacing media have acoustic impedance values close to each other, the reflected energy is small. In this case, it is difficult to detect reflected echoes. If R is high, i.e. the two acoustic impedance values are very different from each other, the reflected energy is large. In the borderline case where R is unitary, imaging is difficult. For example, when tissues of the human body are to be investigated, microbubbles of air are trapped between the ultrasound probe and the skin, which leads to a reflection coefficient 1. Consequently, it is necessary to interpose a layer of gel between the probe and the skin to avoid this problem.

Finally, it is necessary to take into account another fundamental phenomenon concerning the propagation of ultrasounds within a medium, that is the attenuation. To propagate, ultrasound set the molecules of the medium in motion and this results in the loss of energy by the wave. In other terms, the wave undergoes attenuation according to the following law:

$$A(z) = A_0 \cdot e^{-\alpha z} \tag{2.7}$$

where A_0 is the initial amplitude of the wave, α is the attenuation coefficient of the medium and z is the depth.

It can be seen that as the depth increases, the amplitude of the wave decreases, so as the wave propagates in the medium it is attenuated more and more.

Nevertheless, the attenuation also depend on the frequency of the wave: as the frequency increases, the attenuation coefficient of the medium increases.

At the same time, however, the frequency of the wave affects the spatial resolution of the image. Indeed, the higher the frequency, the shorter the wavelength, which represents the minimum distance between two structures capable of generating distinguishable echoes.

Consequently, a compromise has to be found: high frequencies allow high spatial resolution but only allow the investigation of surface structures, low frequencies allow deep structures to be investigated but losing in spatial resolution.

2.3.2   Ultrasounds generation

Ultrasounds are generated by the phenomenon of piezoelectricity. There are two different effects:

- Direct piezoelectric effect: a geometric variation of the piezoelectric crystal generates a variation of potential between the faces of the crystal

- Indirect piezoelectric effect: a variation of potential imposed between the faces of the crystal generates a geometric variation of the crystal
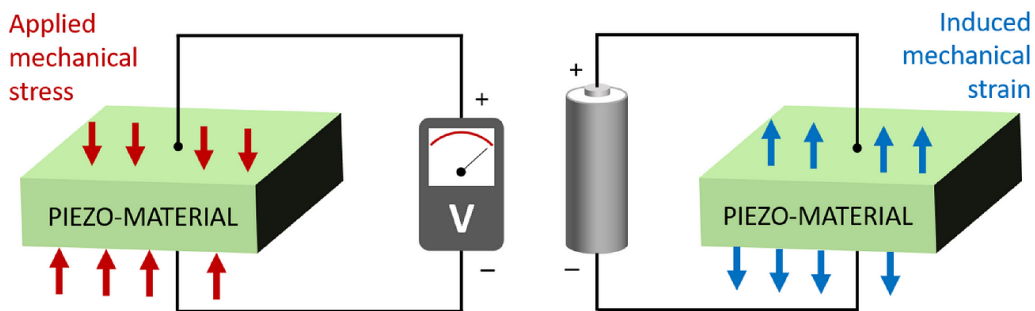
Figure 2.10: *Direct (left) and indirect (right) piezoelectric effect*

The effect used to generate ultrasounds is the reverse one: a potential difference is imposed between the faces of the crystal, it responds with a mechanical change, i.e. it vibrates, and the mechanical waves propagate into the tissues.

Initially, quartz was used as material for piezoelectric crystals, but nowadays special ceramics such as lead-zirconate-titanate (PZT) are used, where the speed propagation of ultrasounds is about 4000 m/s.

The direct effect, on the other hand, is used to measure return echoes.

Piezoelectric crystals, which are located inside the ultrasound probe, act both as an emitter of ultrasounds and as a receiver of return echoes, but they cannot do both at the same time. Therefore, ultrasound emission is not continuous but pulsed, i.e. a packet of ultrasound is emitted whose duration is expressed in terms of time or in terms of the wavelengths contained in the packet. The length of the packet determines the axial resolution, i.e. the resolution along the direction of propagation of the ultrasound wave. In particular, if the distance between two

discontinuities generating return echoes is less than the packet's length, the two discontinuities are recognised as one.

2.3.3   Ultrasound image generation

The ultrasound image is basically a two-dimensional map of the reflection coefficient of the tissues.

The probe consists of many piezoelectric elements, each of which emits a pulse. When the pulse encounters a discontinuity, a return echo is generated by reflection. By measuring the time-of-flight, i.e. the time between emission of the pulse and reception of the return echo, it is possible to calculate the distance from the probe at which the echo was generated:

$$d = \frac{1}{2} \cdot c \cdot \Delta t \tag{2.8}$$

where c is the propagation speed of the pulse (1540 m/s) and Δt is the time-of-flight. Once the depth at which there is the discontinuity is obtained, the amplitude of the return echo, that is proportional to the reflection coefficient, is converted to colour to form the ultrasound image.

As previously mentioned, however, return echoes are attenuated as they propagate in tissues. Thus, the amplitude of the return echo depends on the reflection coefficient R but also on the depth at which it is generated. To eliminate the effect due to the depth, Time-Gain-Compensation (TGC) is used, that is a device that amplifies the return echo by an amount proportional to its time-of-flight. It is a logarithmic amplifier that has the time-of-flight of an echo as its argument. In doing so, only the information related to the reflection coefficient is retained and colour-coded to form the image.
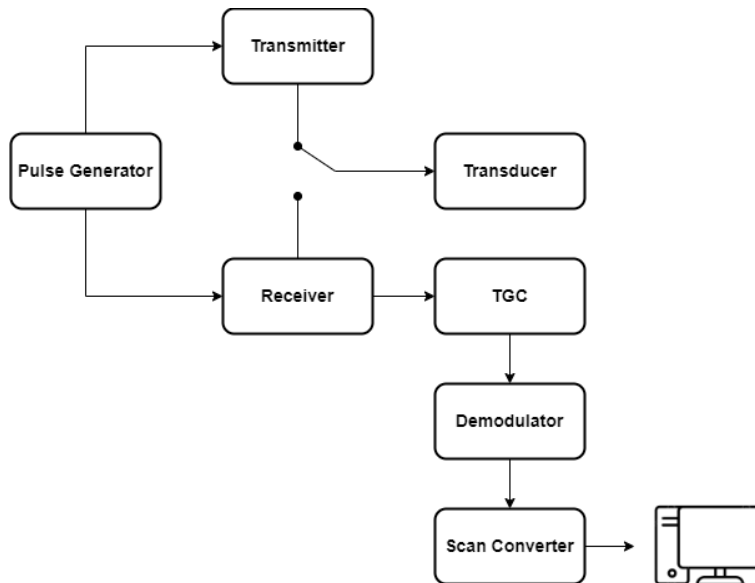
Figure 2.11: *Flow chart of ultrasounds*

To summarise, image formation can be described by the following steps:

1. The piezoelectric crystal emits the ultrasonic pulses

2. The transducer receives the return echoes

3. The time-of-flight of the return echo is calculated and thus the depth at which the discontinuity is present

4. The signal has amplitude proportional to the reflection coefficient R

5. The TGC amplifies the return echo by a quantity proportional to its time-of-flight

6. The amplitude of the return echo is converted in colour

2.3.4 Ultrasound probes

Ultrasound probes are devices with piezoelectric crystals inside. There are different types of probes, which manly differ in the geometric distribution of the crystals and the frequencies at which they work.
The most commonly used probes are:

- Linear probe: piezoelectric crystals are arranged in a rectilinear array; the frequency range is 5-20 MHz; it is used to investigate small organs and surfaces

- Convex probe: piezoelectric crystals are arranged in a curved array; the frequency range is 2-7 MHz; it is suitable for abdominal vessels, abdominal organs, gynaecology

- Phased array probe: the frequency range is 2-10 MHz; it is mainly used in cardiology

2.3.5 Visualisation techniques

There are different strategies for visualising ultrasound data:

- A-mode (Amplitude mode): no real image is obtained, but a signal with peaks at discontinuities, whose amplitudes are proportional to the echo intensity. No longer used in medicine

- B-mode (Brightness mode): the intensity of return echoes is converted into colour to generate the image. It is a grayscale image and it is used to observe moving organs and structures in real-time

- M-mode (Time motion mode): from the B-mode image, a scan line is chosen and a graph is generated, in which the displacement of each individual interface on this scan line is represented as a function of depth and as a function of time. It is used in cardiology, for instance for evaluating the myocardial contractility
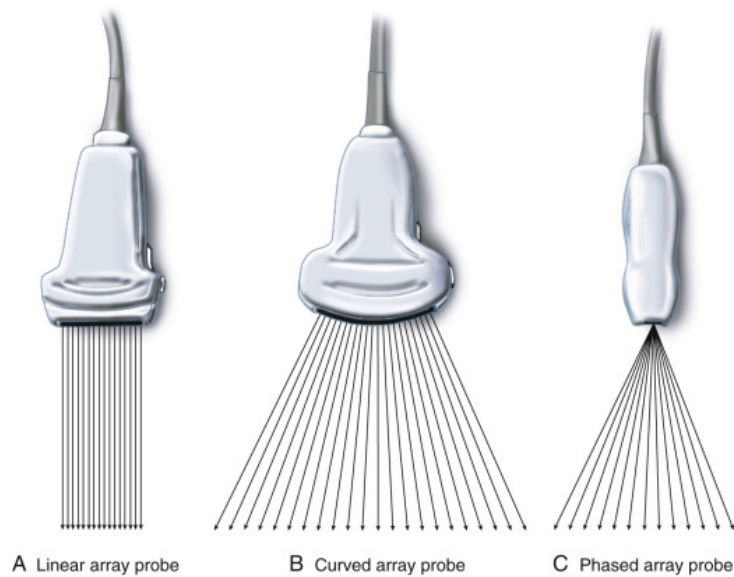
Figure 2.12: *Different types of ultrasound probes*

2.3.6 Ultrasound artefacts

Ultrasound images can be characterised by various artefacts, which can sometimes help in making a diagnosis or can sometimes be a source of error by altering the image.

These artefacts can be caused by the operator who uses the device, such as improper use of the instrument, incorrect scanning technique, inadequate preparation of the patient, but can also result from the interaction between ultrasound and anatomical/biological structures.

The most common artefacts are:

- Reverberation: occurs when the ultrasound beam hits a highly reflective structure perpendicularly. The beam is reflected and hits the probe, from which it is reflected back. This cycle is repeated several times, giving rise to multiple reflection between probe and structure, resulting in echogenic bands spaced by a constant interval and with decreasing intensity.

- Comet tail artefact: it is a particular type of reverberation that is created due to multiple reflections occurring between the front and back wall of the reflective structure. A series of parallel and close echoes are created. They can be due to gases in natural cavities, calcifications, metal catheters, etc...

- Mirror artefact: occurs in the presence of curved, highly reflective interfaces, which act as mirrors. Structures near these interfaces are represented both in their true position and in their mirror position relative to the reflective interface. This effect is due to multiple reflection occurring between the structure and the reflective interface.

- Shadowing: occurs in the presence of a highly absorbent tissue, such as collagen-rich tissues, calcifications. The ultrasound beam is almost totally

reflected by the structure, producing an echo-free zone downstream of it.

- Posterior wall reinforcement: occurs when the ultrasound beam passes through a liquid collection. The ultrasound beam is not attenuated within the liquid collection, so tissues located posterior to it generate more intense echoes than tissues around the liquid formation, consequently appearing more echogenic.

- Side-lobe artefact: occurs due to the secondary beams on the sides of the primary beam emitted by the probe, which have a different direction to the primary beam and lower intensity. The echoes of these beams are visible if the image is predominantly anechogenic and they are positioned in the centre of the image, as they are assumed to derive from the primary beam.

- Lateral refraction shadow: occurs due to the phenomenon of ultrasound refraction. When the beam crosses an interface it is deflected and this causes lateral shadows to appear. Refraction can cause image distortion, leading the operator to misinterpret the image.

- Speed displacement artefact: occurs due to variations in propagation speed of ultrasounds in various tissues. Within liquid and solid structures, the propagation speed of ultrasound decreases and increases, respectively, such that delayed or early return echoes are recorded. This causes the interfaces downstream of the liquid or solid structure to be represented deeper or closer, respectively.

2.3.7   Inferior vena cava echography

To perform the inferior vena cava echography, the patient is placed on a medical couch in a supine position. As said previously, it is important to interpose a layer of gel between the probe and the skin in order to avoid the presence of microbubbles of air that would obstruct the obtaining of the ultrasound image.
The inferior vena cava can be scanned either along the longitudinal axis or along the transverse axis, generally exploiting the subcostal window. To obtain the transverse view, the probe is placed just below the xiphoid process, with the probe marker facing the right side of the patient. In this way, the structures on the right side of the patient are shown on the left of the image, and vice versa. In the ultrasonographic image obtained in this configuration, it is possible to distinguish both the inferior vena cava and the aorta.
To visualise the inferior vena cava in its long axis, the probe is rotated 90° from the transverse view, with the marker pointing in the cranial direction. Thus, the structures present in the cranial direction are shown on the left of the image while the structures present in the caudal direction are shown on the right of the image. In this way, in addition to the inferior vena cava, other structures such as liver, hepatic vein and right atrium can be observed.
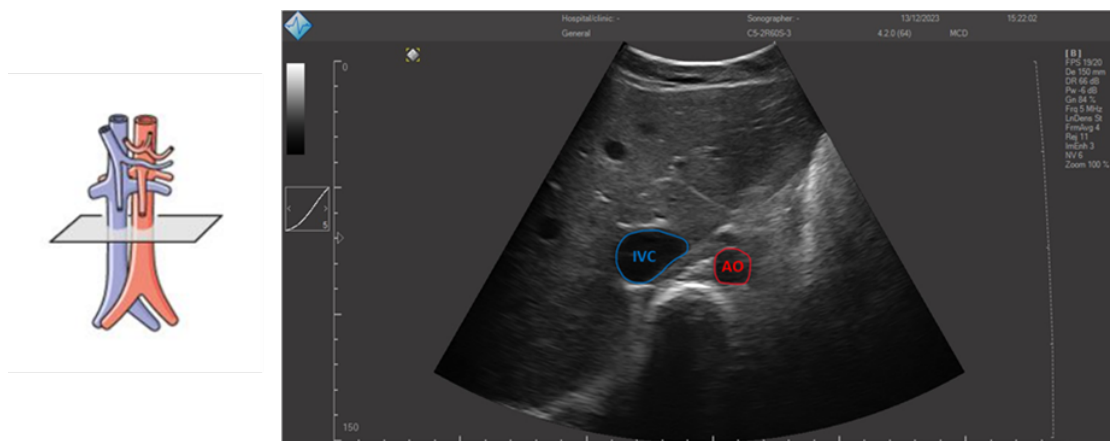
Figure 2.13: *Imaging plane (left) and ultrasonographic image of the IVC scanned along the transverse view (right). It is also possible to observe the aorta, indicated as AO.*
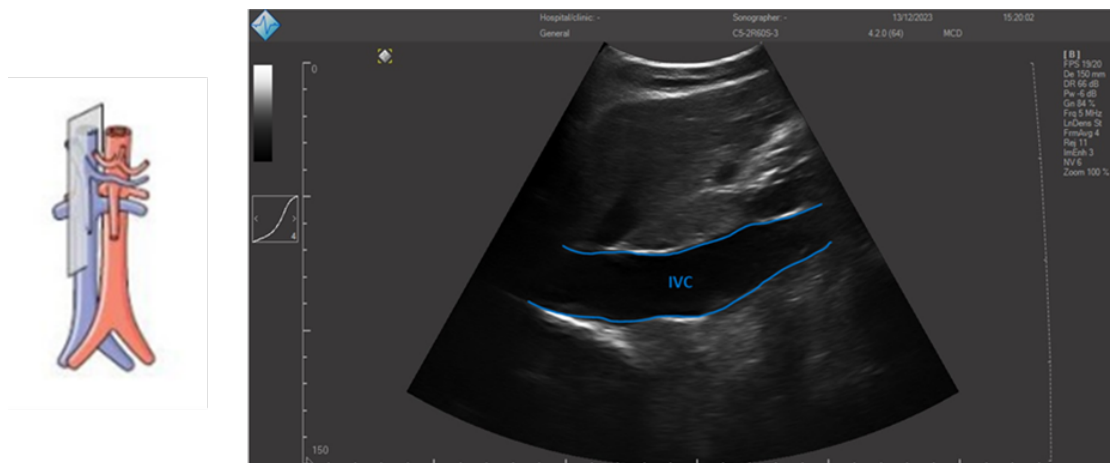
Figure 2.14: *Imaging plane (left) and ultrasonographic image of the IVC scanned along the longitudinal view (right)*

2.4 Current techniques for estimating right atrial pressure

The right atrial pressure (RAP) is the pressure present in the right atrium and coincides with the central venous pressure (CVP), as long as there is no obstruction of the vena cava. In the clinical setting, the determination of RAP is one of the procedures performed for the haemodynamic assessment of patients. Indeed, it allows an estimation of intravascular volume and, consequently, optimisation of patient care and management.

Estimation of volemic status by CVP (or RAP), moreover, can serve as a guide for fluid resuscitation [12].

Normal RAP values range from 1 to 7 mmHg. High RAP values between 10 and 20 mmHg can be found in various cardiac diseases, such as heart failure, constrictive

pericarditis, cardiac tamponade, and in the presence of pulmonary hypertension.

Generally, the estimation of right atrial pressure is obtained through an invasive examination known as 'right heart catheterisation (RHC)': it consists of the insertion, typically through the femoral vein or internal jugular vein, of a catheter that reaches the pulmonary artery. The catheter is made up of several lumens, including one that flows into the right atrium, allowing RAP monitoring.

However, being an invasive procedure, it is not without risks and can lead to a number of complications, such as infection, haematomas, venous thrombosis.

For this reason, several non-invasive techniques have been proposed for the assessment of right atrial pressure, including ultrasound scanning of the inferior vena cava. The pulsatility of the inferior vena cava reflects the patient's volemic state and right atrial pressure [6].

The pulsatility index of the IVC is often expressed by the Caval Index (CI), defined as a relative decrease in the diameter of the inferior vena cava during a respiratory cycle:

$$CI = \frac{D_{max} - D_{min}}{D_{max}} \tag{2.9}$$

where D_{max} is the maximum diameter of the IVC and D_{min} is the minimum diameter of the IVC.

The minimum diameter is calculated during the inhalation phase, during which the negative intra-thoracic pressure increases the venous return to the heart causing the IVC to collapse, while the maximum diameter is calculated during the exhalation phase, during which the intra-thoracic pressure increases, decreasing the venous return and maximising the diameter of the IVC.

Normal breathing conditions, however, may not elicit a collapse of the inferior vena cava. A popular manoeuvre, known as 'sniffing', is often used to induce a rapid decrease in intra-thoracic pressure and consequently a collapse of the IVC. The sniff test involves a strong inhalation through the nose by the patient. Referring to the current guidelines of the American Society of Echocardiography (ASE), it is possible to have an estimate of RAP as a function of inferior vena cava diameter and its pulsatility, obtained through the sniff test [13], as shown in Tab. 2.2.

Variable	Normal RAP [0-5 mmHg]	Intermediate RAP [5-10 mmHg]		High RAP [10-20 mmHg]
IVC max diameter	≤ 2.1 cm	≤ 2.1 cm	> 2.1 cm	> 2.1 cm
Collapse with sniff	> 50 %	< 50 %	> 50 %	< 50 %

Table 2.2: *ASE guidelines to estimate RAP through IVC diameter and its collapsibility with sniff*

Nevertheless, the sniff manoeuvre is not standardised, as the manner and extent of this breathing varies from subject to subject depending on the age and clinical condition of the patient, and therefore this technique may lead to an unreliable and poorly reproducible estimate of right atrial pressure.
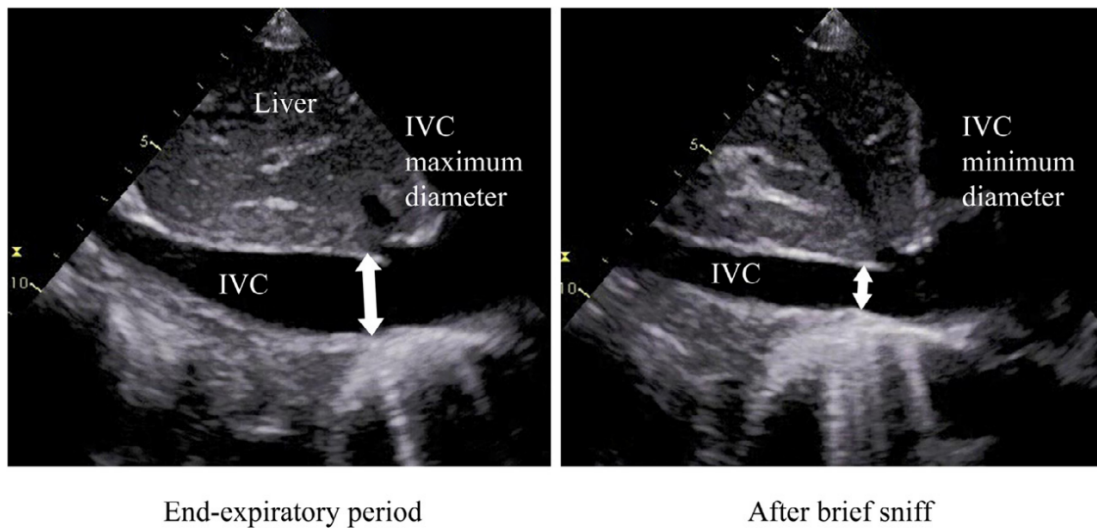
Figure 2.15: *IVC diameter evaluated at the end-expiratory period (left) and after a brief sniff (right) in long-axis view [1]*

In conclusion, ultrasound imaging of the inferior vena cava represents a viable alternative to invasive monitoring of right atrial pressure, due to its advantages such as low cost, high availability, use of harmless radiation, and ease of use.

On the other hand, however, the estimation of RAP using this methodology is affected by variability that depends on both the patient and the operator. Part of this variability is due, for instance, to the sampling position of the IVC, the displacements of the IVC during the respiratory cycle, and the individual breathing manoeuvre [14].

Chapter 3

Material and Methods

In this thesis, several instruments and software were used for data acquisition and processing.

3.1 Echography

The ultrasound scanner used to scan the inferior vena cava of subjects undergoing the experimental test is the MicrUs EXT-1H, that is manufactured by Telemed. It is a portable ultrasound scanner with an open architecture, which is powered via a USB connection. It is therefore very versatile, as it can be connected to several devices, such as personal computers, smartphones, tablets.

It allows the use of a wide rage of multi-frequency transducers, from 2 to 15 MHz, enabling high-quality images to be obtained in various clinical scenarios, such as general, abdominal, obstetric-gynaecological, urological ultrasound. The supported ultrasound probes are linear, convex, microconvex and endocavitary, and, depending on the probe used, the scanning depth can vary from 2 to 31 cm. The ultrasound scanner provides different imaging strategies, including B-mode and M-mode. The ultrasound image is encoded in 256 grayscales and its size is optimised on the basis of the monitor resolution. Images can be saved in various formats, including AVI, BMP, TIFF, DICOM.

The MicrUs EXT-1H is supplied with the Beamformer, or base unit; the USB cable, through which the base unit is connected to the PC; the USB key, containing user manual, installation and set-up manual, software; customer-selected probes purchased separately.

3.1.1 Ultrasound probe

The probe used for ultrasound scanning is the C5-2R60S-3, that is a convex probe manufactured by Telemed.

The piezoelectric crystals are S3-type and the probe works in a frequency range of 2-5 MHz. It is characterized by a bending radius of 65 mm and a field of view of 60°.

It is mainly used in abdominal ultrasound, obstetrics and gynaecology, and paediatrics.

Figure 3.1: *MicrUs EXT-1H [2]*

Figure 3.2: *Convex probe C5-2R60S-3 [2]*

3.1.2 EchoWave II software

The portable ultrasound scanner is managed by the Echo Wave II scanning software, which features a simple and intuitive interface through which the user can view the ultrasound image and modify the scan mode parameters to improve image quality. In addition, the software allows remote control for training, service and technical support.

At the centre of the user interface there is the image display area, which contains both the actual ultrasound image and some information about, for example, scan parameters and measurement results.

The most important parameters to be set in order to obtain a high-quality image are: scan depth, focus, dynamic range, gain and TGC.

The scanning depth regulates the depth of the field of view, and it should be modified depending on the structures to be analysed. For instance, to scan larger or deeper structures, the depth must be increased. After setting the depth, the other parameters can be adjusted. The focus is adjusted immediately after the scanning depth. It optimies the image by increasing the resolution on specific zones. Through the use of markers, the number of zones and the depth of focus

41
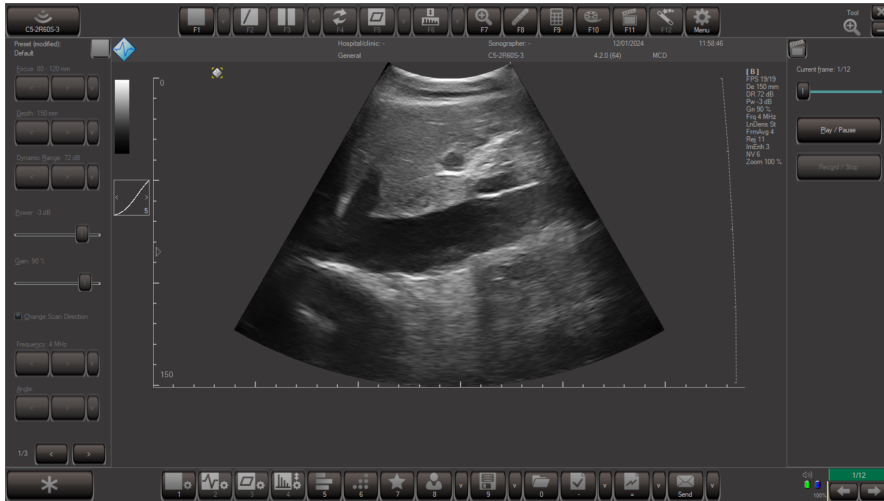
Figure 3.3: *User interface of EchoWave II software*

can be selected. It is essential that these markers are in the centre of the region to be investigated.

The dynamic range adjusts the logarithmic amplification of the return signal, allowing the simultaneous visualisation of very strong and very weak echoes. It is a parameter that mainly affects the contrast of the image: low values increase contrast and vice versa.

Finally, gain and TGC regulate the amplification of return echoes. Specifically, gain evenly amplifies or reduce return echoes, thus making the image brighter or darker, while TGC amplifies return signals as a function of depth. As depth increases, the gain level increases, so that the brightness of surface field decreases and the brightness of the deep field increases.

Furthermore, in order to attenuate noise in the ultrasound image and obtain a high-quality image, the user can use operations such as Frame Averaging and Rejection, or various Speckle Reduction Imaging algorithms. The software also provides several Presets that the user can choose depending on the probe and the type of examination to be conducted. Alternatively, the user can create a new Preset to store the scan parameters and use it for subsequent scans.

3.2 VIPER

Ultrasonography of the inferior vena cava provides relevant information on the patient's clinical condition, e.g. on volemic status and right atrial pressure. However, the calculation of the diameter and pulsatility of the IVC is made difficult due to three main problems: irregular geometry, displacement of the vein caused by respiratory and cardiac movements, and poor repeatability of measurements due to intra- and inter-operator variability [3].

VIPER is a semi-automated tracking algorithm of the inferior vena cava, implemented in Matlab. It allows to analyse the inferior vena cava along both the longitudinal and transverse axis and, always following the same sections of the

vessels by compensating for IVC movements, is able to provide more precise and reliable estimates, thus aiding doctors in diagnosis and monitoring.

Figure 3.4: *VIPER logo [3]*

The algorithm takes the ultrasound video clip as input and processes each frame. In the first frame, the user must indicate certain information required for processing. For the analysis in transverse view, only the centre of the vein needs to be indicated. For the analysis in longitudinal view, on the other hand, the operator must select two reference points, the initial part of the vein from which to start the analysis by selecting two points that are respectively on the upper and lower edge of the vein, and finally a segment indicating the final part of the vein.
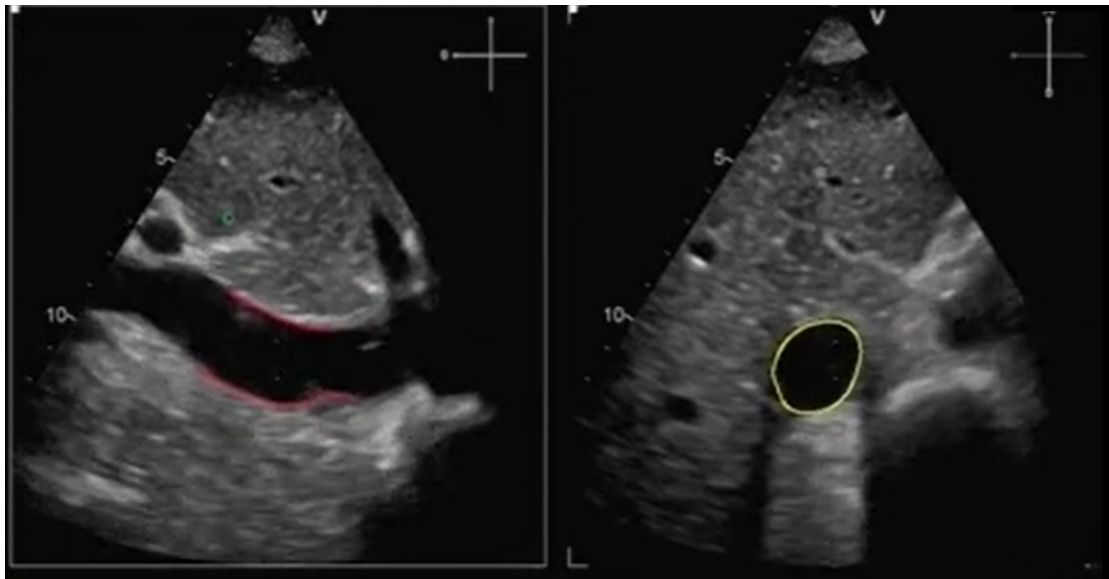
Figure 3.5: *Example of a frame of the ultrasound videoclip in which the IVC is correctly segmented by the algorithm along both the longitudinal axis (left) and transverse axis (right). On the left image the edges of the IVC are indicated in red, on the right image the edges of the IVC are indicated in yellow [3].*

3.3 Spirometer

In this project, a spirometer was designed using 'Autodesk Fusion 360' software, which was then 3D printed with nylon PA12 as printing material, with the aim of

improving the model created in a previous thesis.

The old spirometer consisted of two Venturi tubes arranged in cascade, with a net placed between them to reduce the turbulence generated by the first tube. One of these tubes had three pins to which two differential pressure sensors were connected. However, this model has some limitations:

- Large dimensions, which increases the dead space in addition to the physiological one. As a result, the subject has to move a greater mass of air to breathe, causing possible breathlessness if several consecutive breathing cycles are required

- The subject has to exert effort to breathe, making the ultrasound scan of the IVC more difficult

- It is not easy to handle, given its overall length and the presence of the stapled net

- Asymmetry. To measure a bidirectional air flow, the spirometer must be symmetrical with respect to the central pin connected to the two pressure sensors.
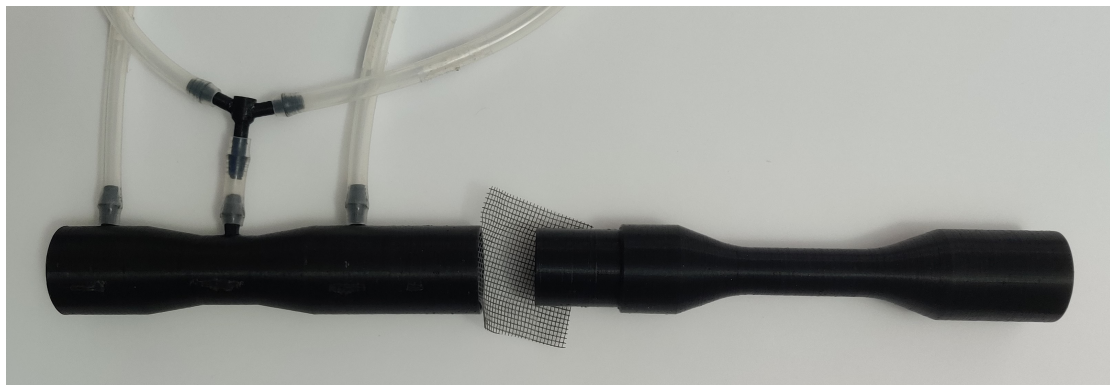
Figure 3.6: *Old spirometer*

The new spirometer consists of a circular Venturi tube with a length of 14 cm. At the inlet and outlet of the tube, the outer and inner diameters are 3.2 cm and 2.5 cm respectively, while at the constriction in centre of the tube the diameters are 2.5 cm and 1.75 cm respectively.

The instrument is characterized by three pins to which two differential pressure sensors are connected, through which it is possible to obtain differential pressure signals and consequently flow signals, in order to distinguish the inhalation and exhalation phases. The three pins are equally spaced every 4.5 cm starting 2.5 cm from the tube inlet.

In order to reduce the the size of the vortices that can be generated due to the inversion of the flow of inhaled and exhaled air, two appendages with a grid equipped with 2 mm diameter circular holes were attached to the two ends of the tube. For each appendage, one end of it partially enters the Venturi tube for a total length

of 1 cm, while the disposable mouthpiece with a diameter of 2.8 cm is inserted at the other end.
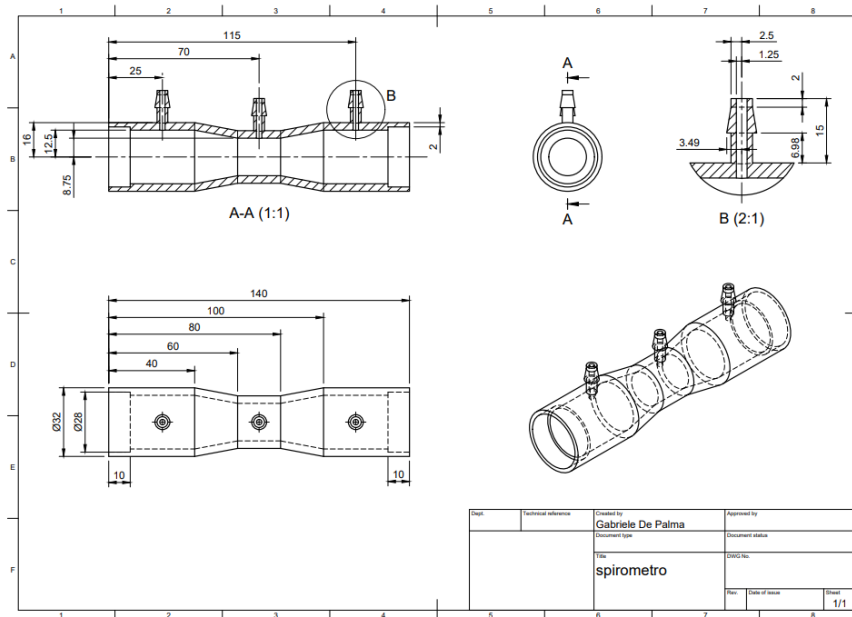
Figure 3.7: *Design of the spirometer*
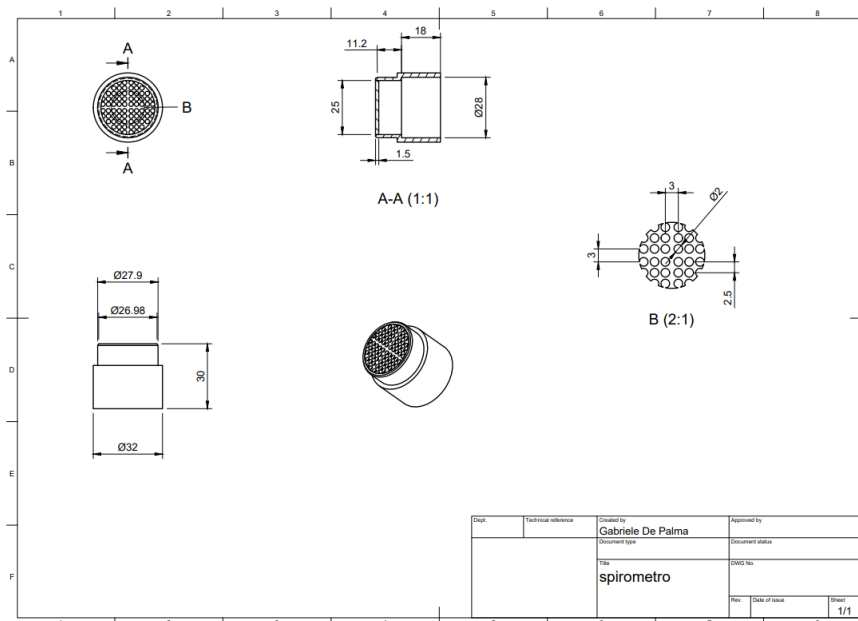
Figure 3.8: *Design of the two appendages*

The spirometer thus realised has a total length of 18 cm and has been specially designed symmetrically with respect to the central pin, in order to have the same condition of fluid motion during inhalation and exhalation and to measure airflow in both directions [15].

45

The small size of the device allows it to be easily handled in the clinic and does not introduce a large dead space other than the physiological one (mouth, nose, trachea, bronchioles).

Finally, a handheld grip, characterised by four grooves for finger placement, has been designed, which can be attached to the spirometer to improve its grip and make the spirometer easier to use.

Figure 3.9: *3D representation of the spirometer and handheld grip*

3.3.1 Differential pressure sensors

The two sensors used in combination with the spirometer to obtain the differential pressure signals, and subsequently the flow signals, are the SDP816-125PA manufactured by Sensirion. They are based on CMOSens technology, whereby the sensor element is coordinated with the digital and analogue signal processing electronics on a small CMOS chip. The supply voltage can vary from 2.7 to 5.5 V. The pressure range is ±125 Pa, so the sensor can measure a differential pressure between -125 Pa and +125 Pa. It is capable of working at a temperature between -40°C and +80°C.

It is a ratiometric sensor, so the output depends on the voltage with which the sensor is supplied. The output signal is a voltage signal, and the formula in the sensor datasheet must be used to convert it into the differential pressure signal.

Figure 3.10: *Sensirion SDP816-125PA differential pressure sensor [4]*

The conversion formula varies depending on the output curve selected, and there are two options:

- Linear: the sensor is not fully bi-directional and the dynamics vary from -10% to +100% of full range.
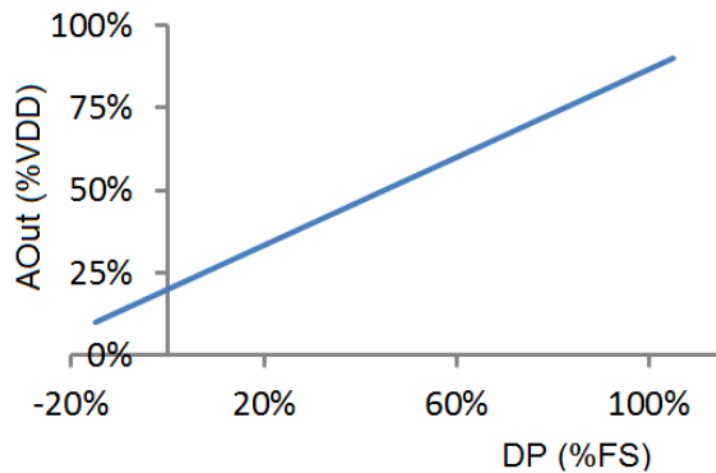
Figure 3.11: *Linear output curve*

The formula for obtaining the differential pressure value is as follows:

$$DP = \frac{190 \cdot AOut}{VDD} - 38 \tag{3.1}$$

where DP is the differential pressure in Pascal, $AOut$ is the analog output in Volt and VDD is the supply voltage in Volt.

- Square root: the sensor is fully bi-directional, so the dynamics range from -100% to +100%. In this configuration, the output has a more stable zero point and greater sensitivity at small pressures.

47
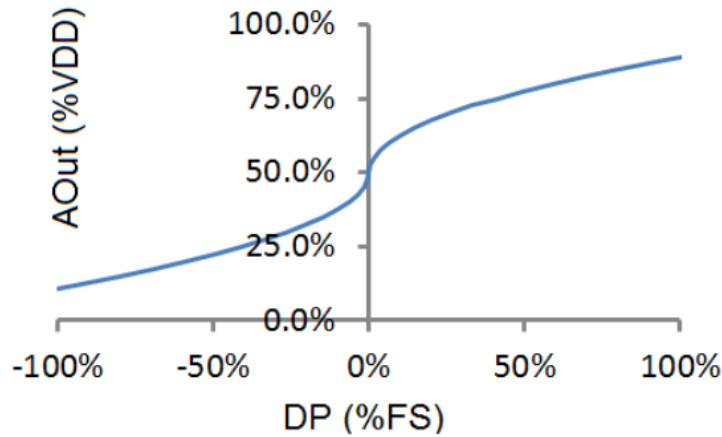
Figure 3.12: *Square root output curve*

The formula for obtaining the differential pressure value is as follows:

$$DP = sign\left(\frac{AOut}{VDD} - 0.5\right) \cdot \left(\frac{AOut}{VDD \cdot .4} - 125\right)^2 \cdot 133 \qquad (3.2)$$

where *sign* is the sign function, *DP* is the differential pressure in Pascal, *AOut* is the analog output in Volt and *VDD* is the supply voltage in Volt.

In this project, the two pressure sensors measure the pressure difference between constriction and inlet and between constriction and outlet of the spirometer, respectively.
According to the continuity equation, the flow rate of a fluid flowing in a pipe with a variable cross-section remains constant, and the flow rate can be expressed as the product of pipe cross-section and fluid velocity:

$$A \cdot v = cost \qquad (3.3)$$

where *A* is the pipe cross-section and *v* is the fluid velocity.
As the spirometer narrows, therefore, the fluid velocity increases as the cross-sectional area decreases.
Furthermore, the Venturi effect states that the fluid pressure decreases as the fluid velocity increases, according to the following law:

$$p + \frac{1}{2}\rho v^2 = cost \qquad (3.4)$$

where *p* is the fluid pressure, ρ is the fluid density and *v* is the fluid velocity.
This implies that, at the constriction of the spirometer, the pressure decrease as the fluid velocity increases.
Thus, the pressure evaluated at the inlet and outlet of the spirometer is always greater than that evaluated at the constriction. Therefore, the two sensors always measure negative differential pressure values.
Following these observations, the quadratic output curve was selected.
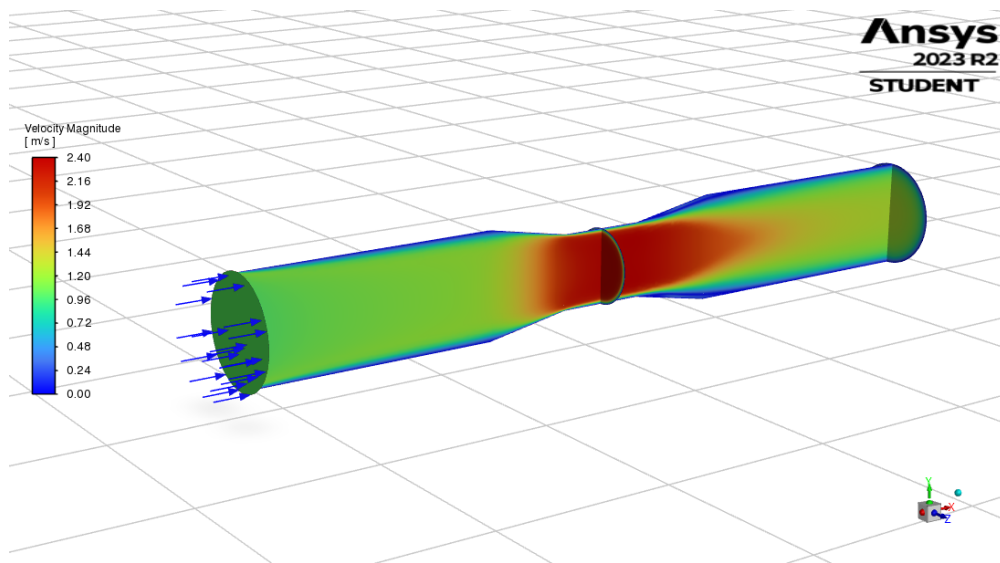
Figure 3.13: *Air velocity distribution inside the spirometer, obtained by means of computational fluid dynamics analysis. At the narrowing of the tube, the air velocity reaches its maximum value.*
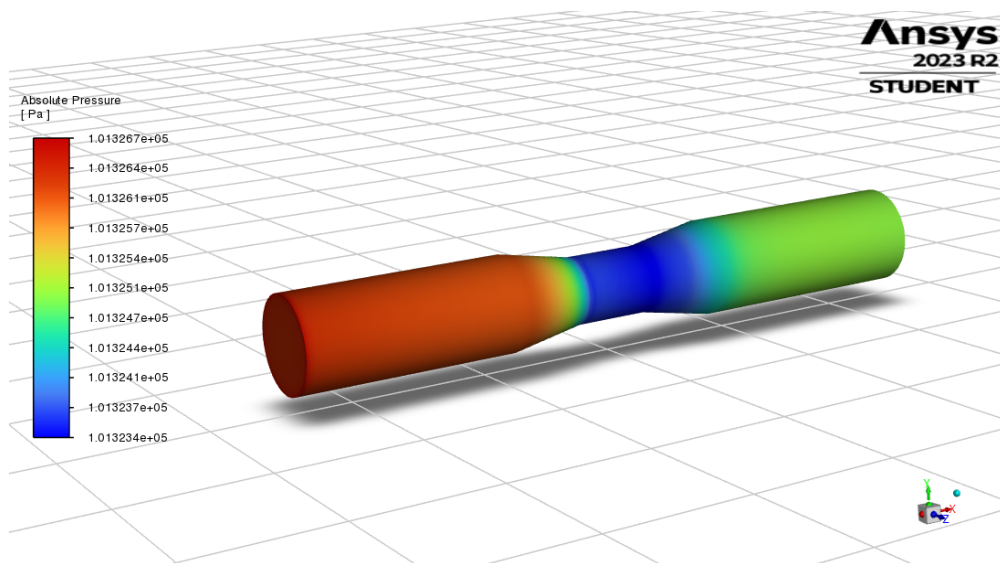
Figure 3.14: *Air pressure distribution inside the spirometer, obtained by means of computational fluid dynamics analysis. At the narrowing of the tube, the air pressure reaches its minimum value.*

3.3.2 Data acquisition board

The USB 6001 data acquisition board (DAQ) from National Instruments was used to observe real-time signals on Matlab, acquired via the sensors. It is a low-cost, multi-functional data acquisition board that allows signals to be generated and acquired. It is equipped with a 14-bit analogue-to-digital converter (ADC) and a 32-bit counter. The board features a sampling rate of 20 kS/s. There are 8

single-ended and 4 differential input channels, with an operating voltage range of ± 10 V, and 2 output channels, with a voltage range of ± 10 V. Finally, the DAQ is connected to the PC via a USB connection, allowing data transfer and visualization.

Figure 3.15: *National Instruments USB 6001 data acquisition board [5]*

The two differential pressure sensors are supplied with +5V and they are connected to two different DAQ input channels, known as Analog Input 0 (AI0) and Analog Input 1 (AI1).

Channel AI0 relates to the sensor that measures the pressure difference between the constriction and the outlet of the spirometer, while channel AI1 relates to the sensor that measures the pressure difference between the constriction and the inlet (on the mouthpiece side) of the spirometer.

3.3.3   Signal processing

The output signals of the sensors are positive voltage signals, as shown in Fig. 3.17, and it can be seen that the two signals alternate during the inhalation and exhalation phases. The blue signal is related to channel AI0 and the red signal is related to the channel AI1.

Using the formula 3.2, associated with the quadratic output curve of the sensors, it is possible to convert voltage signals into differential pressure signals. Observing the pressure signals, it possible to notice that they are negative, as the pressure at the constriction is less than the pressure at the inlet and outlet of the spirometer. Furthermore, during the inhalation phase, the pressure difference between constriction and outlet, indicated as DP_{AI0}, is greater. This is explained by the fact that air must enter the lungs by a pressure gradient, and therefore the pressure at the inlet of the spirometer is smaller than at the outlet of the spirometer. On the other hand, exactly the opposite occurs during exhalation as the air has to escape to the outside environment, so the pressure at the inlet of the spirometer is higher than the pressure at the outlet. Therefore, the pressure difference between constriction and inlet, indicated as DP_{AI1}, is greater.
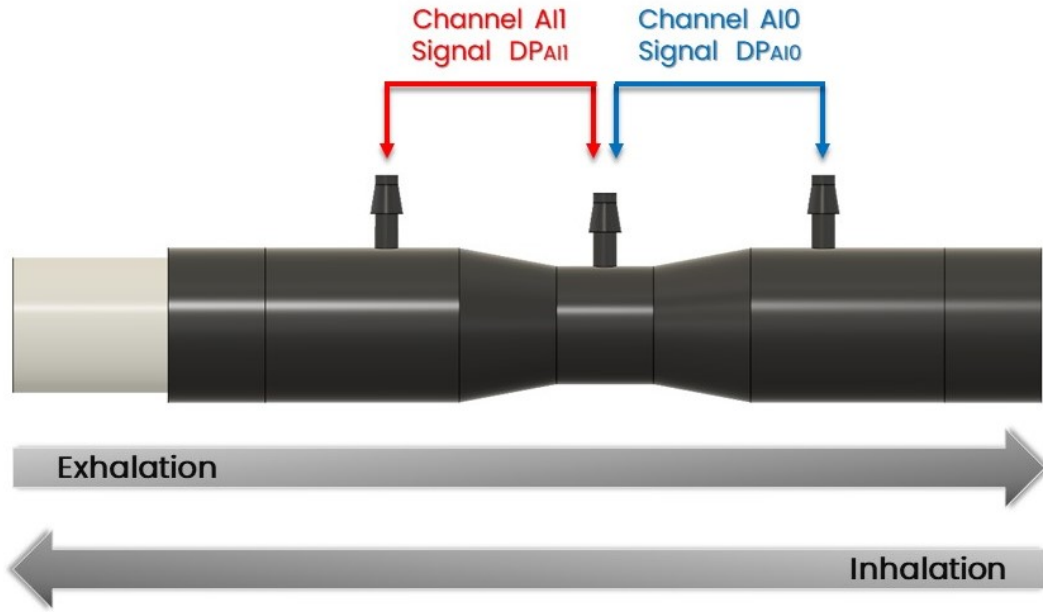
Figure 3.16: *Representation of the spirometer and the DAQ channels to which the differential pressure sensors are connected*

Finally, by setting up the continuity equation and the Bernoulli's equation, neglecting the geodetic pressure term, the flow signals can be obtained. The flow can be derived as follows:

$$F = sign(|DP_{AI1}| - |DP_{AI0}|) \cdot A_2 \cdot v_2 =$$
$$= sign(|DP_{AI1}| - |DP_{AI0}|) \cdot A_2 \cdot \sqrt{\frac{2 \cdot |DP|}{\rho \left[1 - \left(\frac{A_2}{A_1}\right)^2\right]}} \qquad (3.5)$$

where A_2 and v_2 are the pipe cross-section and fluid velocity at the constriction, respectively, and A_1 is the pipe cross-section at the inlet/outlet.
The *sign* function is used to conventionally set a negative flow during the inhalation phase and a positive flow during the exhalation phase. Indeed, during inspiration, the absolute value of the DP_{AI1} term is less than the absolute value of the DP_{AI0} term, so the sign function returns the value -1. Conversely, during expiration, the absolute value of the DP_{AI1} term is greater than the absolute value of the DP_{AI0} term, so the sign function returns the value +1.

Analysing the differential pressure signals, it is evident that during the transitions between the two phases of breathing, with the reversal of air flow through the spirometer, positive differential pressure peaks occur. This leads to the possibility that during inhalation the flow becomes positive, while during exhalation it becomes negative. Consequently, in order to reduce such artefacts, additional conditions were introduced for the calculation of flow signals:

- If the absolute value of the DP_{AI0} term is greater than the absolute value

51
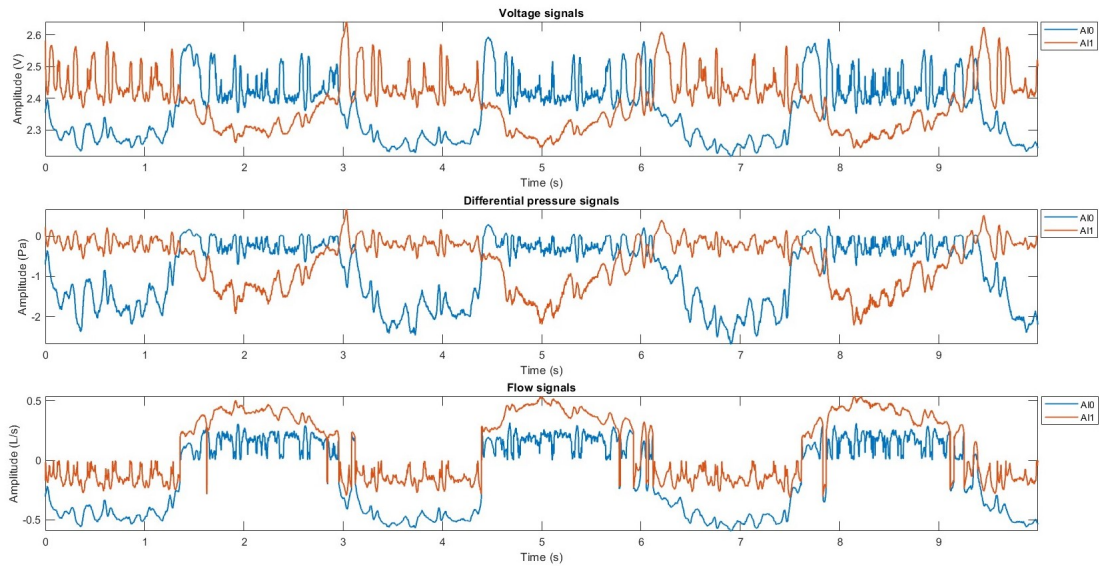
Figure 3.17: *Voltage, differential pressure and flow signals*

of the DP_{AI1} term and the DP_{AI0} term is positive, the resulting flow is considered positive since it corresponds to the expiration phase

- If the absolute value of the DP_{AI1} term is greater than the absolute value of the DP_{AI0} term and the DP_{AI1} term is positive, the resulting flow is considered negative since it corresponds to the inspiration phase

Furthermore, taking into account short pauses during breathing acts and/or light breathing, it is possible that the pressure differences detected by the two sensors are very small, causing the two pressure signals to overlap and generating the previously described artefacts in the respective flow signals.(In particular, it could occur that during inspiration the flow becomes positive and during exhalation the flow becomes negative).

In order to eliminate the presence of such artefacts, a 2nd-order Butterworth low-pass filter with a cut-off frequency of 2 Hz was applied to the differential pressure signals before calculating the flow signals. The filtering of the differential pressure signals takes place in blocks of 100 samples, whereby the delayers derived from filtering one block are used to filter the next block in order to eliminate transients. However, working in real time, it is not possible to implement a double-pass filter to eliminate the delay introduced by the filter between the raw and filtered signal. Therefore, a balance must be found between filtering quality and delay. For this reason, an infinite impulse response (IIR) filter was chosen instead of a finite impulse response (FIR) filter. Using a FIR filter would require a higher order to achieve the same performance, causing a more significant delay.

In Figs. 3.18 and 3.19, the effect of filtering can be seen in the differential pressure and flow signals, respectively.
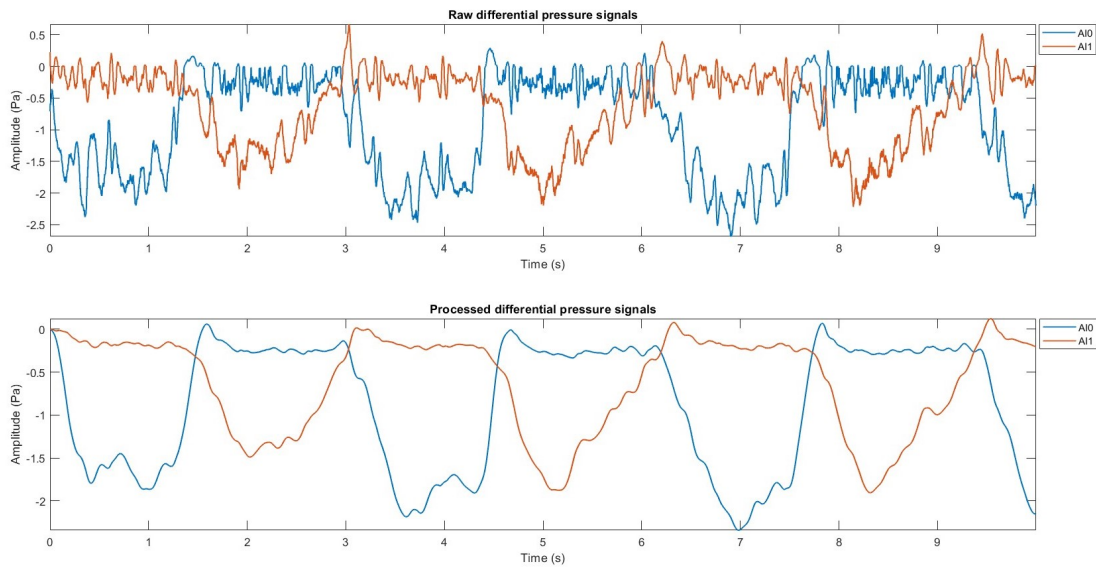
Figure 3.18: *Effect of filtering on differential pressure signals*
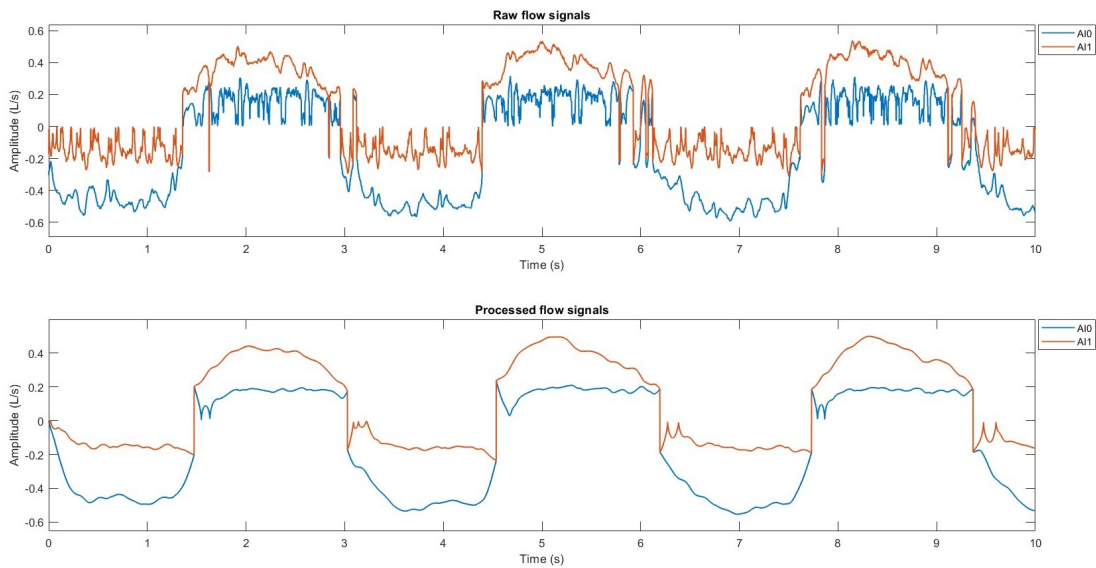
Figure 3.19: *Effect of filtering on flow signals*

One of the main purposes of developing the spirometer is to provide the subject with visual feedback in real time during the test, thus allowing visual guidance in the correct execution of the respiratory manoeuvre by displaying flow signals. However, the simultaneous display of the two signals could be confusing and compromise the correct execution of the test. For this reason, it was decided to combine the two signals in order to obtain and display a single flow signal. Referring to Fig. 3.19, for the inhalation phase the blue signal is taken into account while for the exhalation phase the red signal is taken into account. The single flow signal

can be obtained as follows:

$$F = \begin{cases} F_{AIO}, & sign(|DP_{AI1}| - |DP_{AI0}|) = -1 \\ F_{AI1}, & sign(|DP_{AI1}| - |DP_{AI0}|) = +1 \end{cases} \tag{3.6}$$

where F_{AI0} corresponds to the flow obtained from the differential pressure signal DP_{AI0} and F_{AI1} corresponds to the flow obtained from the differential pressure signal DP_{AI1}.
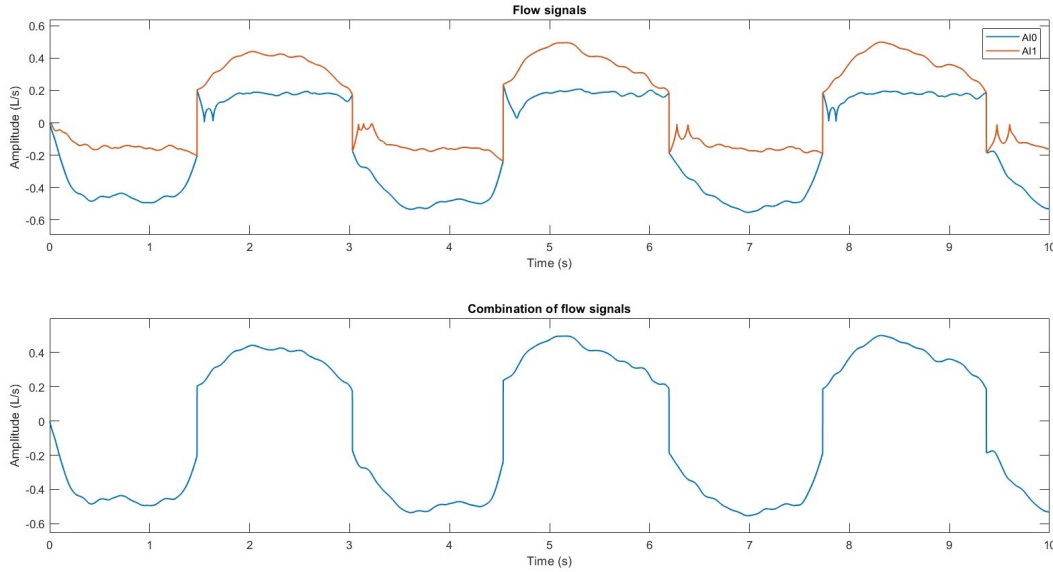
Figure 3.20: *Flow signal obtained by combining the two flow signals*

3.3.4   Approximations and simplifications

It is essential to highlight that the two equations used to calculate flow signals, namely the continuity equation and the Bernoulli's equation, are only applicable under certain conditions, which are not met in the present context. More precisely, the continuity equation assumes incompressible fluids, or those with constant density, whereas air, being an easily compressible fluid, does not fall into this category. Bernoulli's equation, on the other hand, is only valid for ideal fluids, i.e. incompressible, non-viscous fluids, in stationary motion.

Furthermore, pressure losses, which occur during the passage of the fluid through the spirometer, have not been taken into account. These losses can be attributed either to geometric variations in the pipe (localised head losses) or to friction (distributed head losses).

3.3.5   CFD analysis

A CFD analysis was performed using 'Ansys Fluent' software, simulating the motion of the fluid during the exhalation phase under stationary conditions. Although this simulation does not faithfully represent reality, its main objective is to highlight the pressure and velocity distributions and the effect of the screens

on the flow.

To model turbulence, the standard κ-ϵ model was used, which introduces two additional equations on turbulent kinetic intensity transport and turbulent kinetic energy dissipation rate transport, in addition to the continuity and momentum equations.

A velocity of 2 m/s was set at the inlet along the duct axis, a pressure equal to atmospheric pressure was set at the outlet, and a non-slip velocity was set at the surfaces.

The mesh is shown in Fig. 3.21, which subdivides the fluid domain into many small cells within which the equations of motion are solved. Tetrahedrons with a dimension of 1.25 mm were used to generate the mesh.
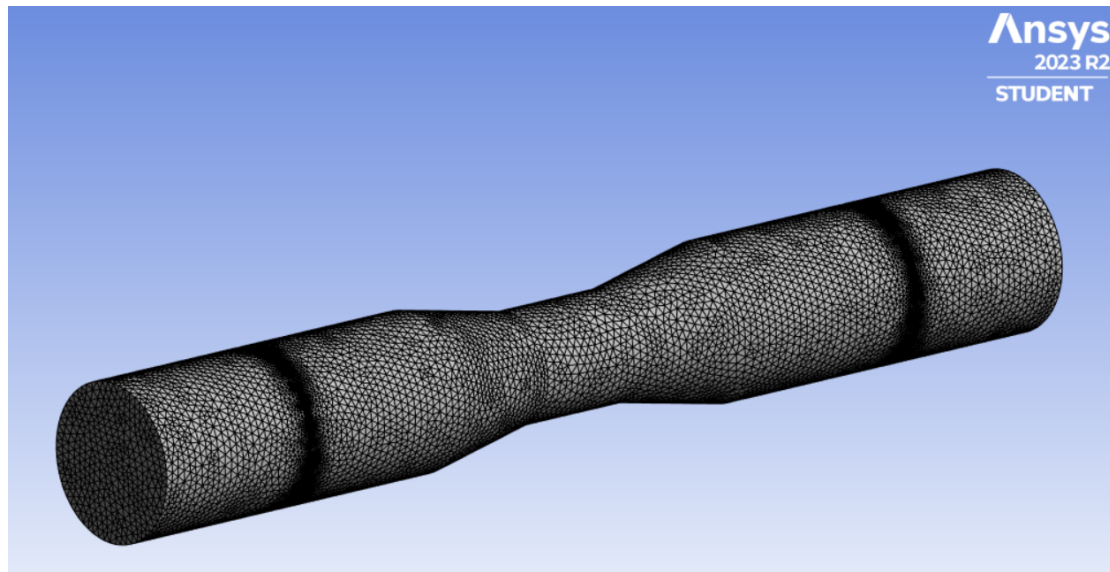
Figure 3.21: *Mesh of the spirometer*

The pressure distribution is shown in Fig. 3.22. Examining only the Venturi tube, thus excluding the two appendages with the grids, it can be seen that at the restriction of the tube the pressure reaches its minimum. Furthermore, due to the pressure losses occurring in the duct, the pressures measured upstream and downstream of the restriction are different. Considering also the two appendages placed at the ends of the Venturi tube, it can be seen that the two grids, mainly used to reduce the size of the vortices that can be created due to the inversion of the inhaled and exhaled air flow, also represent in part an obstruction to the flow, thus causing a pressure drop.

The velocity vectors are shown in Fig. 3.23 . Examining only the Venturi tube, thus excluding the two appendages with the grids, it can be seen that at the narrowing of the tube, the velocity reaches its maximum. Considering the effect of the grids, it can be seen that the fluid velocity increases as it passes through the holes of the grids, with the formation of small recirculation zones immediately downstream of the grids. To limit the pressure drop and the size of the recirculation zones caused by the presence of the grids, a grid with high porosity, i.e. with a large number of holes, was designed. Such a grid, as opposed to one with

a small number of holes, makes it possible to reduce the pressure drop and the size of the recirculation zones, which could have otherwise altered the differential pressure measurements, and to achieve a more uniform velocity field downstream of the grid.
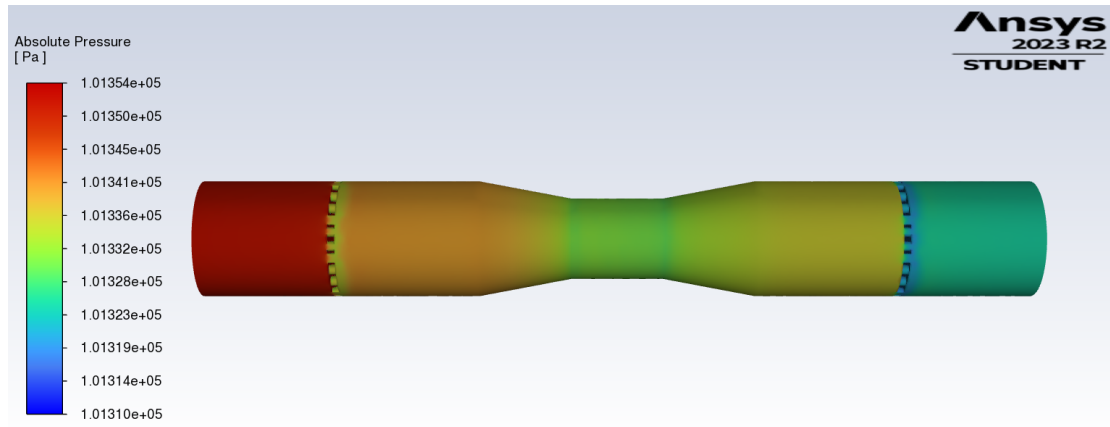
Figure 3.22: *Pressure distribution*
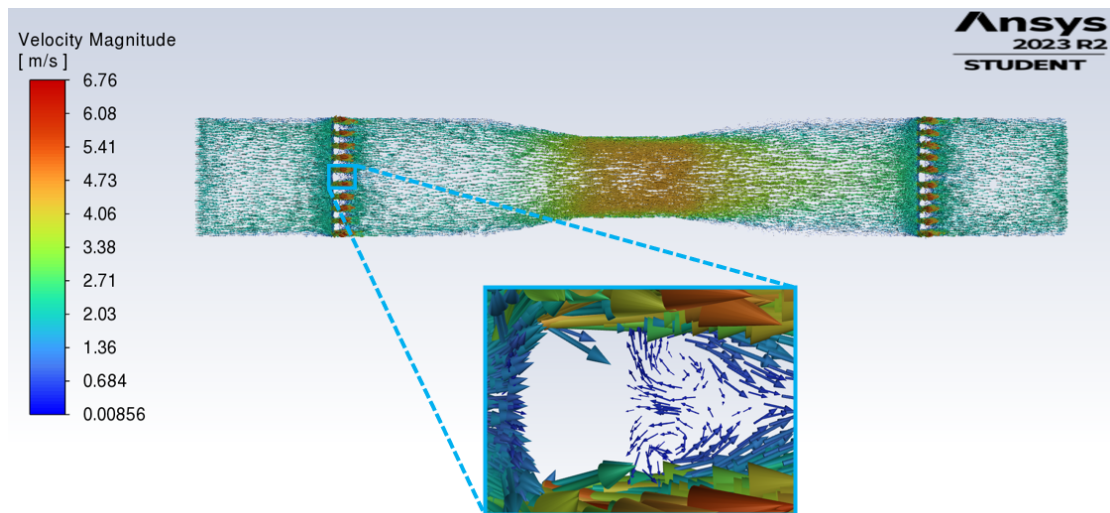
Figure 3.23: *Velocity vectors and details of recirculation zones*

3.3.6 Final setup

The final setup is illustrated in Fig. 3.24. The spirometer is connected to the two differential pressure sensors, which are in turn connected to the DAQ. The latter is connected to the personal computer via a USB connection.

Nº	ITEM
1	Handheld grip
2	Spirometer
3	Disposable mouthpiece
4	Differential pressure sensors
5	DAQ
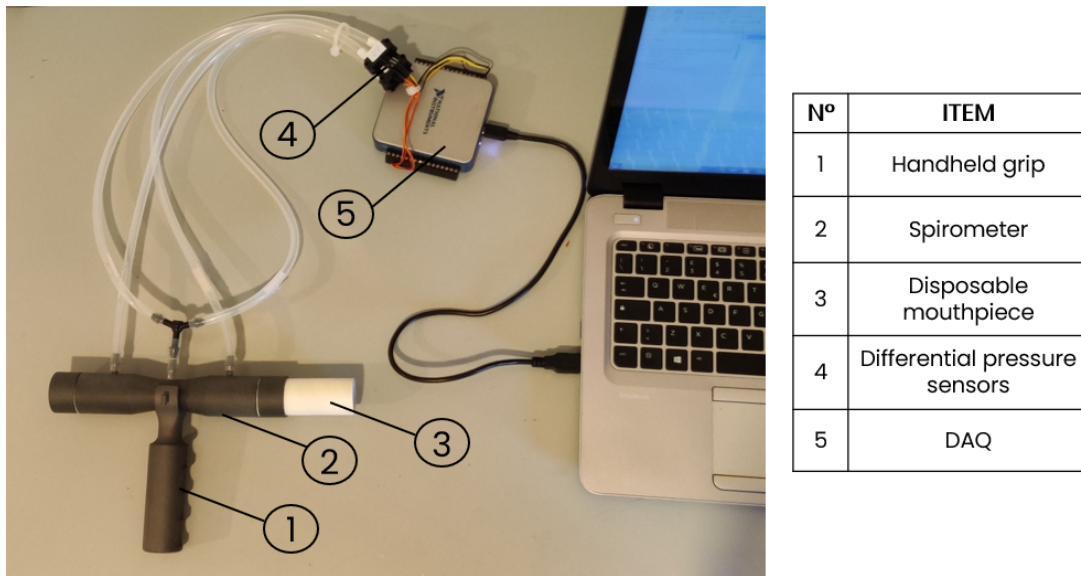
Figure 3.24: *Final setup for data acquisition with the spirometer*

3.4 Graphical user interface

A graphical user interface was developed using Matlab's 'App Designer' environment. This environment offers a wide range of widgets, including buttons, text boxes, numeric fields, drop-down lists and figures, which allow an interactive graphical user interface to be created. The user interface developed in this project consists of two panels called 'Patient Information' and 'Acquisition'. In the first panel called 'Patient Information', shown in Fig. 3.25, the operator enters the personal data of the analysed patient, such as patient ID, first name, last name, gender, age, height and weight. Once all fields have been completed, the operator presses the 'Click to confirm' button to save the data and a folder is automatically created on the computer's desktop, the name of which contains the name and surname of the subject in question. This folder will contain all the files relating to the tests performed with the subject. Subsequently, the operator switches to the second panel called 'Acquisition', shown in Fig. 3.26, where he/she enters the number of the test to be performed in the 'Trial' field and presses the 'START' button to start data acquisition. While the test is being performed, the subject visualises the signal obtained by the spirometer in real time. Finally, at the end of the acquisition, the file relating to the test just performed is saved in the subject-specific folder created earlier.

Figure 3.25: *First panel of the graphic interface visualised by the operator, in which the personal data of the analysed subject are entered: patient ID, first name, last name, gender, age, height and weight.*
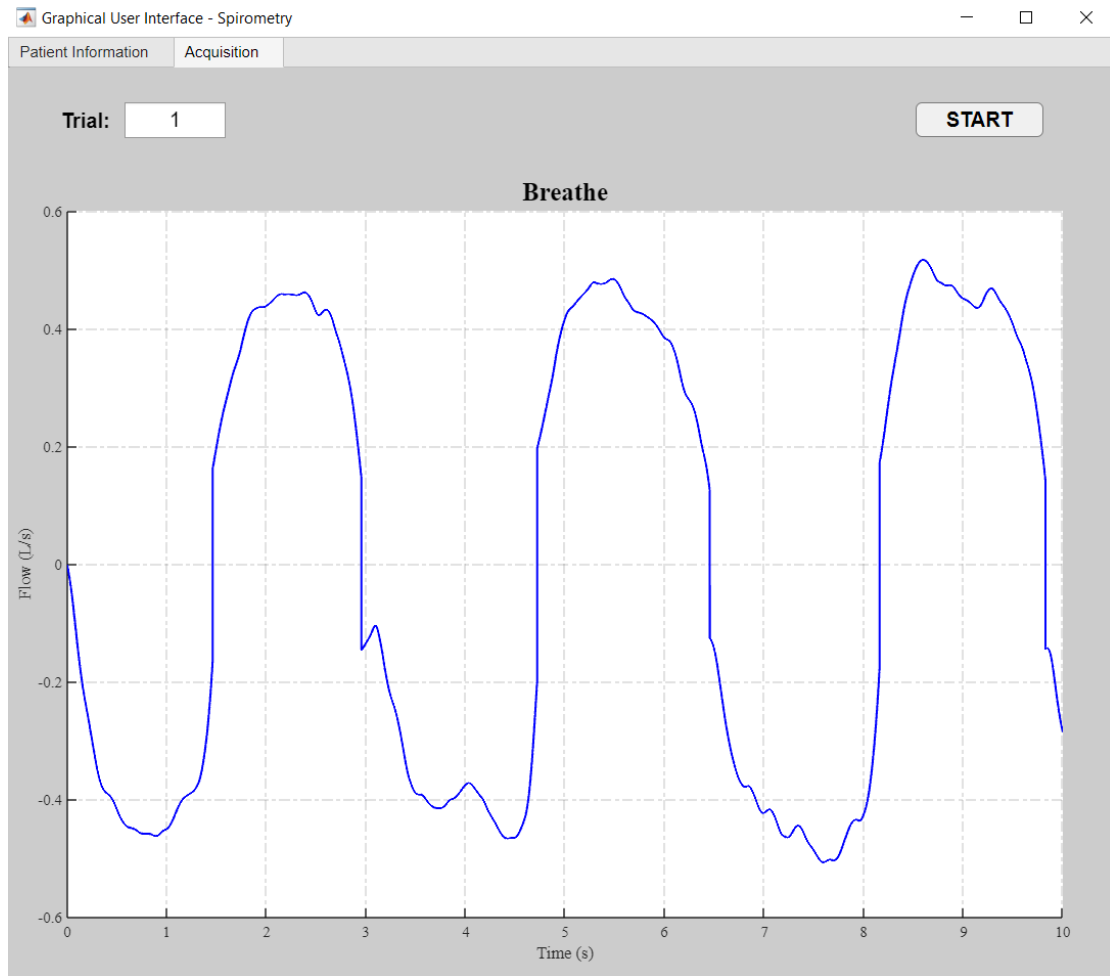
Figure 3.26: *Second panel of the graphic interface visualised by the operator, in which the number of the test to be performed is entered, the acquisition is started and the subject observes the signal obtained by the spirometer in real time.*

Chapter 4

Experimental Protocol

In order to avoid invasive procedures for the measurement of right atrial pressure or the use of non-standardised techniques, the present study proposes an experimental protocol characterised by non-invasive, rapid and comfortable measurements for both the operator and the subject under examination. Furthermore, through the use of a classifier, this protocol could facilitate the estimation of right atrial pressure.

This experimental protocol aims to evaluate the changes in pulsatility of the inferior vena cava under different controlled breathing conditions. After a series of pilot tests aimed at examining the feasibility of the designed experimental procedures, it was decided to analyse the dynamics of the inferior vena cava under light, normal and deep breathing conditions.
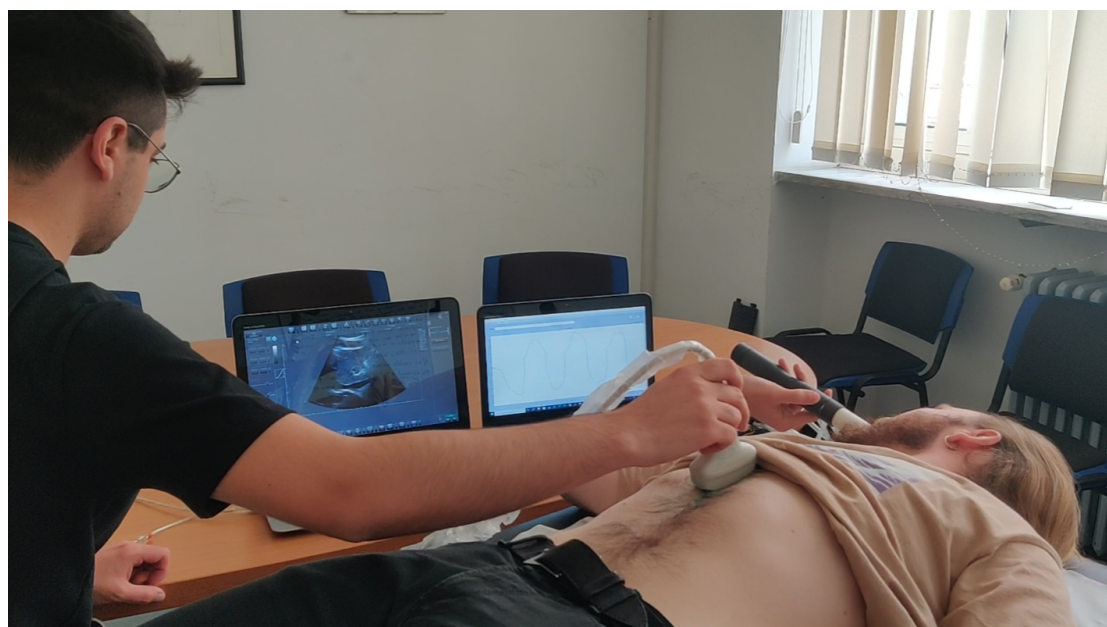
Figure 4.1: *Experimental setup*

In this study, 16 healthy subjects were analysed, however 6 persons were excluded due to the poor quality of the ultrasound videos. Consequently, the final dataset

consisted of 10 healthy subjects (1 female and 9 males, with 24.1 $\pm$ 0.5 years old). During the execution of the experimental protocol tests, the subject was placed supine on an ultrasound couch and performed specific respiratory manoeuvres while using the spirometer. In addition, the subject monitored the flow signal displayed on the PC screen in real time to ensure the correct execution of the respiratory manoeuvres.

At the same time, the inferior vena cava was scanned by ultrasound, with the ultrasound probe positioned just below the xiphoid process and its marker pointing towards the subject's head in order to scan the inferior vena cava in its longitudinal axis. The vein was not scanned in its transverse axis due to poor visibility. To ensure accurate acquisitions of the same portion of the IVC, the position of the probe was not changed between scans.

The protocol involved three tests lasting 10 seconds each, in order to record three respiratory cycles. In addition, before each test, the subject underwent a short training phase in order to perform the tests with greater precision.

In the first test, the subject is asked to breathe normally without exerting any effort. On the PC screen, the subject displays the respiratory flow signal, the scale of which is adapted based on the first respiratory cycle. Specifically, the value range of the vertical axis is set by increasing the recorded minimum and maximum flow values by 30%. At the end of the test, the minimum and maximum flow values in the inhalation and expiration phases respectively are calculated and averaged to obtain a reference flow value for each of the two phases.
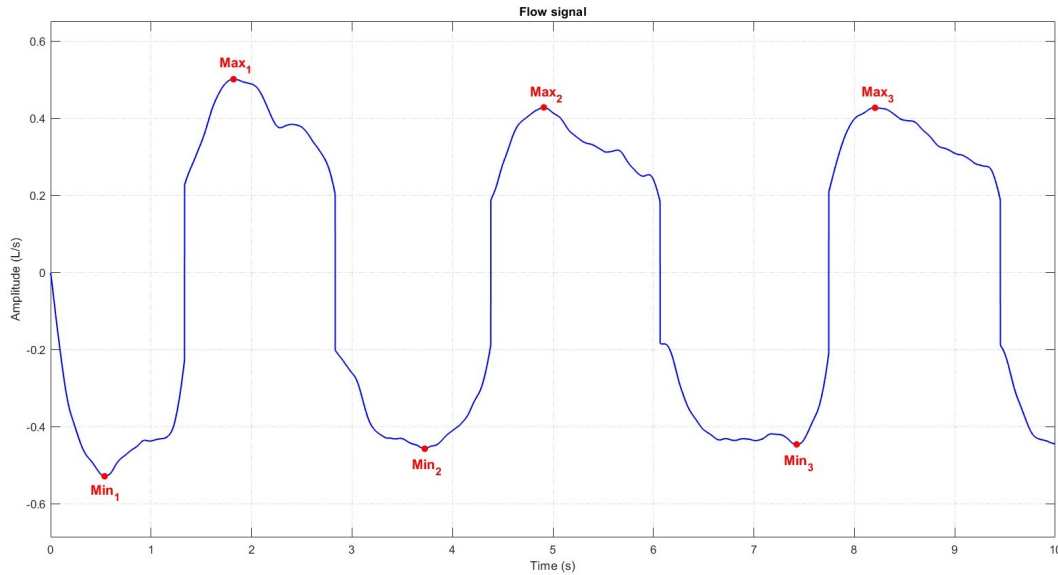
Figure 4.2: *Example of flow signal during normal breathing test. The red dots respectively identify the three maximum flow values (Max_1, Max_2, Max_3) and the three minimum flow values (Min_1, Min_2, Min_3), which are averaged to obtain the two reference values.*

The second and third trials of the protocol involve deep breathing and light breathing, respectively. During these trials, the subject observes the flow signal and two

bars, one upper and one lower, indicating the maximum and minimum values of respiratory flow that the subject must alternately achieve during breathing. In the case of deep breathing, the flow values indicated by the two bars correspond to the reference values calculated during the first trial of the experimental protocol, increased by 20%. For light breathing, on the other hand, the two values are reduced by 20%. In order to provide the subject with a margin of tolerance, a band was included around the flow value to be reached, having a width equal to 10% of this value. This allows the subject not to reach exactly the desired flow value, as long as the signal remains within the band.
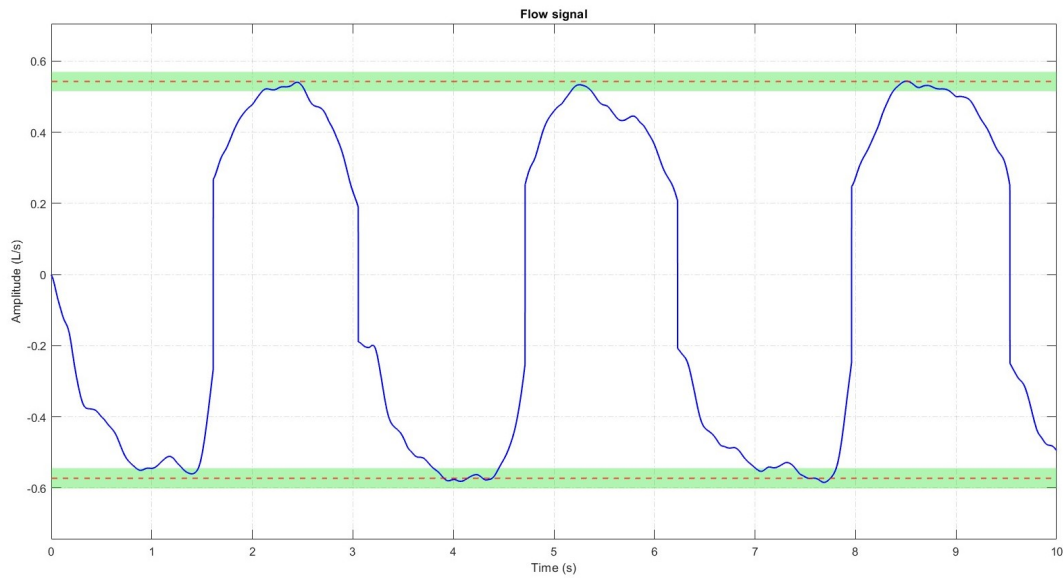
Figure 4.3: *Example of flow signal during the deep breathing test. The two dashed red lines represent the reference values obtained in the normal breath test increased by 20%, while the two green regions of amplitude 10% of the value they are centred on represent the margin of tolerance.*

Chapter 5

Data post-processing

During each test, the inferior vena cava was scanned along its longitudinal axis for the entire duration of the test. The purpose is to process the ultrasound video clips in order to obtain the time series of the inferior vena cava diameter and subsequently extract the vein pulsatility index or Caval Index.

5.1 IVC segmentation and temporal evolution of vein diameter

Viper software was used for the initial segmentation of the vein. The algorithm takes the ultrasound video clip as input and processes each frame, outputting the segmentation of the inferior vena cava, i.e. the upper and lower edges of the vein. After selecting the video clip to be processed, the operator must sequentially indicate certain information required for processing. Initially, the user manually selects two reference points that are used to follow and estimate the movements of the vein. Subsequently, the user selects one point on the upper and one on the lower edge of the vein that identify the initial part of the vein from which to start the analysis. And finally, the user draws a line on the right end of the vein corresponding to the end part of the vein to be segmented.
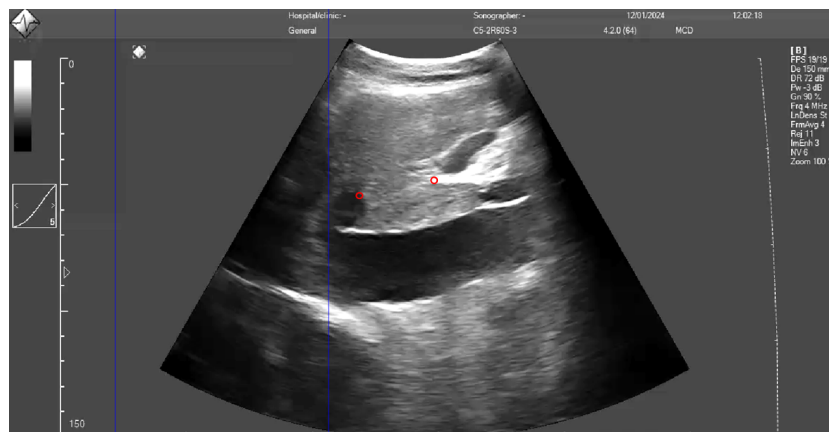
Figure 5.1: *Selection of the two reference points*
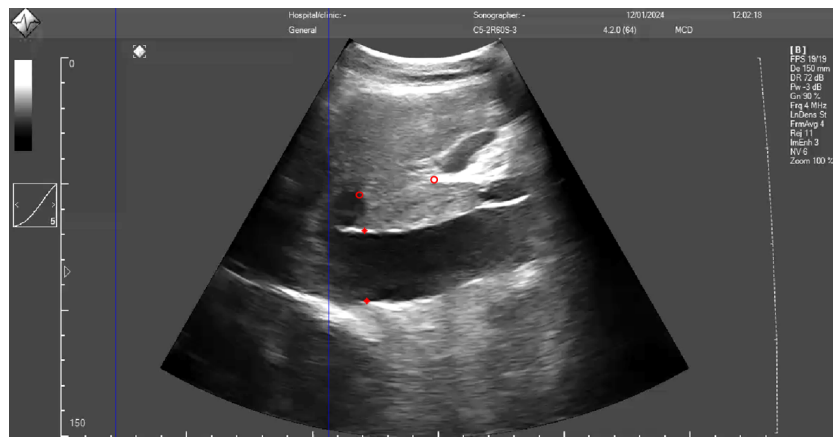
Figure 5.2: *Selection of one point on the upper and one on the lower edge of the vein*
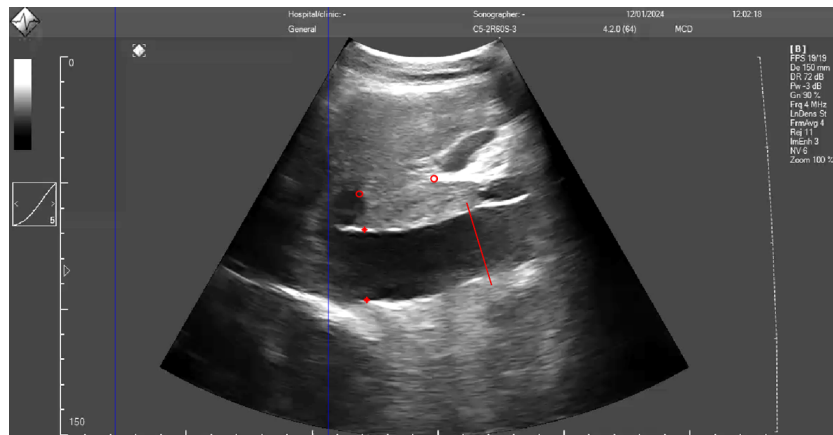
Figure 5.3: *Drawing the line on the right end of the vein*

Once the segmentation of the vein has been obtained, the time series of the vena cava diameter can be extracted.

Considering one frame at a time, from the upper and lower edges of the vein, the median line of the vein is determined by taking the upper and lower edges and averaging them. This line is then interpolated using a fourth-degree polynomial. At this point, the total length of the curve is calculated, focusing exclusively on the portion of the vein approximately between 10% and 90% of its length, thus neglecting the ends. On this new length, 20 points are uniformly distributed and, for each point, the line perpendicular to the curve and passing through the point considered is drawn; the intersections between this line and the two edges of the vein define the diameter of the vein. In this way, 20 diameter values are obtained, which are averaged to obtain a single diameter value representative of the frame. The diameter obtained is expressed in pixels and requires conversion to millimetres. A conversion coefficient can be extracted based on the scanning depth of the ultrasound video. By multiplying the diameter in pixels by this coefficient, the diameter value expressed in millimetres is obtained.

By performing this procedure for each frame of the ultrasound recording, the evolution of the diameter of the inferior vena cava over time is obtained.
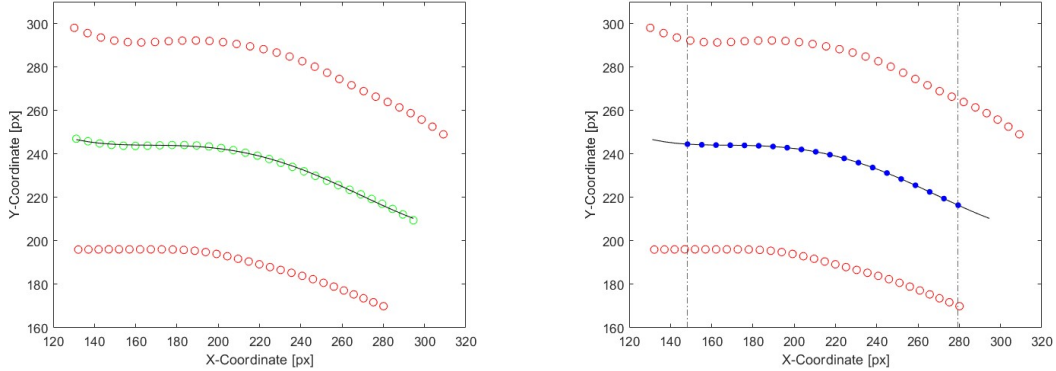
(a) Upper and lower edges of the vein sampled on 30 points (red points). Median line (green points) and its interpolation with a 4th degree polynomial (black line).

(b) Uniform distribution of 20 points (blue points) in the 10% to 90% portion of the vein length.
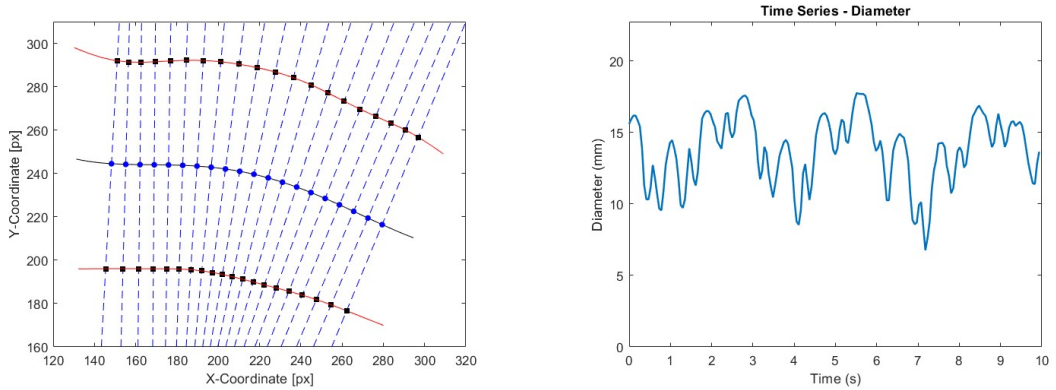
(c) For each of the 20 points, a line perpendicular to the median line and passing through the point is drawn (dashed blue lines), and its intersections with the two edges of the vein determine the diameter value

(d) Time series of the inferior vena cava diameter

Figure 5.4: *Procedure for obtaining the diameter time series*

5.2 IVC pulsatility index extraction

From the temporal evolution of the vein diameter it is possible to extract the pulsatility index or Caval Index. Specifically, changes in vein diameter result mainly from two distinct stimuli: respiration and cardiac activity. For each of these stimuli, an additional pulsatility index can be derived, called Respiratory Caval Index (RCI) and Cardiac Caval Index (CCI) respectively. These indices are derived by applying the formula 2.9 to the respiratory and cardiac components alone [16].

The two different components are extracted from the diameter time series using different filters. In order to identify the cut-off frequencies to be used for separating the respiratory and cardiac components, a power spectral density estimation was first carried out on both the diameter signal and the flow signal obtained with the spirometer.
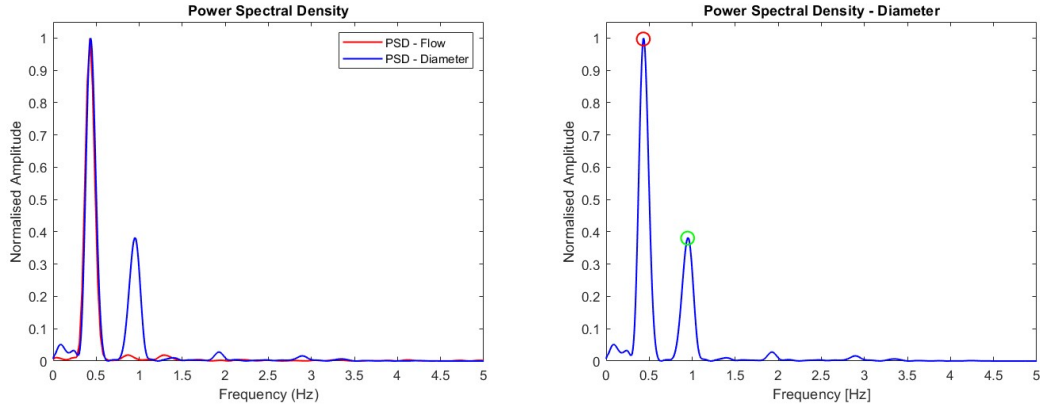
(a) PSD of the diameter signal (blue) and PSD of the flow signal (red)

(b) Manual selection of the respiratory frequency and cardiac frequency

Figure 5.5: *PSD of the signals for the extraction of the respiratory and cardiac component*

Looking at the PSD of the signals, it can be seen that both signals have a peak at the respiratory rate while only the diameter signal has an additional peak at the heart rate. The respiratory and heart rates are obtained by manually selecting the peaks on the graph, as shown in Fig. 5.5b.

After obtaining the two frequency values, the diameter signal is high-pass filtered with a Chebyshev I type filter with a cut-off frequency equal to the heart rate increased by 0.5 Hz [7]. Subsequently, the signal thus obtained is filtered again in order to extract the respiratory component and the cardiac component. For the former, the signal is low-pass-filtered with a 1st-order Chebyshev filter with a cut-off frequency equal to the respiratory rate increased by 0.2 Hz; for the latter, the signal is high-pass-filtered with a 1st-order Chebyshev filter with a cut-off frequency equal to the heart rate decreased by 0.2 Hz.

Each filter was used twice, once with the time axis reversed, in order to eliminate phase distortion and delay.

Finally, the diameter signal, respiratory component and cardiac component are divided according to respiratory cycles using the flow signal acquired via the spirometer, as shown in Fig. 5.8. For each respiratory cycle, the CI, RCI and CCI are calculated, which are then averaged across respiratory cycles to obtain an average of the CI, RCI and CCI values.
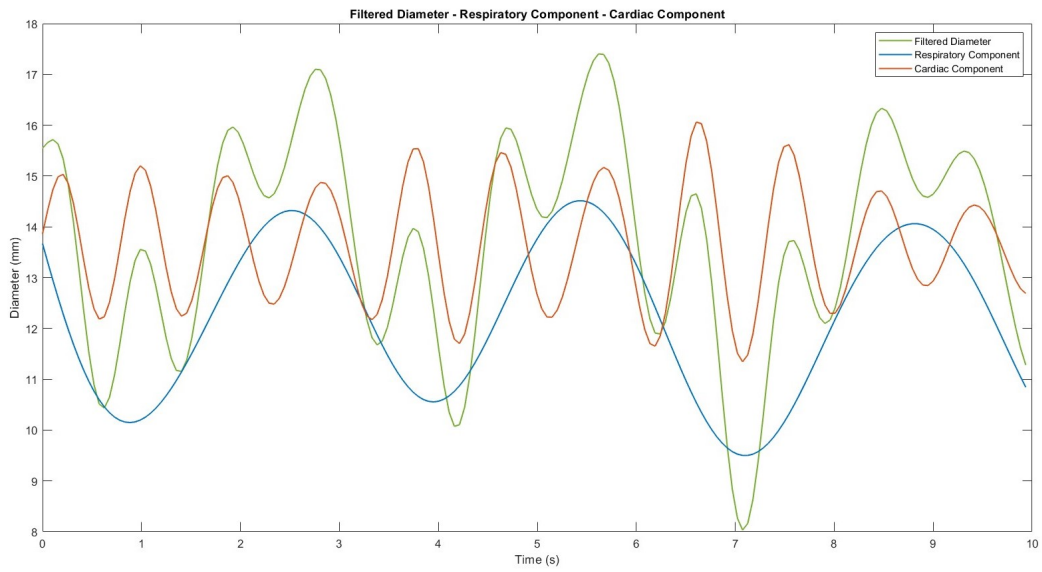
Figure 5.6: *Overlapping filtered diameter, respiratory component and cardiac component*
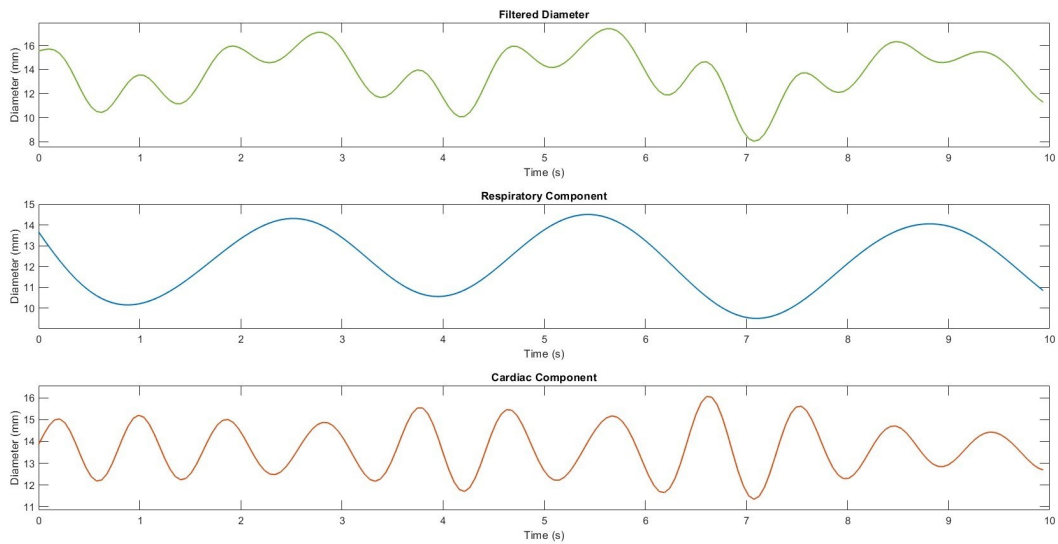
Figure 5.7: *Filtered diameter (top), respiratory component (middle) and cardiac component (bottom)*
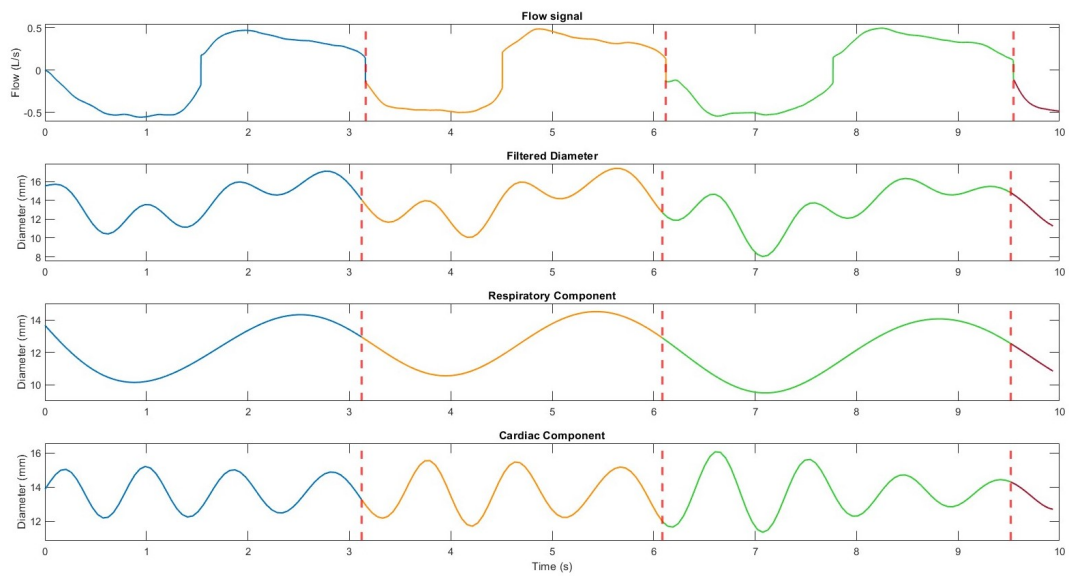
Figure 5.8: *Segmentation of signals according to respiratory cycles. The dotted red lines identify the end of each respiratory cycle.*

Chapter 6

Statistics

Statistics is a branch of mathematics that focuses on the collection, analysis and interpretation of data.

It can be divided into two parts: descriptive and inferential statistics. The former describes the characteristics of data by means of indices (mean, median, standard deviation, etc) and graphical representations (bar chart, scatter plot, box plot, etc). The latter, on the other hand, makes it possible to extract information on the population by means of sample data.

6.1 Descriptive statistics

Bar charts were used to analyse and compare the Caval Indices and inferior vena cava diameter results obtained under the three breathing conditions. Spearman's correlation was used to analyse the correlation between the dynamics of the vein and the pressure values measured by the differential pressure sensors connected to the spirometer.

6.1.1 Bar diagram

The 'bar diagram' is a graphical representation of data by means of rectangular bars, the height of which is proportional to the value they represent. In this type of diagram, two variables can be distinguished: a categorical variable and a numerical variable, which determines the length of the bar.

6.1.2 Coefficient of Variation

The coefficient of variation is a numerical index describing the relative variability of a data distribution. It can only be used for quantitative variables and is calculated as:

$$CoV = \frac{\sigma}{|\mu|} \tag{6.1}$$

where σ is the standard deviation and μ is the mean value of the data distribution The closer the CoV value is to zero, the lower the variability of the data distribution.

6.1.3   Spearman's correlation

The Spearman's correlation coefficient is used to quantify the intensity of the relationship between two variables and it is used when the conditions for applying the Pearson's correlation are not met, i.e. when the distribution of the two variables is not normal.

Spearman's correlation, unlike Pearson's correlation, measures the intensity of the relationship between the ranks of the two variables, so it is also less sensitive to outliers. Specifically, the values of the two variables are first converted into ranks and then the correlation coefficient is calculated.

The Spearman's correlation coefficient is calculated as:

$$\rho = 1 - \frac{6\sum_{i=1}^{n} d_i^2}{n(n^2 - 1)} \tag{6.2}$$

where n is the number of observations and d_i is square of the difference between the rank of the first variable and the rank of the second variable relative to the ith observation.

The Spearman's correlation coefficient can take values between -1 and +1. The stronger the relationship between the variables, the closer the correlation coefficient is to +1 or -1.

6.2   Inferential statistics

In inferential statistics there are two types of tests: parametric and non-parametric tests. Parametric tests are used when the data follow a normal distribution, have the same variance and are randomly drawn from the population. Non-parametric tests, on the other hand, do not assume a specific distribution of the data. In general, they are used for small sample sizes, for data that do not follow a normal distribution, and are not as sensitive to outliers as parametric tests.

Since the sample size in this work is small, non-parametric tests such as 'Friedman's test' and 'Wilcoxon signed rank test' are chosen to perform a statistical analysis.

6.2.1   Hypothesis test and p-value

A hypothesis test is a procedure for testing a population hypothesis from sample data.

In a hypothesis test there are two different hypothesis: the null hypothesis (H_0), which is formulated with the aim of rejecting it, and the alternative hypothesis (H_1), which is opposed to H_0. When the null hypothesis is rejected but should be accepted, or when it is accepted but should be rejected, an error is committed. Specifically, in the first case the type I error is committed and the probability of committing this error is known as significance level α, whereas in the second case the type II error is committed and the probability of committing this error is identified as β. Furthermore, the probability of accepting the null hypothesis when it is true is called specificity, while the probability of rejecting the null hypothesis

when it is false is called sensitivity.

The significance level α is chosen following the formulation of the hypothesis, and it is generally set at 0.05.

To determine whether differences between samples are statistically significant or due to chance, a value known as 'p-value' is used, which is compared to the significance level. If the p-value is lower than α, then the null hypothesis H_0 can be rejected.

6.2.2 Friedman test

The 'Friedman test' is a non-parametric method used to compare more than two related samples, and it is the equivalent non-parametric test of the repeated measures analysis of variance (ANOVA).

To perform the Friedman test, the values of each subject are first ranked for each analysed condition. Subsequently, the F_r statistic test can be calculated as:

$$F_r = \left[\frac{12}{nk\,(k+1)} \sum_{i=1}^{k} R_i{}^2 \right] - 3n\,(k+1) \tag{6.3}$$

where n is the number of subjects, k is the number of conditions, and R_i is the sum of the ranks of the ith condition.

If there are equal values between the different conditions for the same subject, the statistical test F_r can be determined as:

$$F_r = \frac{n\,(k-1)\left[\sum_{i=1}^{k} \frac{R_i{}^2}{n} - C_F \right]}{\sum r_{ij}{}^2 - C_F} \tag{6.4}$$

where n is the number of subjects, k is the number of conditions, R_i is the sum of the ranks of the ith condition, C_F is a correction factor equal to $\frac{1}{4}nk\,(k+1)^2$, and R_{ij} is the rank corresponding to subject j in column i.

The degrees of freedom, denoted as df, are derived as:

$$df = k - 1 \tag{6.5}$$

where k is the number of conditions.

Once the value of the statistical test F_r has been obtained, it must be compared with the table of critical values to determine whether there is a statistical difference between the groups. If the number of groups k or the number of subjects n exceeds those available in the table, an approximation for large samples can be made using the table with the χ^2 distribution.

If the F_r statistic is significant then there is a difference between at least two of the conditions [17]. In this case, a post-hoc test must be performed to determine which pairs of conditions are significantly different. For example, the Bonferroni correction can be used, in which a Wilcoxon signed rank test and a corrected α value are used. The new significance level is obtained as:

$$\alpha_B = \frac{\alpha}{k} \tag{6.6}$$

where α_B is the corrected significance level, α is the original significance level and k is the number of comparisons.

6.2.3   Wilcoxon signed rank test

The 'Wilcoxon signed rank test' is a non-parametric method used to compare two related samples, and it is the non-parametric equivalent of the 'Student's t-test'. The formula for calculating the Wilcoxon T-test is:

$$T = smaller\ of\ \sum R_+ \ and\ \sum R_- \tag{6.7}$$

where $\sum R_+$ and $\sum R_-$ are the sum of the ranks with positive and negative differences, respectively.

After obtaining the T statistic, it must be compared with the table of critical values. If the number of pairs n exceeds those available in the table, an approximation can be made for large samples. In this case, a z-score is calculated and a table with the normal distribution is used to obtain a critical region of z-scores. The z-score is obtained by means of the following formulae:

$$\overline{x}_T = \frac{n\,(n+1)}{4} \tag{6.8}$$

where $\overline{x}_T$ is the mean and n is the number of matched pairs analysed,

$$s_T = \sqrt{\frac{n\,(n+1)\,(2n+1)}{24}} \tag{6.9}$$

where s_T is the standard deviation,

$$z^* = \frac{T - \overline{x}_T}{s_T} \tag{6.10}$$

where z^* is the z-score for an approximation of the data to the normal distribution and T is the T statistic [17]

Chapter 7

Results and Discussion

This chapter presents the results of this pilot study, which aims to analyse the dynamics of the inferior vena cava under different controlled breathing conditions. In particular, the results relating to Caval Indices, inferior vena cava diameter and correlations between vein dynamics and pressure values measured by differential pressure sensors connected to the spirometer are illustrated, accompanied by the relevant discussions.

7.1 IVC pulsatility

7.1.1 Caval Indices

The bar graphs in Figs. 7.1 and 7.2 show the trends of the three Caval Indices, represented by mean and error bar, in the three breathing conditions tested. Tab. 9.1 shows the values of the three Caval Indices, expressed in terms of mean and standard deviation.

Analysing the trends of the three parameters in the different breathing modes, it is observed that both CI and RCI show a progressive increase in their value from the light to the deep breathing condition, while the CCI remains relatively stable in the three conditions analysed. Specifically, CI is more influenced by RCI, indicating that IVC pulsatility is mainly due to respiratory rather than cardiac activity. This phenomenon is most evident in normal and deep breathing conditions. The RCI, on the other hand, reflects the breathing-related stimulus, increasing in proportion to the intensity of breathing. Consequently, the RCI increases from the light breathing condition to the deep breathing condition as the effort exerted by the subject increases. As far as the CCI is concerned, there is a slight increase in its value, which is more evident between the light and normal breathing conditions, but it tends to remain relatively stable between the different conditions compared to the other two parameters. This behaviour can be explained by the fact that the CCI reflects the pulsatility of the IVC due to cardiac activity, which remains essentially constant.

Importantly, both CI and RCI increase more between the light and normal breathing modes, rather than between the normal and deep breathing modes. This can be attributed to the fact that the analysis was conducted on healthy subjects, in

whom the normal breathing condition can already cause maximum IVC collapse, without there being a significant difference with the deep breathing condition. For example, for one subject analysed, the CI and RCI reached 70% and 55% in both the normal and deep breathing conditions, respectively.

This effect is also evident from the statistical analysis of the three parameters, which highlighted the differences between the three breathing conditions. Friedman's test revealed a statistically significant difference for CI and RCI. The Wilcoxon signed-rank test with Bonferroni correction for the post-hoc tests showed for the CI a statistically significant difference with $p < 0.01$ between the light and normal breathing conditions and between the light and deep breathing conditions, and a significant difference with $p < 0.05$ between the normal and deep breathing conditions. For the RCI, the Wilcoxon signed-rank test with Bonferroni correction showed a statistically significant difference with $p < 0.01$ between the light and normal breathing conditions and between the light and deep breathing conditions. Consequently, the light and deep breathing conditions, particularly light breathing, are able to result in significant differences from the normal breathing condition in terms of IVC pulsatility.

In conclusion, the three tests tested in the experimental protocol succeed in inducing a different pulsatility of the vein, while not requiring excessive effort by the subjects analysed.
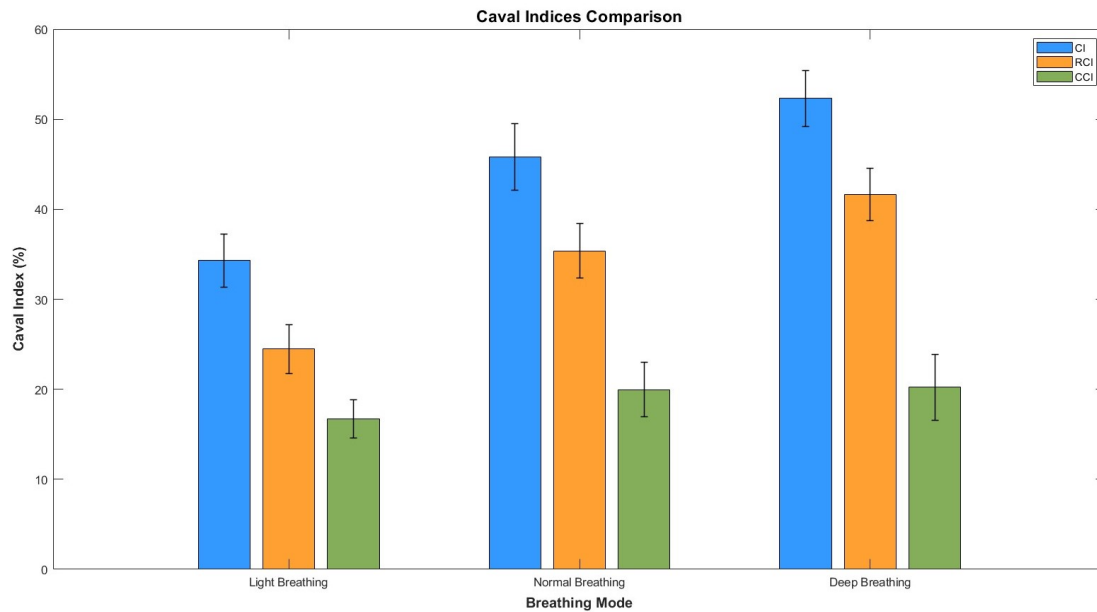

Figure 7.1: *Bar chart showing mean values and error bars of the Caval Indices for each breathing mode, grouped according to breathing mode.*
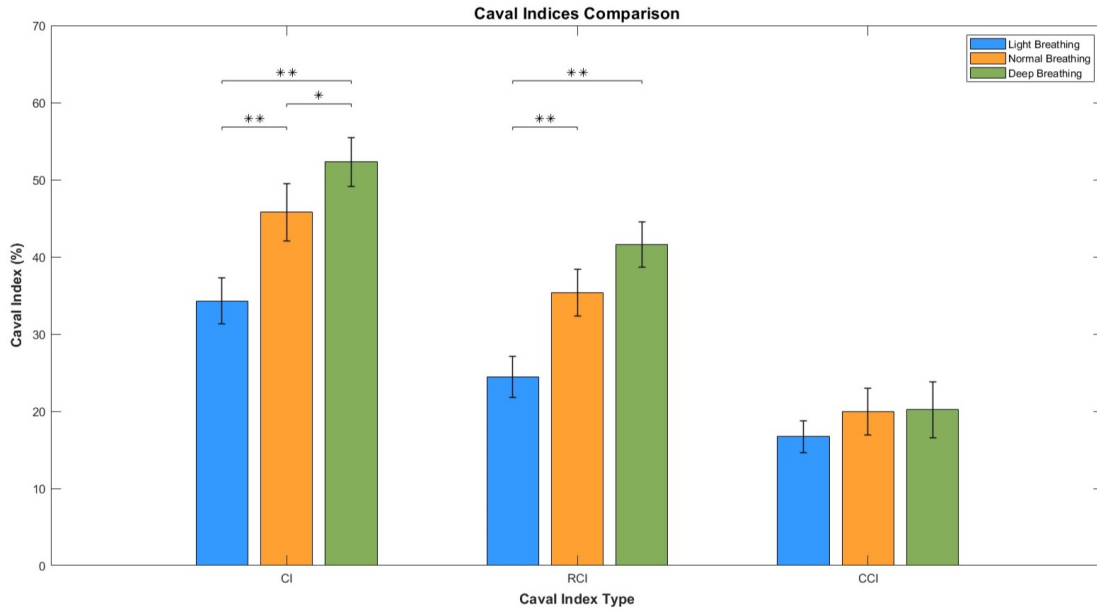
Figure 7.2: *Bar chart showing the mean values and error bars of the Caval Indices for each breathing mode, grouped according to the type of Caval Index. Square brackets indicate statistically significant differences (* p<0.05, ** p<0.01).*

Breathing Mode	Caval Index		
	CI (%)	RCI (%)	CCI (%)
Light Breathing	34.30 ± 9.36	24.46 ± 8.49	16.71 ± 6.62
Normal Breathing	45.79 ± 11.72	35.36 ± 9.62	19.97 ± 9.62
Deep Breathing	52.30 ± 9.89	41.00 ± 9.23	20.21 ± 11.45

Table 7.1: *Percentage values of the Caval Indices, expressed as mean and standard deviation, for each breathing mode.*

7.1.2   Coefficient of Variation of Caval Indices

The bar charts presented in Figs. 7.3 and 7.4 highlight the Coefficients of Variation of the three Caval Indices, represented by mean and error bar, in the three breathing conditions tested. Tab. 7.2 provides the values of the coefficients of variation of the Caval Indices, expressed in terms of mean and standard deviation.

The results obtained are slightly out of line with expectations. In the light and deep breathing conditions, the subject has to reach predetermined flow values, in contrast to the normal breathing condition, in which no indication of the breathing mode is given. Consequently, one would expect to observe lower Coefficients of Variation for CI and RCI in these two conditions than in the normal breathing

condition, and very similar Coefficients of Variation for CCI between the three conditions, as the latter is related to cardiac activity. However, when looking at the CoV values for CI and RCI, which depend mainly on breathing activity, this effect is not evident.

Specifically, it is observed that for the CI, CoV values decrease from the light breathing condition to the deep breathing condition, while for the RCI, the minimum CoV value occurs in the normal breathing condition. In contrast, the coefficient of variation of the CCI is very similar in the light and normal breathing conditions, but increases significantly in the deep breathing condition, suggesting greater variability of the CoV in the latter condition.

Part of these problems could result from the quality of the ultrasound videos, as the vein moves during breathing, and different longitudinal sections of the vein could be scanned. In addition, during the deep-breathing condition, sometimes the peak relative to the heart rate, which was used to extract the cardiac component of the pulsatility of the IVC from which to obtain the CCI, was not easily visible in the power spectral density plot, as pulsatility in this condition is dominated mainly by respiration. This can lead to a cardiac component of the Caval Index that does not accurately reflect the pulsatility of the IVC related to cardiac activity. To obtain a more accurate estimate of the CCI and consequently a lower coefficient of variation, one solution might be to implement a sensor to monitor cardiac activity, such as a heart rate monitor.
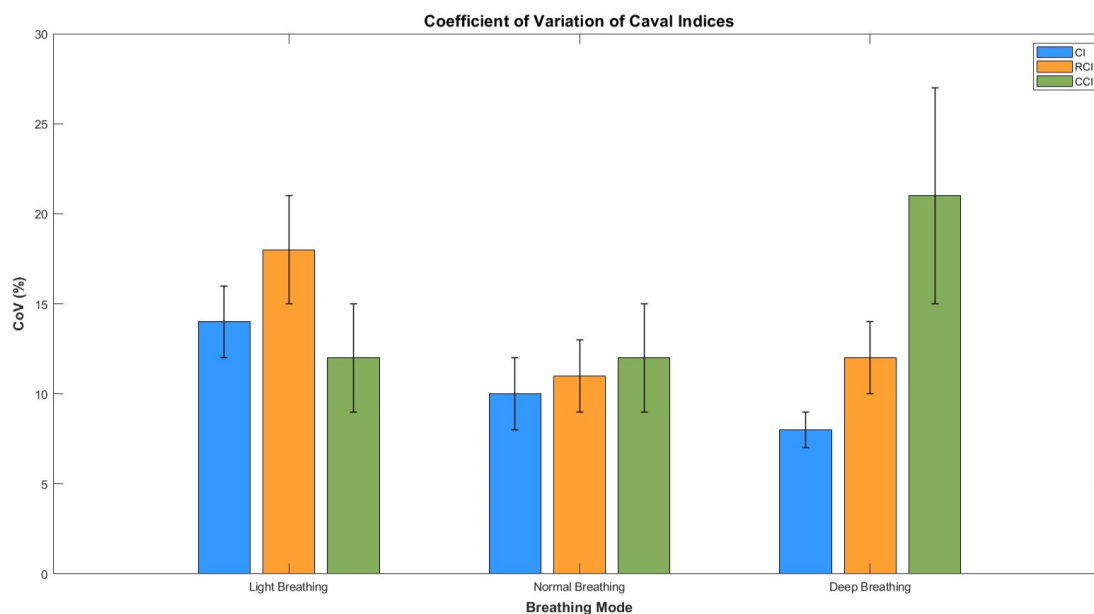

Figure 7.3: *Bar chart showing mean values and error bars of the Coefficient of Variation of the Caval Indices for each breathing mode, grouped according to breathing mode.*
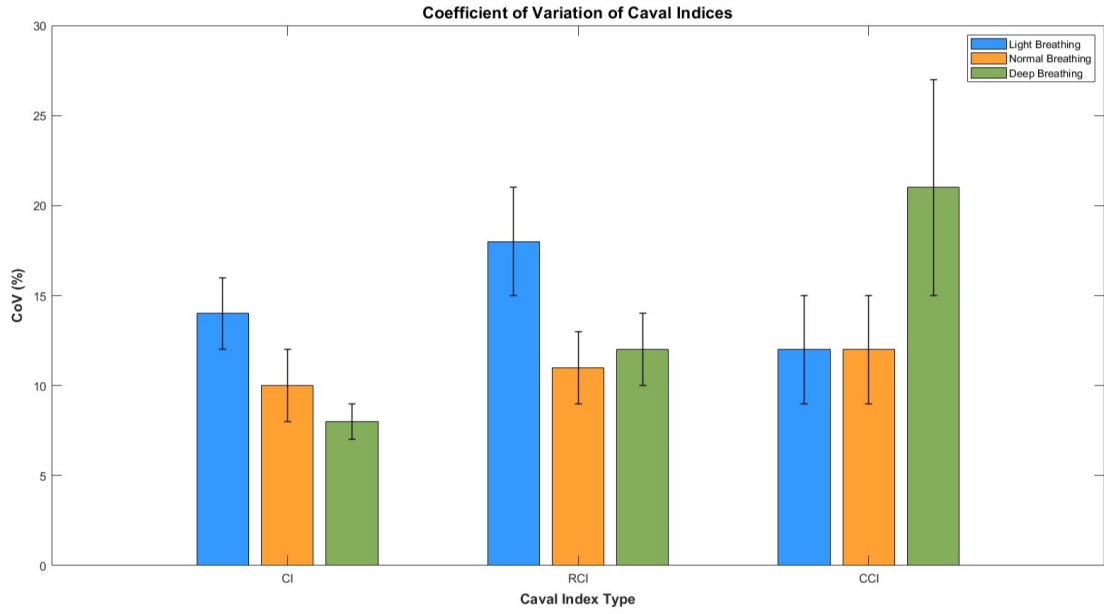
Figure 7.4: *Bar chart showing the mean values and error bars of the Coefficient of Variation of the Caval Indices for each breathing mode, grouped according to the type of Caval Index.*

Breathing Mode	Coefficient of Variation		
	CI (%)	RCI (%)	CCI (%)
Light Breathing	14.50 ± 6.92	17.55 ± 9.86	11.91 ± 8.27
Normal Breathing	9.85 ± 5.35	10.93 ± 7.71	12.00 ± 9.18
Deep Breathing	8.31 ± 3.67	11.85 ± 6.61	21.31 ± 19.46

Table 7.2: *Percentage values of the Coefficient of Variation of the Caval Indices, expressed as mean and standard deviation, for each breathing mode.*

7.2 IVC size

7.2.1 Minimum diameter

Fig. 7.5 shows the mean value and error bar of the minimum diameter of the IVC in the three breathing conditions tested, together with the linear regression model to show the trend.

The minimum diameter values obtained for the light, normal and deep breathing conditions, expressed as mean and standard deviation, are 10.58 ± 3.48 mm, 8.79 ± 3.71 mm and 7.62 ± 2.57 mm, respectively. There is a gradual decrease in the minimum diameter, obtained during the inhalation phases of the respiratory cycles, moving from the light to the deep breathing condition. This indicates that as
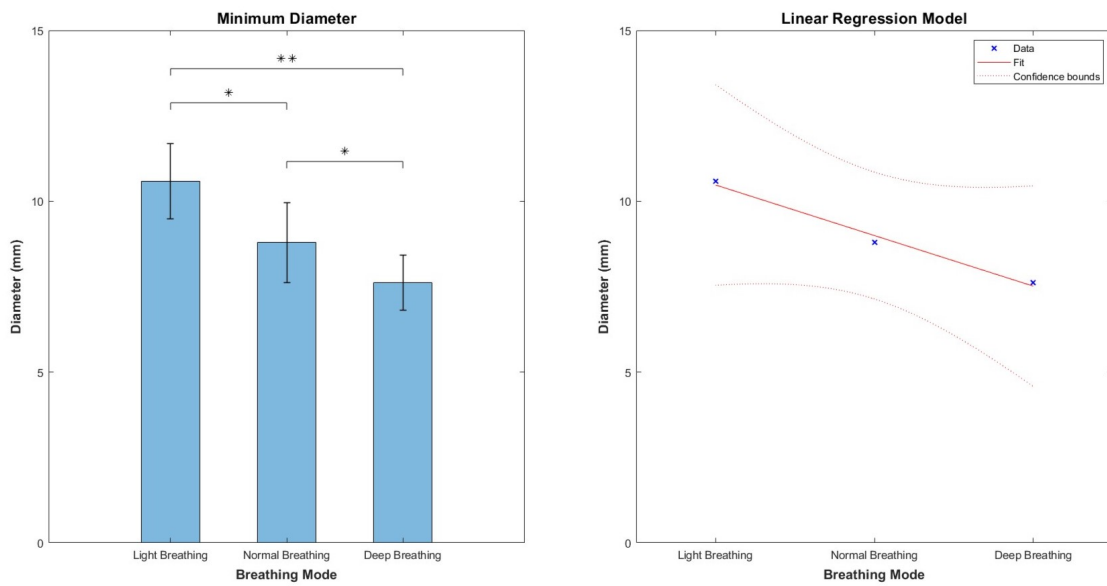
Figure 7.5: *On the left is a bar chart showing the mean value and error bar of the minimum diameter of the IVC in the three breathing conditions. Square brackets indicate statistically significant differences (* p<0.05, ** p<0.01). On the right is the linear regression model to show the decreasing trend.*

respiratory effort increases, the IVC becomes more compressed, in line with theory. There is also a greater reduction in diameter between the light and normal breathing conditions, in agreement with what was previously discussed regarding Caval Indices.

A linear regression model was created to show the downward trend, with a coefficient of determination of 0.97, indicating the good fit of the model. However, it is important to consider that the validity of the model could be affected by the limited number of conditions analysed. An analysis on a larger number of conditions could confirm this trend.

From a statistical point of view, the Friedman test yielded significant results. The Wilcoxon signed-rank test with Bonferroni correction for post-hoc tests showed a statistically significant difference with $p < 0.01$ between the light and deep breathing conditions, and with $p < 0.05$ between the light and normal breathing conditions, as well as between the normal and deep breathing conditions.

7.2.2 Maximum diameter

Fig. 7.6 shows the mean value and error bar of the maximum diameter of the IVC in the three breathing conditions tested, together with the linear regression model to show the trend.

The maximum diameter values obtained for the light, normal and deep breathing conditions, expressed as mean and standard deviation, are 16.88 ± 3.83 mm, 16.61 ± 3.97 mm and 16.66 ± 2.95 mm, respectively. It is observed that the maximum diameter, measured during the exhalation phases of the respiratory cycles, remains
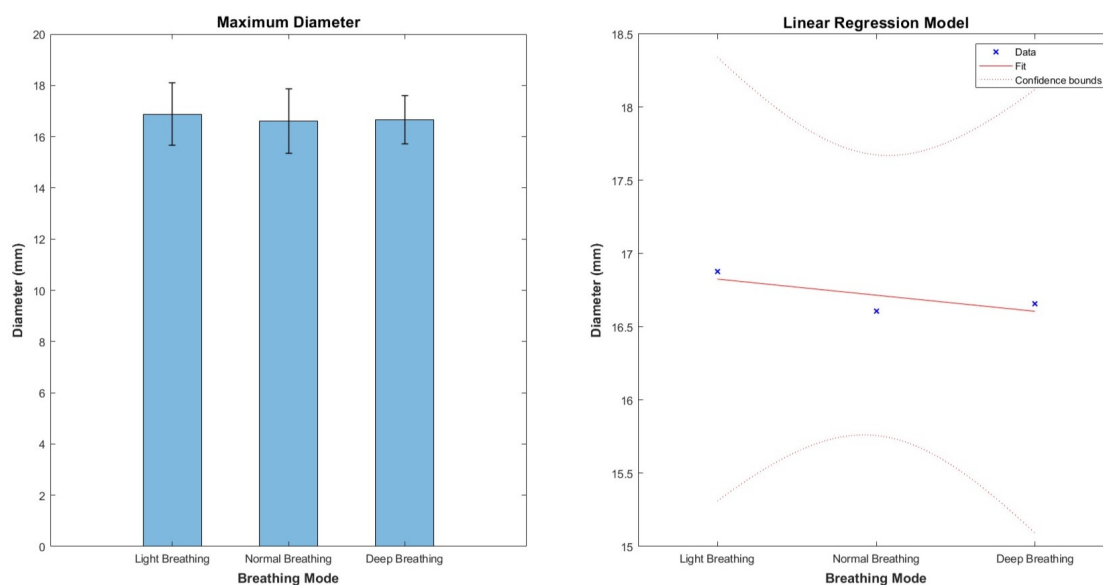
Figure 7.6: *On the left is a bar chart showing the mean value and error bar of the maximum diameter of the IVC in the three breathing conditions. On the right is the linear regression model to show the trend.*

essentially constant, with no evidence of a significant dependence on the subject's respiratory effort.

In this case, the linear regression model has a coefficient of determination of 0.17, indicating a poor fit of the model.

From a statistical point of view, the Friedman test did not lead to a statistically significant difference, as one might have expected from the results mentioned above.

From the results of the trends in the minimum and maximum diameter of the inferior vena cava in the three breathing conditions, it can be deduced that the increase in pulsatility of the IVC, as indicated by the Caval Indices described above, is mainly due to the reduction in the diameter of the vein, i.e. its collapse. The three breathing conditions involve a different level of effort exerted by the subject: the greater the effort, the lower the intrathoracic pressure and the more the vein is compressed.

7.2.3 Mean diameter

Fig. 7.7 shows the mean value and error bar of the mean diameter of the IVC in the three breathing conditions tested, together with the linear regression model to show the trend.

The mean diameter values obtained for the light, normal and deep breathing conditions, expressed in terms of mean value and standard deviation, are 13.90 $\pm$ 3.83 mm, 12.98 $\pm$ 4.36 mm, 12.21 $\pm$ 3.16 mm, respectively. A gradual decrease in mean diameter can be seen moving from the light breathing condition to the
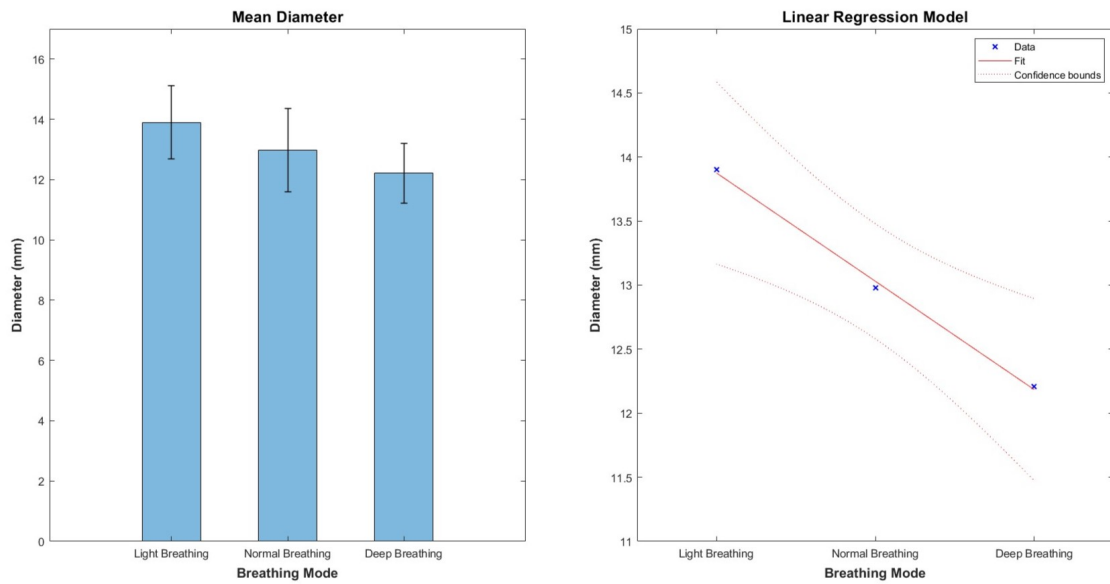
Figure 7.7: *On the left is a bar chart showing the mean value and error bar of the mean diameter of the IVC in the three breathing conditions. On the right is the linear regression model to show the decreasing trend.*

deep breathing condition, in line with what could be expected from the trends in minimum and maximum diameter.

A linear regression model was constructed to show the downward trend, showing a coefficient of determination of 0.99, indicating the good fit of the model.

From a statistical point of view, the Friedman test did not lead to a statistically significant difference.

7.3 Correlations between pressure values and IVC variables

From the previous results on pulsatility indices and IVC size, it can be concluded that the variables that vary the most as a function of the subject's exertion are mainly CI, RCI, minimum diameter and mean diameter of the IVC.

As the three breathing conditions tested involve different levels of subject's effort, leading to variations in the previously mentioned variables, the differential pressure values measured by the sensors connected to the spirometer are also different. Therefore, the aim is to look for a relationship between the pressure values and the variables related to IVC.

With regard to the minimum diameter, it decreases as the effort exerted by the subject increases. The increase in effort implies an increase in absolute differential pressure (or an increase in its negativity, since differential pressure values are negative due to the configuration of the spirometer) detected during the inspiration phase by the sensor that measures the pressure difference between the constriction and the spirometer outlet. For simplicity, this pressure difference in absolute value

will be called inspiratory pressure and referred to as P_{insp}.

Regarding the remaining variables, these are analysed in order to find a relationship with the respiratory pressure range, referred to as ΔP. This range is calculated as the sum of the absolute value of the pressure difference measured by one sensor during the inspiration phase (inspiratory pressure) and the absolute value of the pressure difference measured by the other sensor during the expiration phase (expiratory pressure). However, it is clear from previous results that the maximum diameter of the IVC remains almost constant, showing no dependence on expiratory pressure. Therefore, a relationship between inspiratory pressure alone and CI, RCI, and mean IVC diameter was also sought.
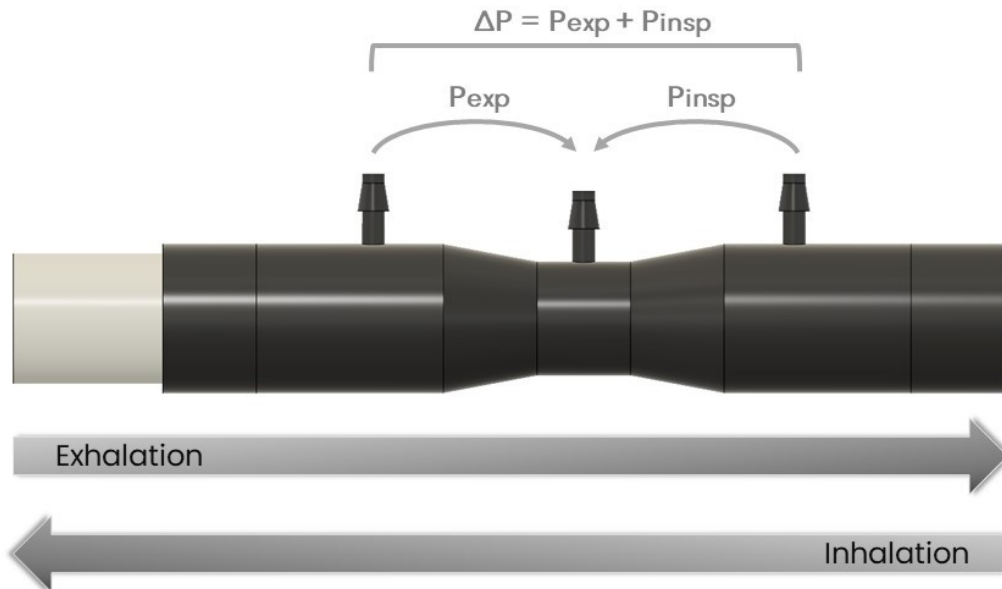

Figure 7.8: *Representation of the spirometer with an indication of respiratory pressures*

The Spearman's correlation coefficient was used to quantify the relationship between the variables, given the non-normal distribution of the pressure variables. The results are shown in Tab. 7.3.

The results show that all correlations are weak or, at most, moderate. The correlation coefficients for the minimum and mean diameter of the IVC are negative, as these variables tend to decrease as the subject's exertion increases. The correlation coefficients of the two pulsatility indices are positive, indicating that these variables tend to increase with increasing exertion. Finally, for all correlations, the p-values are above the significance level of 0.05, with the exception of the correlation between inspiratory pressure and CI, which is statistically significant.

	Spearman's Correlation	
	ρ	p
D_{min} - P_{insp}	-0.32	0.081
D_{mean} - ΔP	-0.21	0.27
D_{mean} - P_{insp}	-0.26	0.16
CI - ΔP	0.33	0.078
CI - P_{insp}	0.37	0.046
RCI - ΔP	0.31	0.092
RCI - P_{insp}	0.35	0.06

D_{min}: minimum diameter of IVC; D_{mean}: mean diameter of IVC.

Table 7.3: *Spearman's correlation coefficient*

Chapter 8

Conclusion

This thesis work led to the realisation of a spirometer, solving the problems associated with the model developed in a previous thesis project. This tool provides visual feedback, guiding the subject in the execution of breathing manoeuvres, and could help standardise the measurement of RAP.

The developed user interface allows for easy storage of the analysed subject's data, facilitates the operator in the data acquisition phases and allows for real-time verification of whether the subject is correctly performing respiratory manoeuvres.

Finally, the experimental protocol tested in this project consists of tests that do not require excessive effort compared to normal breathing, but still manage to induce a different pulsatility of the IVC. The protocol was tested on healthy subjects, in whom it is possible to observe a variation of Caval Indices in the three different tests, a variation that should be less evident in patients with high RAP.

However, this study has some limitations. Volunteers were not selected for echogenicity, so ultrasound scans could not be acquired on some subjects, while others were discarded during the data processing phase.

The results obtained are influenced by the quality of the ultrasound recordings, as the images obtained with a portable ultrasound machine are of lower quality than those obtained with a hospital ultrasound machine and depend largely on the experience of the operator. Furthermore, the results are influenced by the subject's breathing type, which can be thoracic or diaphragmatic. Diaphragmatic breathing, in fact, tends to compress the IVC more, leading to higher pulsatility indices.

The absence of a sensor capable of monitoring cardiac activity negatively impacts the extraction of the cardiac pulsatility index. This limitation can be overcome by implementing a heart rate monitor, for example.

Finally, the test execution times turned out to be rather long, especially in the light and deep breathing tests, in which the subject had to reach predetermined values of respiratory flow, requiring greater precision in the execution of the breathing manoeuvres.

Future work could include an analysis on a larger number of subjects and adopt solutions to overcome the problems found in this study.

Chapter 9

Future developments

Talking to some colleagues dealing with this issue, the idea emerged of assessing the pulsatility of the IVC under conditions in which the subject breathes in the same way in terms of respiratory flow and respiratory rate but against increasing resistance. As resistance increases, the positive and negative changes at the alveolar level increase, and consequently the intra- and extra-vascular effect on the IVC increases, which should increase its pulsatility.

For this purpose, two screens with circular holes were created which, by rotating relative to each other, allow the occlusion of the airflow passage area to be adjusted. The pair of screens is positioned at each end of the spirometer.

Using this system, three configurations are available:

- 1st configuration: perfectly overlapping screens

- 2nd configuration: the 4 central holes closed

- 3rd configuration: all holes partially occluded
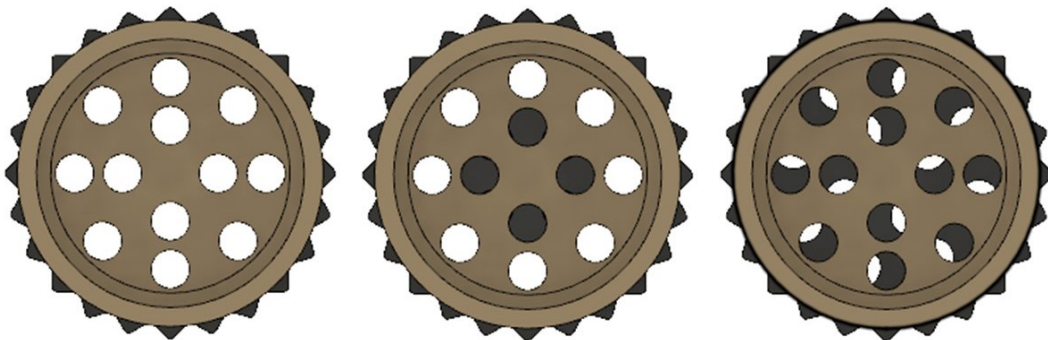
Figure 9.1: *Configurations of the two screens: perfectly overlapping screens (left), the 4 central holes closed (middle), all holes partially occluded (right)*

The experimental protocol involves three tests. In the first test, the subject is asked to breathe normally with the screens perfectly overlapping. From the flow signal, a waveform is extracted that reflects both the extent of breathing and the

respiratory rate. In the next two tests, one of the screen is rotated relative to the other and the subject is asked to breathe following the previously extracted waveform.
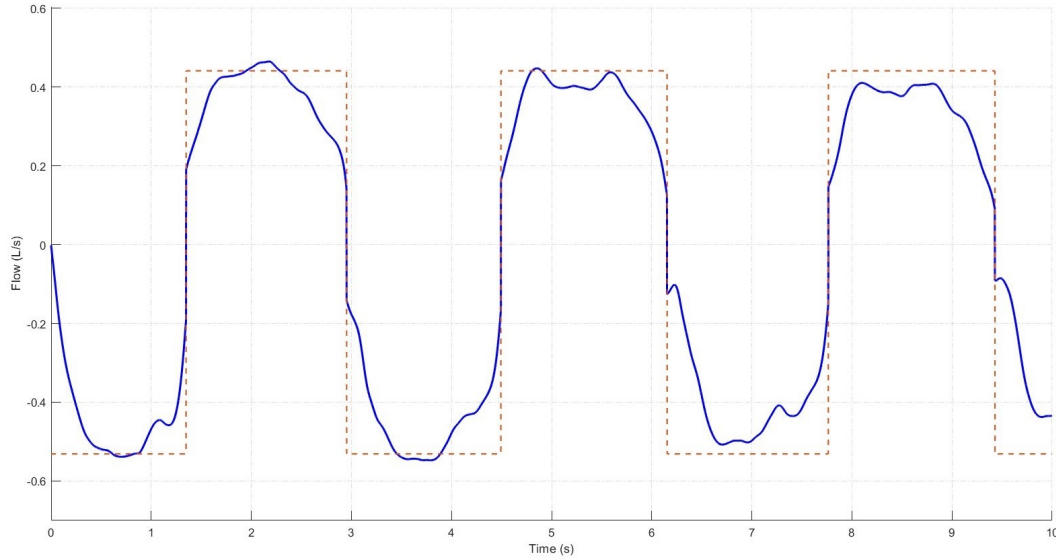

Figure 9.2: *Example of flow signal (blue) and extracted waveform (red)*

By testing this new system on a healthy subject, the following results were obtained:

Screen Configuration	Caval Index		
	CI (%)	RCI (%)	CCI (%)
1st configuration	18.46 ± 3.40	10.42 ± 1.17	9.60 ± 0.61
2nd configuration	28.66 ± 2.64	22.51 ± 4.72	12.67 ± 0.89
3rd configuration	31.03 ± 4.79	24.22 ± 7.00	10.82 ± 1.04

Table 9.1: *Percentage values of the Caval Indices, expressed as mean and standard deviation, for each screen configuration.*

Analysing the results, an increase in the pulsatility indices can be seen, although between the second and third conditions the increase is not as pronounced as between the first and second conditions.

Screen Configuration	Minimum, Maximum and Mean Diameter		
	Dmin (mm)	Dmax (mm)	Dmean (mm)
1st configuration	15.29	20.97	18.94
2nd configuration	14.07	21.57	16.98
3rd configuration	12.94	21.40	18.12

Table 9.2: *Values of the minimum, maximum and mean diameter of IVC for each screen configuration.*

Furthermore, it can be deduced that the increase in pulsatility of the IVC is mainly due to the reduction in the diameter of the vein, i.e. its collapse.
Of course, this system should be tested on a larger number of subjects in order to ensure its validity.

Appendix A

Caval Indices graphs
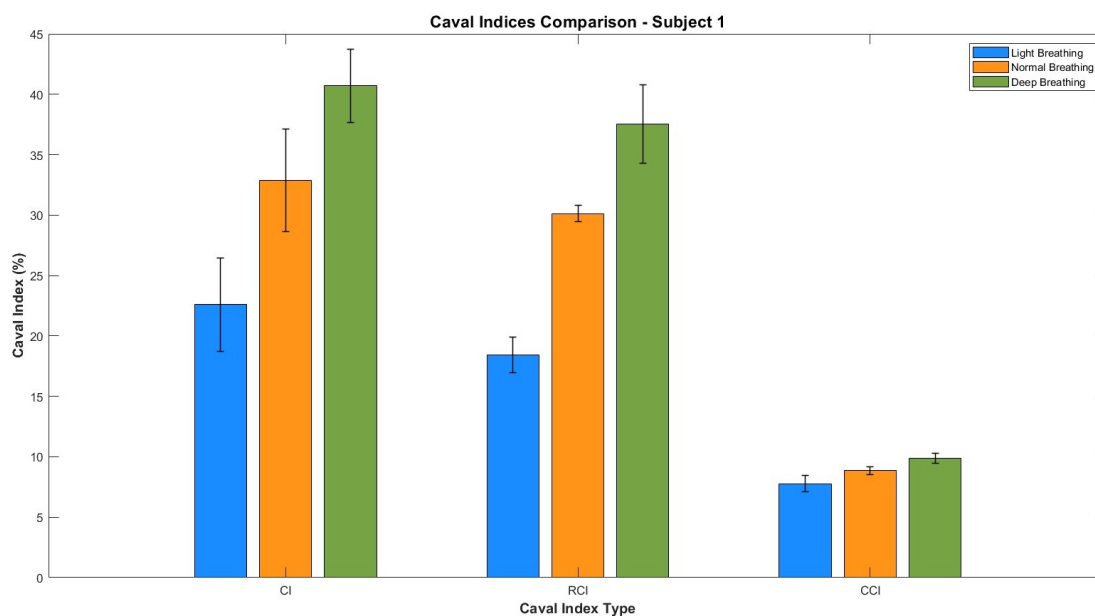
Figure A.1: *Bar chart showing mean values and standard deviations of the Caval Indices for each breathing mode, grouped according to the type of Caval Index, for subject 1.*
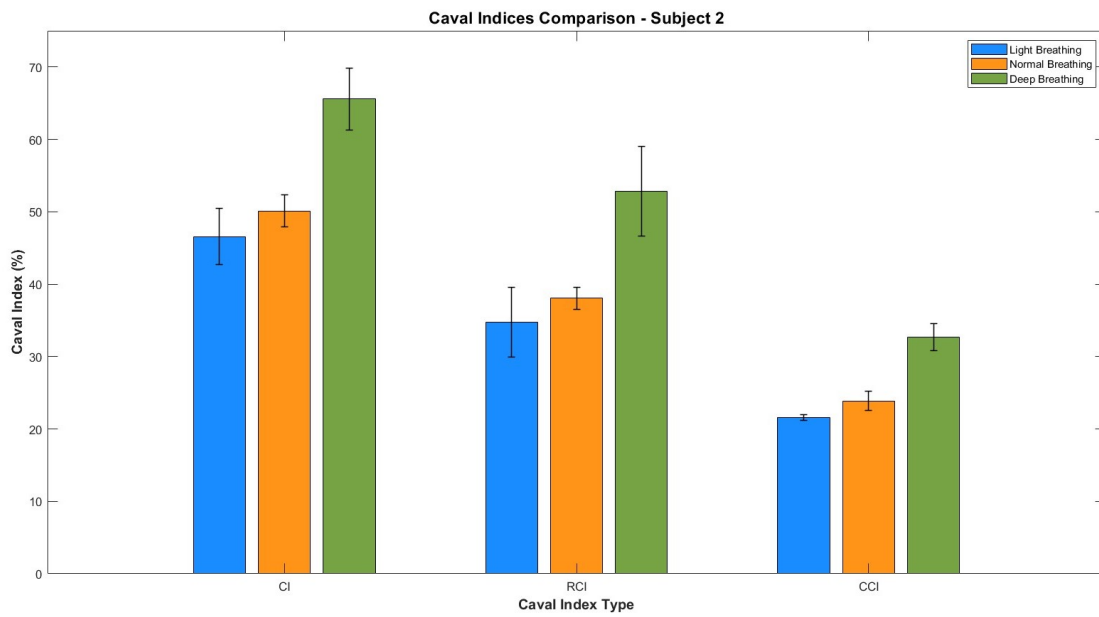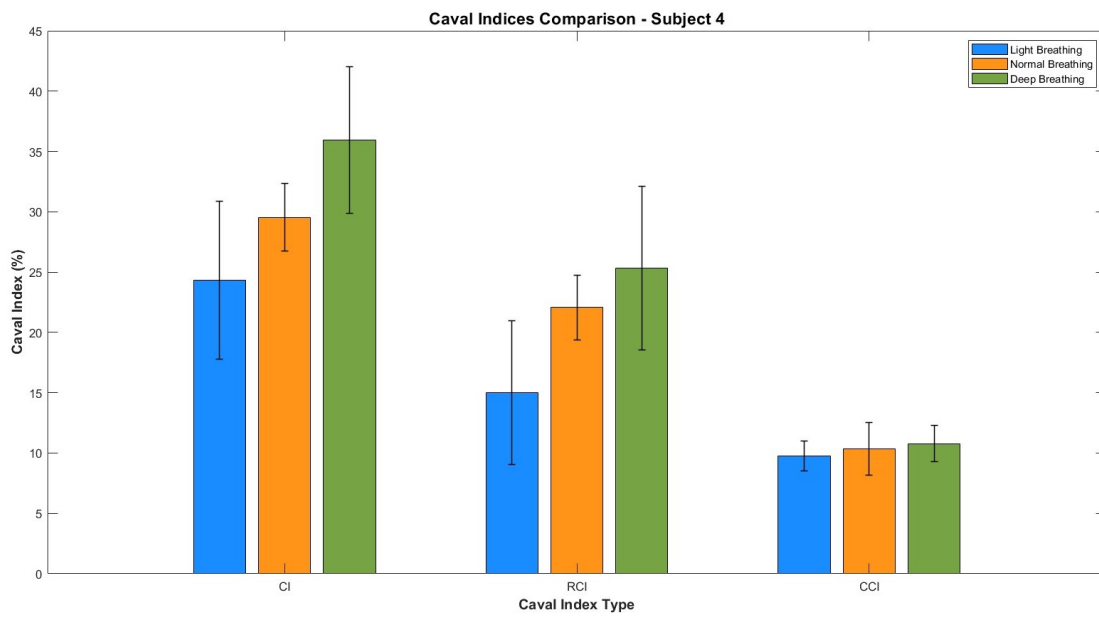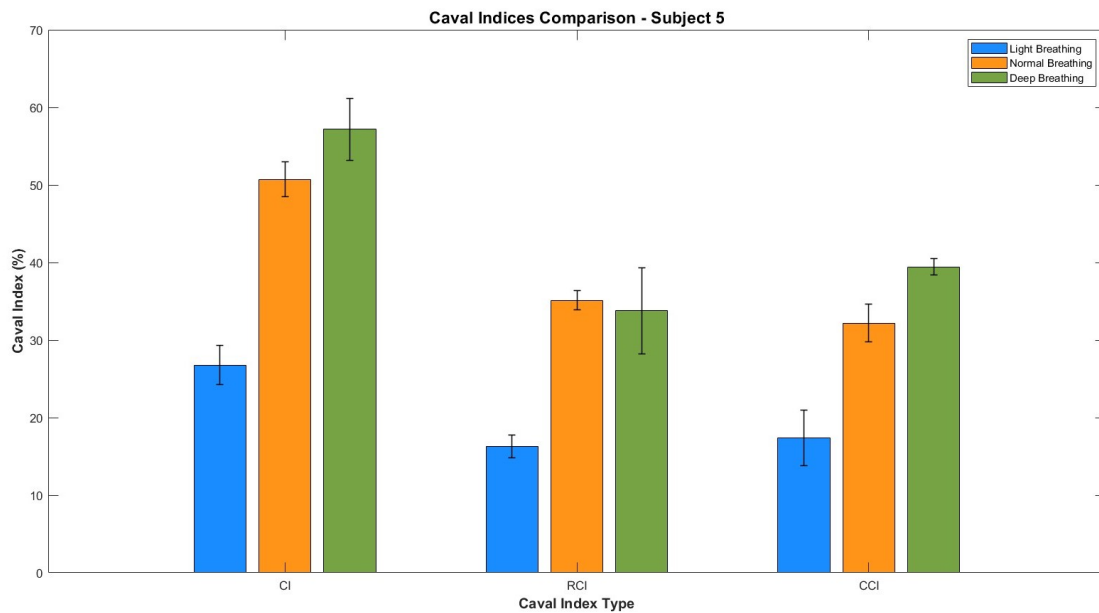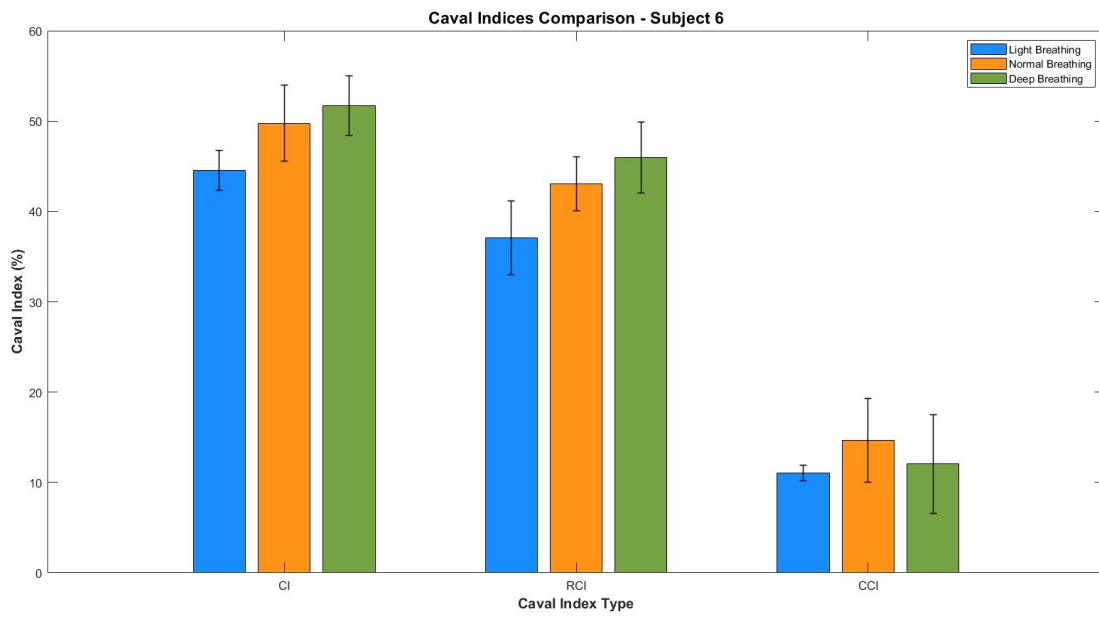
Figure A.2: *Bar chart showing mean values and standard deviations of the Caval Indices for each breathing mode, grouped according to the type of Caval Index, for subject 2.*
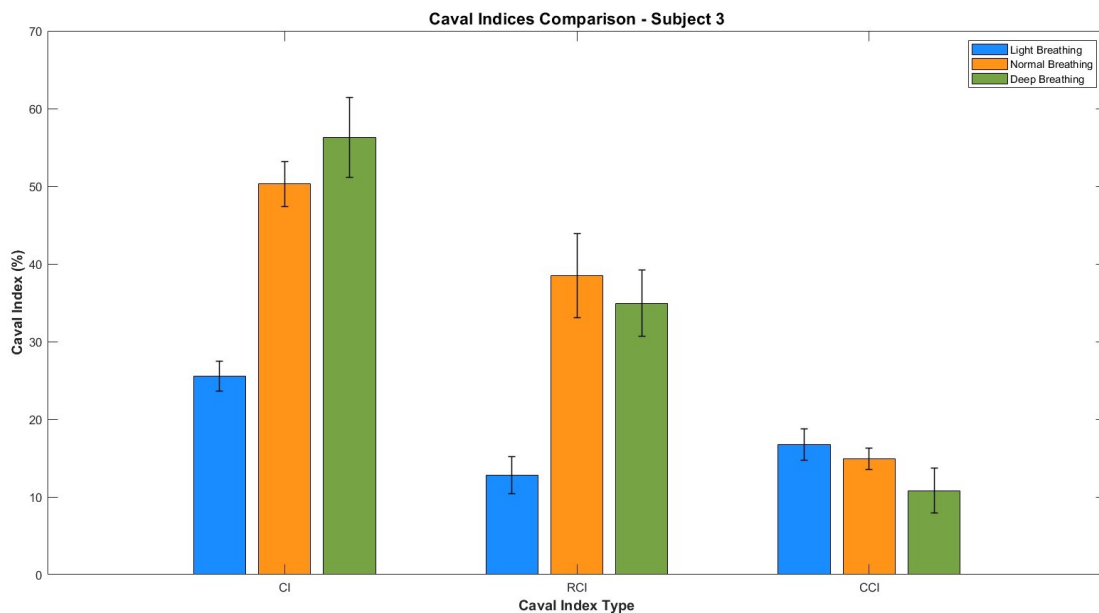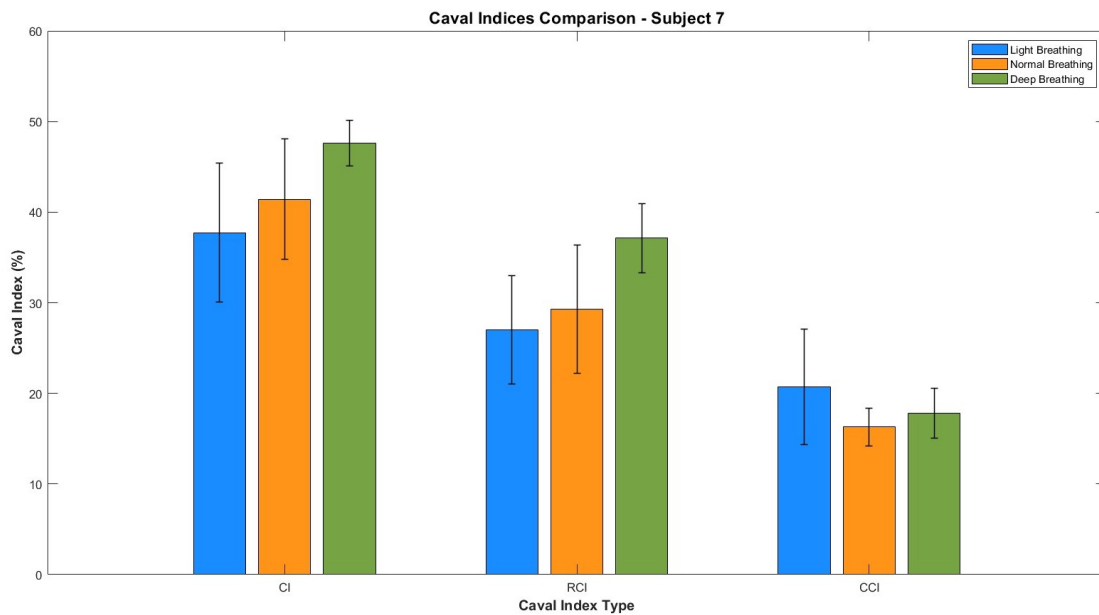

Figure A.3: *Bar chart showing mean values and standard deviations of the Caval Indices for each breathing mode, grouped according to the type of Caval Index, for subject 3.*

Figure A.4: *Bar chart showing mean values and standard deviations of the Caval Indices for each breathing mode, grouped according to the type of Caval Index, for subject 4.*

Figure A.5: *Bar chart showing mean values and standard deviations of the Caval Indices for each breathing mode, grouped according to the type of Caval Index, for subject 5.*
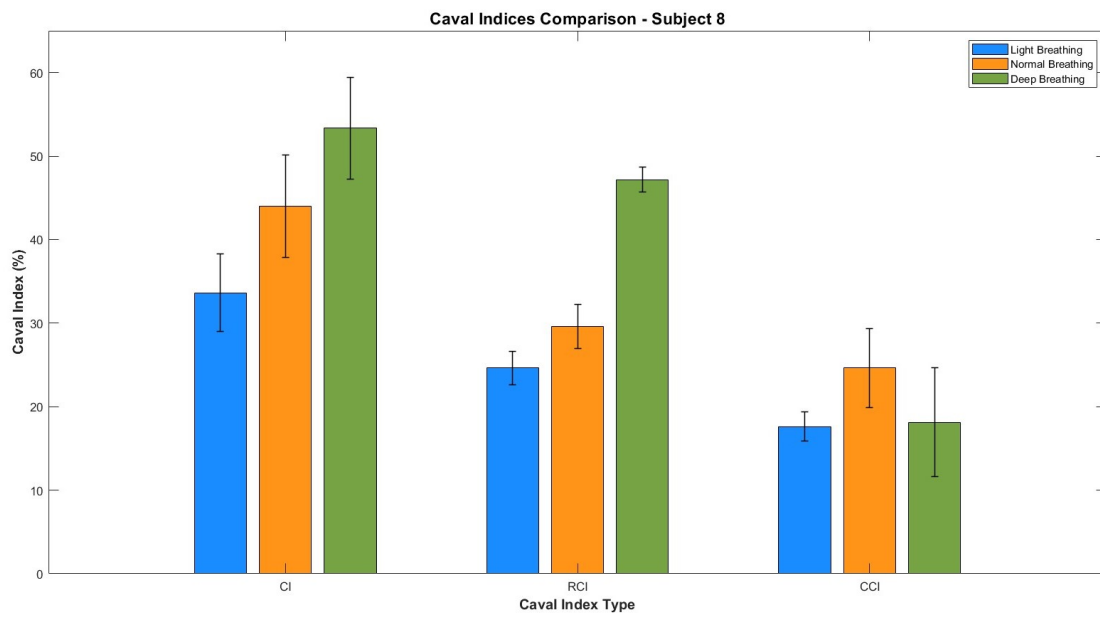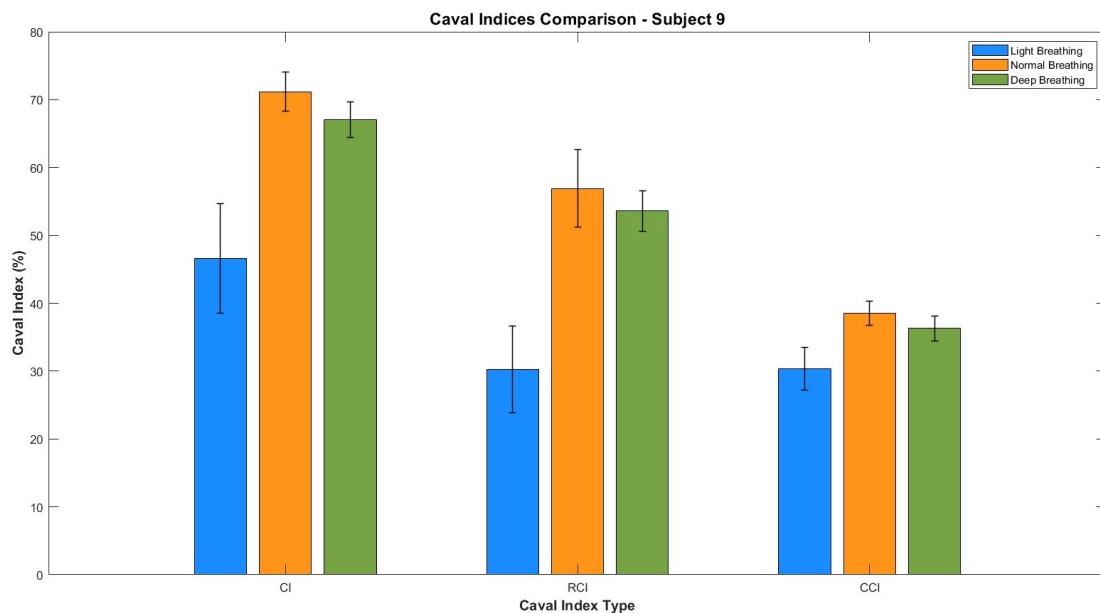
Figure A.6: *Bar chart showing mean values and standard deviations of the Caval Indices for each breathing mode, grouped according to the type of Caval Index, for subject 6.*

Figure A.7: *Bar chart showing mean values and standard deviations of the Caval Indices for each breathing mode, grouped according to the type of Caval Index, for subject 7.*
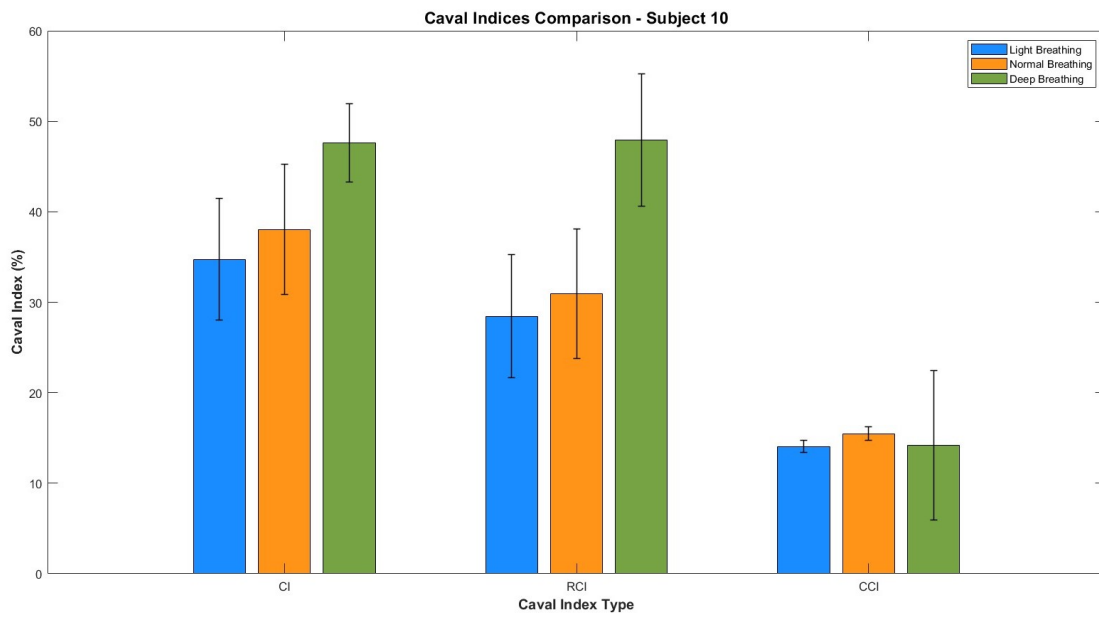
Figure A.8: *Bar chart showing mean values and standard deviations of the Caval Indices for each breathing mode, grouped according to the type of Caval Index, for subject 8.*

Figure A.9: *Bar chart showing mean values and standard deviations of the Caval Indices for each breathing mode, grouped according to the type of Caval Index, for subject 9.*

91

Figure A.10: *Bar chart showing mean values and standard deviations of the Caval Indices for each breathing mode, grouped according to the type of Caval Index, for subject 10.*

Appendix B

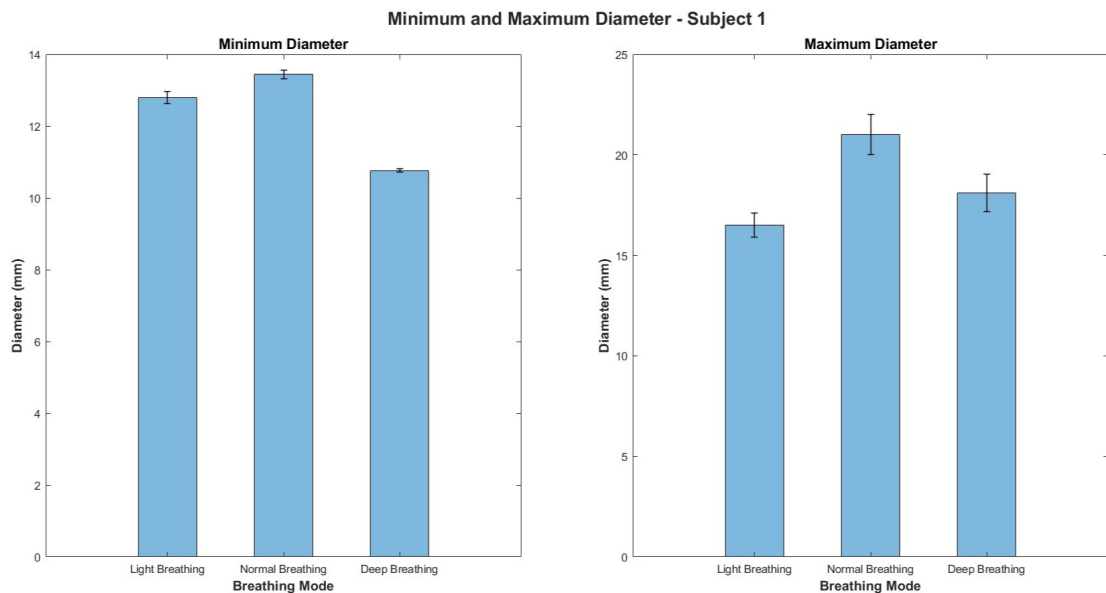# Minimum and maximum diameter graphs

Figure B.1: *Bar chart showing mean values and standard deviations of the minimum and maximum diameter of the IVC in the three breathing conditions for subject 1.*
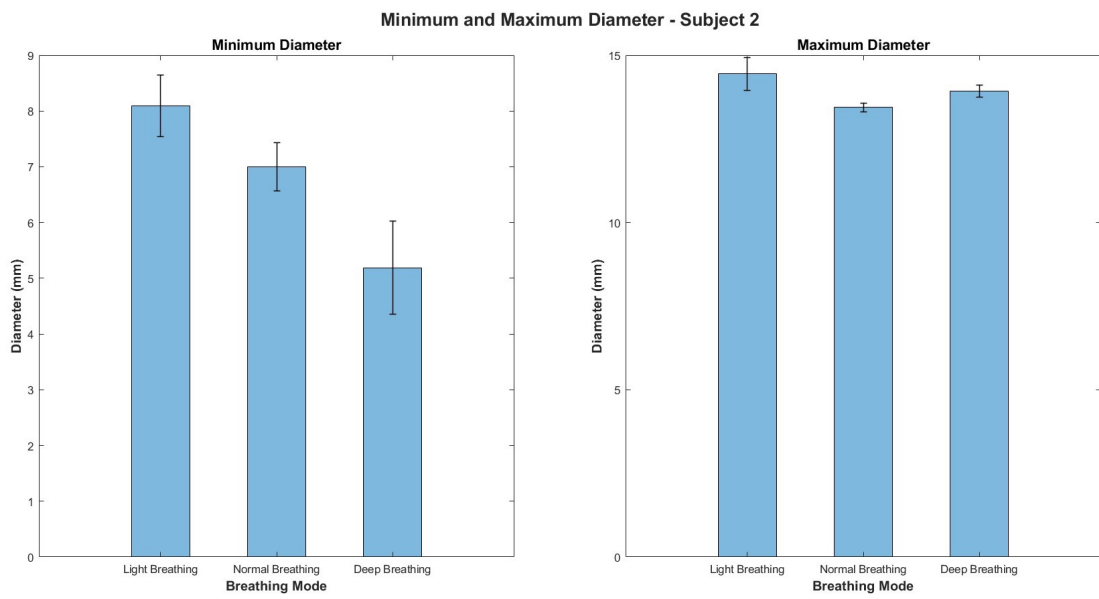
Figure B.2: *Bar chart showing mean values and standard deviations of the minimum and maximum diameter of the IVC in the three breathing conditions for subject 2.*
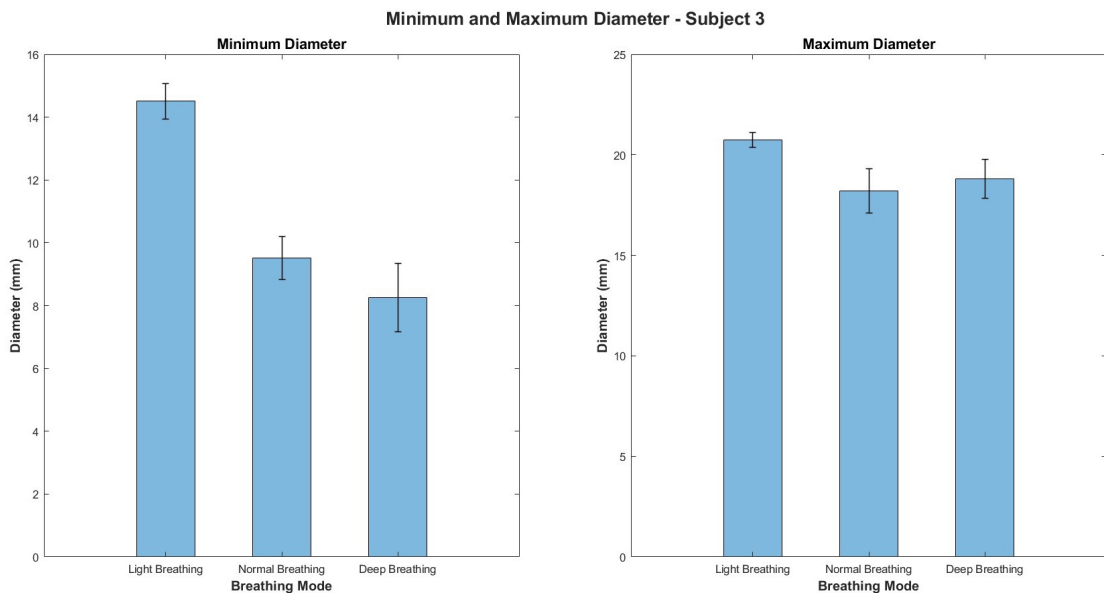

Figure B.3: *Bar chart showing mean values and standard deviations of the minimum and maximum diameter of the IVC in the three breathing conditions for subject 3.*
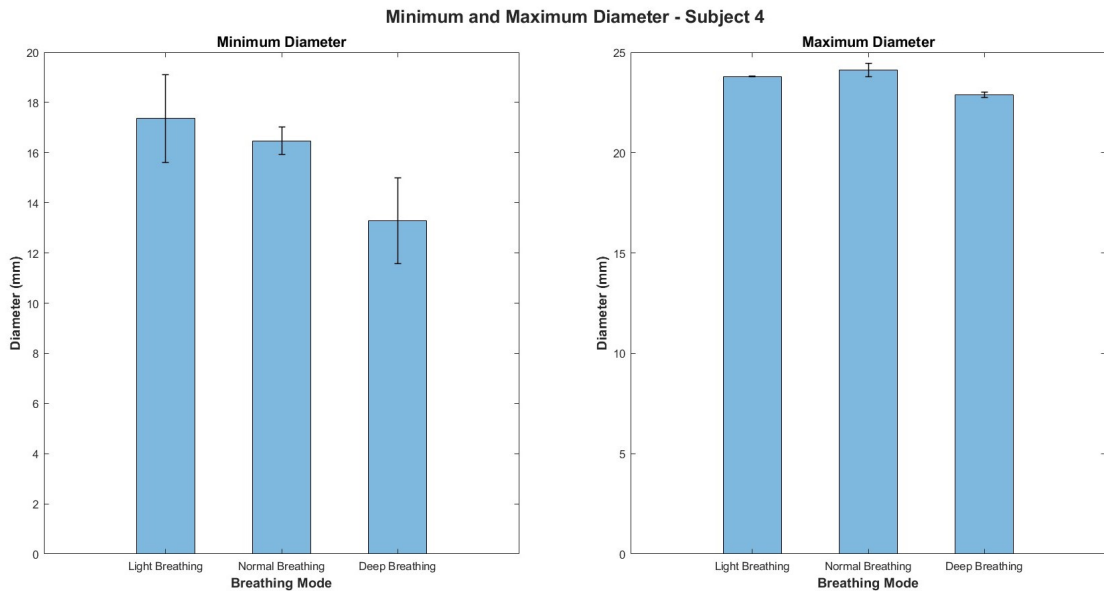
Figure B.4: *Bar chart showing mean values and standard deviations of the minimum and maximum diameter of the IVC in the three breathing conditions for subject 4.*

Figure B.5: *Bar chart showing mean values and standard deviations of the minimum and maximum diameter of the IVC in the three breathing conditions for subject 5.*
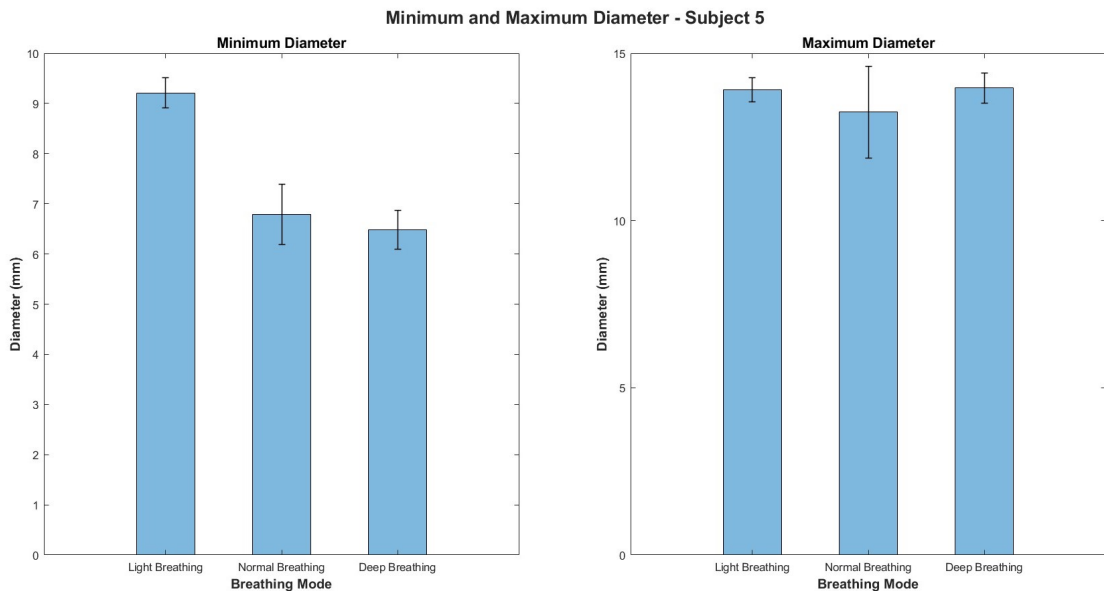
Figure B.6: *Bar chart showing mean values and standard deviations of the minimum and maximum diameter of the IVC in the three breathing conditions for subject 6.*

Figure B.7: *Bar chart showing mean values and standard deviations of the minimum and maximum diameter of the IVC in the three breathing conditions for subject 7.*
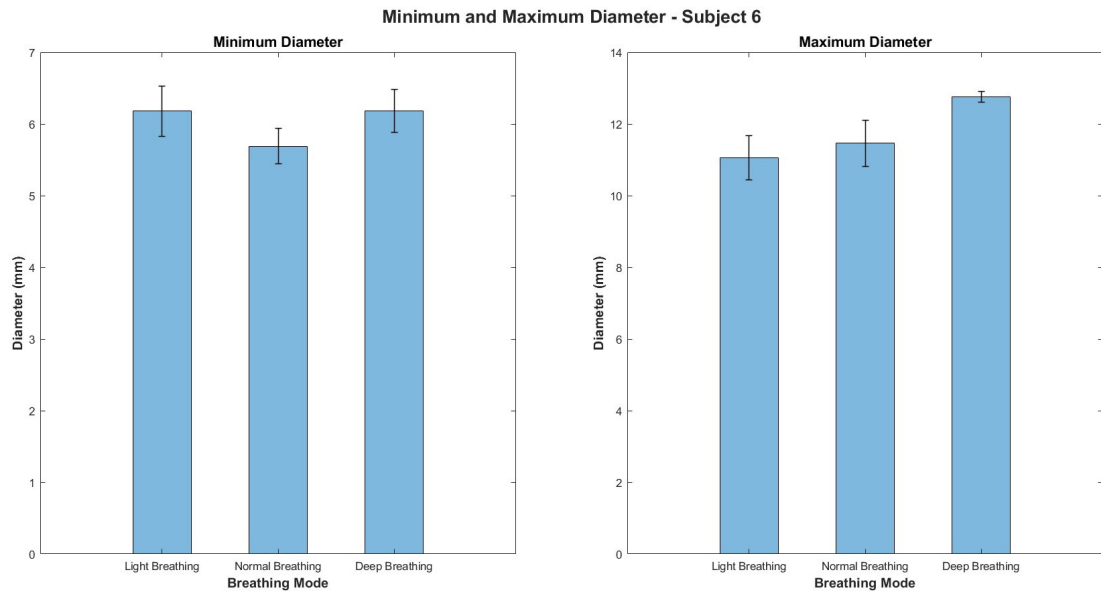
Figure B.8: *Bar chart showing mean values and standard deviations of the minimum and maximum diameter of the IVC in the three breathing conditions for subject 8.*

Figure B.9: *Bar chart showing mean values and standard deviations of the minimum and maximum diameter of the IVC in the three breathing conditions for subject 9.*
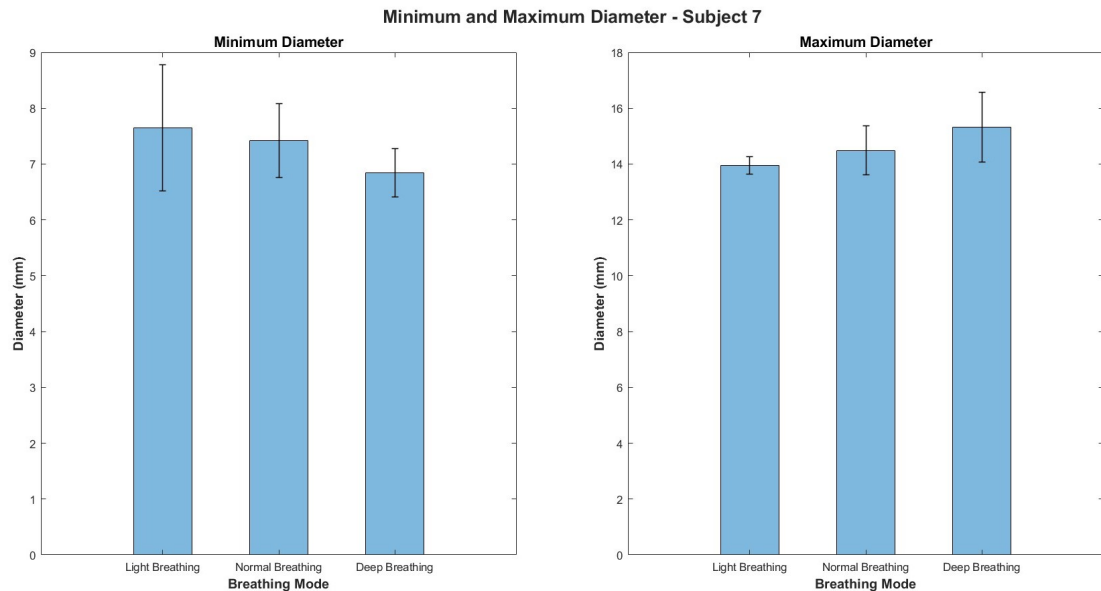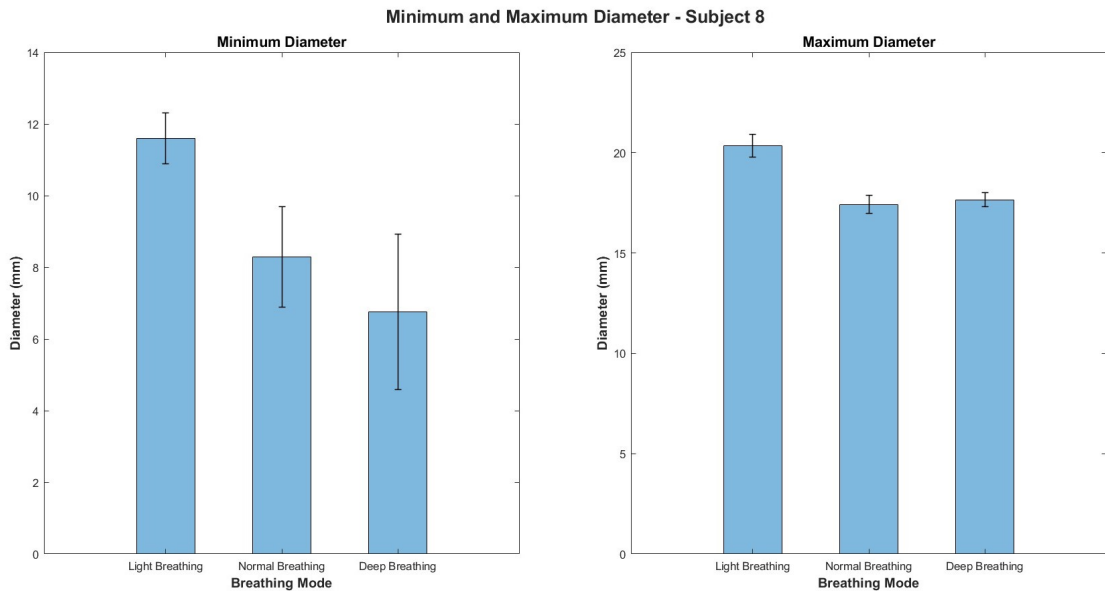
97

Figure B.10: *Bar chart showing mean values and standard deviations of the minimum and maximum diameter of the IVC in the three breathing conditions for subject 10.*
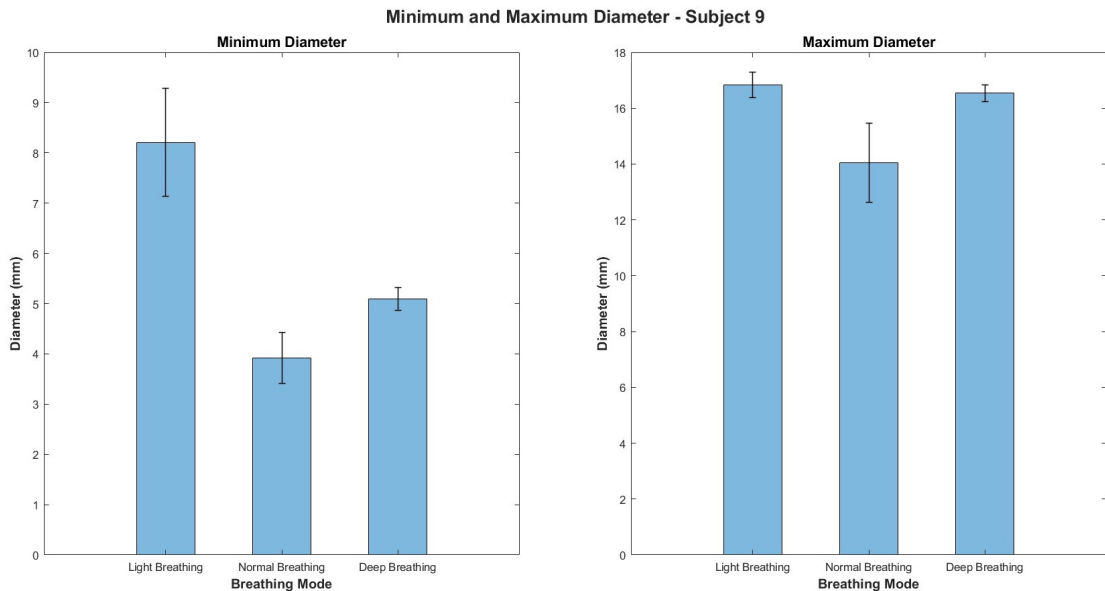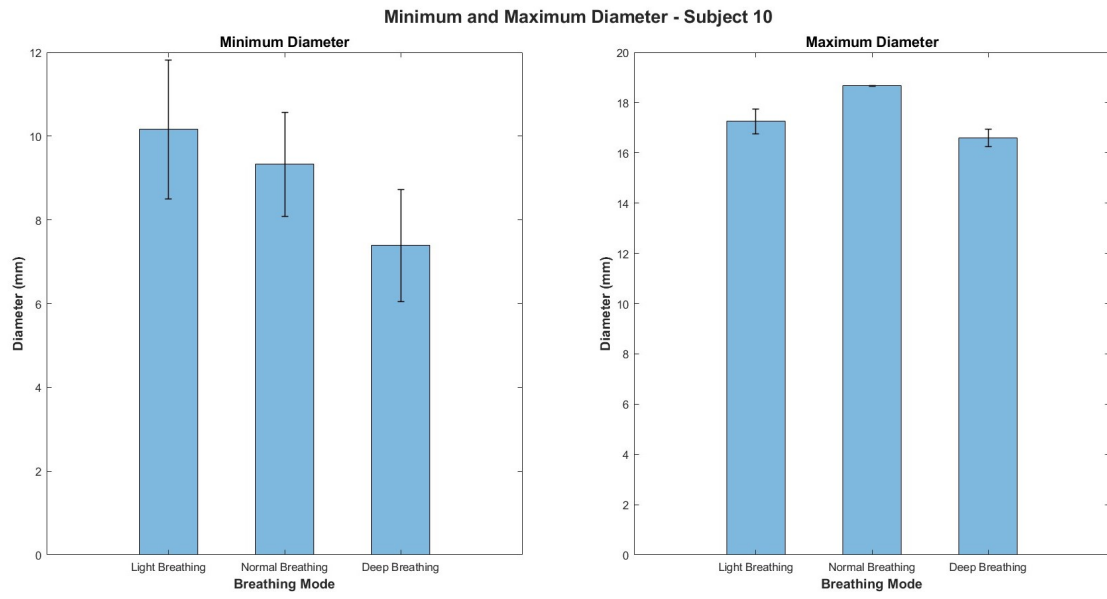
Bibliography

[1] Takayuki Kawata, Masao Daimon, Koki Nakanishi, Koichi Kimura, Naoko Sawada, Tomoko Nakao, Megumi Hirokawa, Jumpei Ishiwata, Norifumi Takeda, Yutaka Yatomi, and Issei Komuro. Factors influencing inferior vena cava diameter and its respiratory variation: simultaneous comparison with hemodynamic data. *Journal of Cardiology*, 79(5):642–647, 2022.

[2] `https://www.telemedultrasound.com/micrus-scanner/`.

[3] `https://www.viper.srl/`.

[4] `https://sensirion.com/products/catalog/SDP816-125Pa/`.

[5] `https://manuals.plus/national-instruments/usb-6001-6002-6003-low-cost-daq-usb-device-manual`.

[6] Luca Mesin, Stefano Albani, and Gianfranco Sinagra. Non-invasive estimation of right atrial pressure using inferior vena cava echography. *Ultrasound in medicine and biology*, 45(5):1331–1337, 2019.

[7] Leonardo Ermini, Stefano Seddone, Piero Policastro, Luca Mesin, Paolo Pasquero, and Silvestro Roatta. The cardiac caval index: improving noninvasive assessment of cardiac preload. *Journal of Ultrasound in Medicine*, 41(9): 2247–2258, 2022.

[8] Stefano Albani, Luca Mesin, Silvestro Roatta, Antonio De Luca, Alberto Giannoni, Davide Stolfo, Lorenza Biava, Caterina Bonino, Laura Contu, Elisa Pelloni, Emilio Attena, Vincenzo Russo, Francesco Antonini-Canterin, Nicola Riccardo Pugliese, Guglielmo Gallone, Gaetano Maria De Ferrari, Gianfranco Sinagra, and Paolo Scacciatella. Inferior vena cava edge tracking echocardiography: a promising tool with applications in multiple clinical settings. *Diagnostics*, 12(2):427, 2022.

[9] Cindy L. Stanfield. *Principles of human physiology*. Benjamin-Cummings Pub Co, 2010.

[10] Pierpaolo Di Nicolò, Guido Tavazzi, Luca Nannoni, and Francesco Corradi. Inferior vena cava ultrasonography for volume status evaluation: an intriguing promise never fulfilled. *Journal of Clinical Medicine*, 12(6):2217, 2023.

[11] Keith Lamb, Danny Theodore, and Beenish S. Bhutta. *Spirometry*. StatPearls Publishing LLC, 2023.

[12] Panita Worapratya, Sawanya Anupat, Ruedeekorn Suwannanon, and Prasit Wuthisuthimethawee. Correlation of caval index, inferior vena cava diameter, and central venous pressure in shock patients in the emergency room. *Open Access Emergency Medicine*, 6:57–62, 2014.

[13] Lawrence G Rudski, Wyman W Lai, Jonathan Afilalo, Lanqi Hua, Mark D Handschumacher, Krishnaswamy Chandrasekaran, Scott D Solomon, Eric K Louie, and Nelson B Schiller. Guidelines for the echocardiographic assessment of the right heart in adults: a report from the american society of echocardiography. *American Society of Echocardiography*, 23(7):685–713, 2010.

[14] Luca Mesin, Piero Policastro, Stefano Albani, Christina Petersen, Paolo Sciarrone, Claudia Taddei, and Alberto Giannoni. Non-invasive estimation of right atrial pressure using a semi-sutomated echocardiographic tool for inferior vena cava edge-tracking. *Journal of Clinical Medicine*, 11(12):3257, 2022.

[15] Laura L. Becerra, Tarek Rafeedi, Sankaran Ramanarayanan, Ian Frankel, Juliana Miller, Alexander Chen, Yi Qie, Darren Lipomi, Harinath Garudadri, and Tse-Nga Ng. Bidirectional venturi flowmeter based on capacitive sensors for spirometry. *Advanced Materials Technologies*, 8(18), 2023.

[16] Luca Mesin, Tatiana Giovinazzo, Simone D'alessandro, Silvestro Roatta, Alessandro Raviolo, Flavia Chiacchiarini, Massimo Porta, and Paolo Pasquero. Improved repeatability of the estimation of pulsatility of inferior vena cava. *Ultrasound in medicine and biology*, 45(10):2830–2843, 2019.

[17] Gregory W. Corder and Dale I. Foreman. *Nonparametric Statistics: A-Step-by-Step Approach*. Wiley, 2014.